Kyoto University

Ab-initio design methods for selective and efficient optomechanical control of nanophotonic structures

Doctoral thesis in Electronic Science and Engineering

Author:
Pedro A. Favuzzi
Supervisor:
Prof. Yoichi Kawakami

Contents

Chapter 1

Introduction

1.1 Thesis objective

The objective of this thesis is to develop methods and techniques to better understand and tailor optical forces between photonic waveguides by studying the relationship between the behavior of such forces and the morphology of the photonic system. In practice this implies an increased ability to control the position and vibrational modes of nano-mechanical systems via optical forces. This is not only an important step toward the development of simple MEMS devices based on such interaction but the increased flexibility of such effect should allow the realization of novel all optical photonic devices.

1.2 Background

All optical devices are a long standing dream of photonics [1, 2]. Ideally these should allow the realization of faster and more energy efficient technologies than electronic devices. The later require the transport of electric charge though transistors and diodes, which is done at sub relativistic speeds. This gives an inherent limitation to the working speed of electronic devices: the faster the electron moves the more energy it will carry and the harder it will be to control it so that, in order to increase the device speed, manufacturers are forced towards extreme miniaturization which in turn leads to lower energy efficiency and closer to quantistic effects. Instead, photons are the fastest thing in nature and have been used for information transmission for several decades in the form of omnipresent optic-fibers. Not surprisingly these devices are mainly limited by how fast we can transfer an optical signal to an electronic signal and vice versa. This has driven the production of smaller and

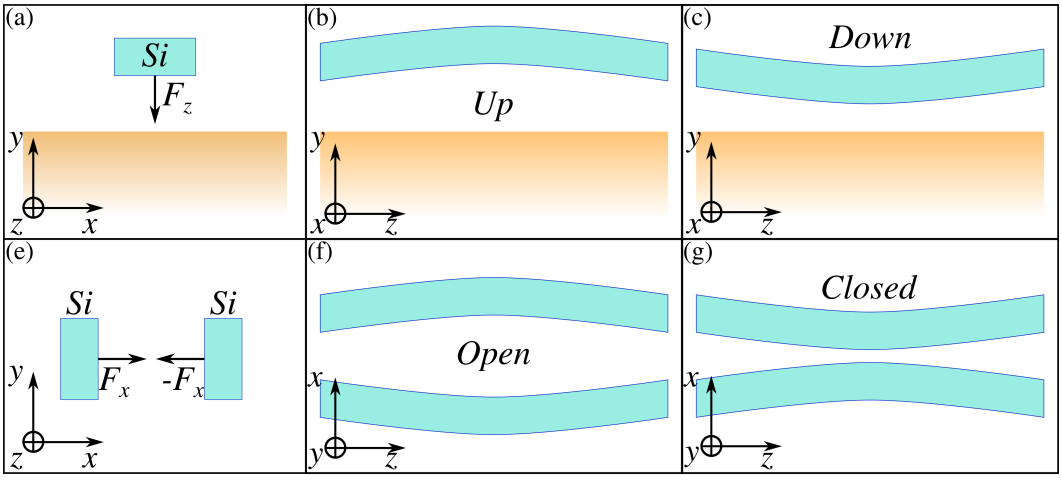

Figure 1.1: **(a)**:Cross sectional representation of the system used in [6], **(b-c)**: *Up* and *Down* state of the same device.

more integrated electro/opto transducers, which transform electronic signals into optical pulses, all the way up to on-chip integration of electronic and optic elements. Of course, it would be possible (at least in theory) to progressively supplant electronic components with optical ones. However this is not imaginable unless we are able to modify the path of light with light. Electric devices function via transistors and other similar components that control the flow of information, electrons packages, by applying voltages and currents in specific ways. Similarly, an all optical device should control the flow of light via smaller optical signals that control the state of the system in which light is traveling through, which can be done by taking advantage of non-linear effects [3]. Unfortunately this solution is less than optimal due to the significant loss induced by such methods which have to be compensated for, making the system more complex and less energy efficient [4]. Another important issue of optical circuits is the lack optical diodes [5] as well as optical memories.

1.2.1 Stable optical memories

While most optical memories require the presence of optically active layers like quantum wells [7]. A recent proposal demonstrated that passive, all-optical memories can be developed via the use of gradient optical forces [6]. This implementation, schematically shown in Figure 1.1 is based on the optical force that a Silicon waveguide experiences in proximity to a Silicon dioxide substrate. This force is usually called gradient optical-force (or simply gradient-force) and

it is directed normally to the wavevector of the optical signal. In this specific example an attractive force between the waveguide and the substrate appears due to gradient forces and, by making use of the mechanical Euler instability, once a sufficient amount of force is applied, the beam can be driven to a stable buckling point as shown in Figure 1.1(b) and (c). In this figure we assume that light travels along the waveguide‘s axis (parallel to the x-axis), and can be used to drive the beam into the stable *Up* or *Down* state. Due to the presence of the substrate these two have slightly different resonant transmission frequencies, which can be measured once such state is "impressed" into the system. Optomechanical memories are stable at room temperature and under reasonable using conditions. One of the limitations of such device is its complex usability. In [6], in order to "erase" the memory state, they make use of a complex optomechanical cooling technique; mainly because of the lack of repulsive interaction between waveguide and substrate. In [8] they considered the case where the optical force was induced by the interaction between two parallel waveguides, as shown in the second row of Figure 1.1. In this case the *Up* and *Down* states are exchanged for *Open* and *Closed* states. They observed that, even in the presence of repulsive interaction, in vacuum, which offers the best working conditions for moving micro-mechanical devices, an optomechanical trapping effect would be required for optimal operation. These are indeed limitations that modern optomechanic devices must deal with if we ever wish to integrate such system in MEMS or electronic devices.

1.2.2 Optomechanical devices

Optomechanical memories are an example of integration with MEMS devices, which are formed by a moving mechanical part plus and actuation system. In optomechanics we "simply" change the capacitive, piezoelectric or magnetic actuators, just to name a few, with an optical one [10]. A significant advantage of such interaction for all optical devices is the lack of loss [11]. This type of devices can be operated statically or dynamically. In the static regime the device operation is quite simple: the system is modified by constant optical forces or by an externally applied force, which deforms the initial geometry of the system changing its resonant frequency. The frequency shift from the unperturbed state gives a measurement of the total deformation and the applied force. Many optomechanic systems based on this principle perform better than their classical counterparts as pressure sensors [12], switches [9] or interferometers [13].

Excellent performance is given by the optomechanical switch proposed by [9] and described in Figure 6.1. In this case the device is formed by a

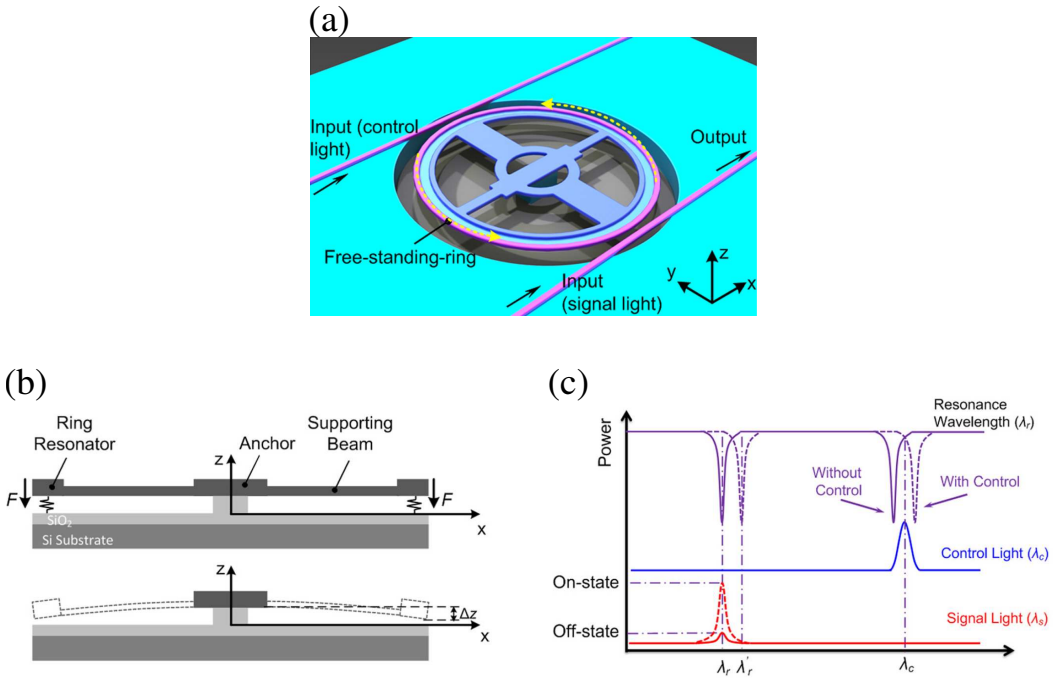

Figure 1.2: **(a)**: Schematic of an optomechanical switching device described in [9], **(b)**: Representation of the mechanical force acting on the ring resonator shown in (a), **(c)**: optical characterization of the switch. Figures were taken from [9]

.

ring resonator, which interacts optomechanically with the substrate, as shown in Figure 6.1(b). One waveguide is used to load the optical control pulse in the ring-resonator that induces the optical force and the other waveguide contains the signal to be modulated. As a result, once a force is applied, the suspended ring resonator will be deformed, changing its resonance frequency, shown in Figure 6.1(c), so that the probe signal goes on and off resonance with the resonator and the transmissivity of the system at the control signal wavelength can be changed. This system shows no residual vibration or switching overshoot and it is also an order of magnitude faster than thermally tuned switches [14].

Dynamically operated optomechanical-devices, instead, can be used for wavelength conversion [15, 16], with ideally no absorption loss, unlike alternative methods like other ultra-fast modulation techniques based on optical hot carrier injection [17]. Of course, this can only be done in the presence of high Q-factor cavities where the lifetime of the photon is on the order of magnitude

of the mechanical oscillation period so that the photon can "sense" the mechanical vibration which allows the mechanical energy to be transferred from the mechanical to the optical resonance and vice versa [18]. This devices are some between the most sensitive motion sensors with more than sub-atomic displacement sensitivity [19].

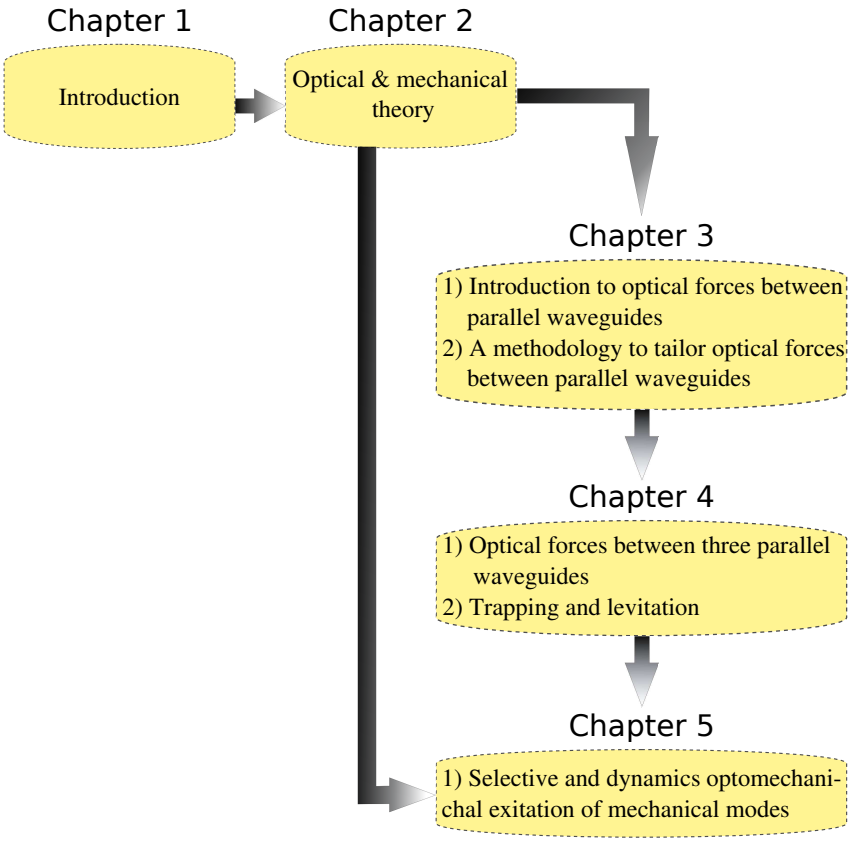

Figure 1.3: Schematic outline of the content of each chapter of this thesis

.

1.3 Thesis outline

In this thesis we develop simple and intuitive methods that can be used to describe and predict both magnitude and direction of optical forces between parallel waveguides. We will use this method to increase our ability to control the forces acting between (but not limited to) parallel dielectric waveguides.

As we will show in **Chapter 2**, optical forces can be described as a surface integral along the interface between two different media, its magnitude is approximately equal to the square of the electric field along the such surface and directed normally to it. Such simple formulation of optical forces allows us, in **Chapter 3**, to elaborate a semi-empirical method to tailor such forces between two parallel waveguides and to demonstrate the effect of periodicity on the forces, which is a direct consequence of the field distribution. In **Chapter 4** we extend our study to a more complex, less symmetric system, formed by three parallel waveguides, where the central one is free to move and the external ones are fixed. While the dynamics of fields and forces are described via the methodology developed in **Chapter 3**, such system demonstrates an increased ability to manipulate the free beam in the whole space normal to the direction of propagation of light. In **Chapter 5** we demonstrate, using the same configuration studied in **Chapter 4**, that optical forces can also be tailor along the direction of propagation of light, albeit the forces remain normal to it.

In **Chapter 2** we introduce the methods and theory that will be used though out this thesis. We begin by briefly describing the computational methods used (a plane-wave basis eigensolver and FDTD solver), we then discuss and derive two different, but equivalent, formulations of optical force: The Maxwell stress tensor and a surface integral formulation based on perturbation theory. Two different ways to modulate the refractive index of Silicon in a controllable and not permanent manner are introduced. Also we give a short introduction to the eigenmode-dynamics of a single doubly-clamped nano-beam in the Euler-Bernoulli approximation.

Chapter 3 is mainly focused on the formulation of a set of principles and a methodology useful to tailor and enhance optical forces between parallel, dielectric waveguides by molding the eigenmode field distribution via the combined effects of highly symmetric slow light modes and waveguide morphology. The proposed technique can be used to predict the field distribution of complex, but axis-symmetric structures so that the direction and amplitude of the force might be inferred from them. We also demonstrate that band edge modes can not only be used to enhance the magnitude of the force but that, since they induce unique symmetry-constrains on the field distribution, with an appropriate choice of geometry, they can also be used to tailor optical forces. This way we are able to control the direction of the optical force at very short separations with geometries that are amenable to standard lithographic techniques.

The principles formulated in **Chapter 3** are used in **Chapter 4** to investigate the optical forces induced by localized optical modes propagating along

three parallel waveguides, of which only the central one is free to move. In this configuration, when all three waveguides are identical, the components of the optical-force acting on the free beam are decoupled along the axis of symmetry. As a result, two dimensional optomechanical control of the central waveguide, like single-mode optical trapping, can be achieved. We also study non symmetric configurations that can be used, for example, to tailor the position of the optical trap.

The three parallel waveguides configuration presented in the previous chapter is now used in **Chapter 5** in order to selective and efficiently excite high frequency vibrational eigenmodes of micro-mechanical double clamped beams. This technique is based on an optomechanical system formed by three parallel waveguides, where the central one is free to move and the refractive index of the external ones in modulated via optical, free-carrier injection. This configuration allows us to obtain forces of opposite sign along the free beam and thus, with an appropriate refractive index modulation, optical forces can be tailored to match the amplitude profile of, possibly, any selected mechanical mode. The technique here presented offers an alternative to resonant excitation, which might be difficult to achieve for higher frequencies, and, we believe, might be of significant importance in the realization of future all optical devices. We also study a static modulation of the refractive index, by simply modulating the thickness of the plates, which offers stronger forces since a much larger perturbation is possible.

In **Chapter 6** we quickly summarize our results an reach a conclusion on the goals of this thesis as well as discussing the future developments of our work

Bibliography

[1] S. A. Maier, M. L. Brongersma, P. G. Kik, S. Meltzer, A. A. G. Requicha, and H. A. Atwater. Plasmonicsa route to nanoscale optical devices. *Advanced Materials*, 13(19):1501–1505, 2001.

[2] C. Monat, P. Domachuk, and B. J. Eggleton. Integrated optofluidics: A new river of light. *Nature photonics*, 1(2):106–114, 2007.

[3] R. W Boyd. *Nonlinear optics*. Academic press, 2003.

[4] A. V. Zayats and S. Maier. Active plasmonics and tuneable plasmonic metamaterials, 2013.

[5] M. S. Kang, A. Butsch, and P. S. J. Russell. Reconfigurable light-driven opto-acoustic isolators in photonic crystal fibre. *Nature Photonics*, 5(9):549–553, 2011.

[6] M. Bagheri, M. Poot, M. Li, W. Pernice, and H. Tang. Dynamic manipulation of mechanical resonators in the high amplitude regime through optical backaction. *Nature Nanotechnology*, 6:726–732, 2011.

[7] M. T. Hill, H. J. S. Dorren, T. De Vries, X. J. M. Leijtens, J. H. Den Besten, B. Smalbrugge, Y. S. Oei, H. Binsma, G. D. Khoe, and M. Smit. A fast low-power optical memory based on coupled micro-ring lasers. *Nature*, 432(7014):206–209, 2004.

[8] V. Intaraprasonk and S. Fan. Nonvolatile bistable all-optical switch from mechanical buckling. *Applied Physics Letters*, 98(24):241104, 2011.

[9] H. Cai, B. Dong, J. F. Tao, L. Ding, J. M. Tsai, G. Q. Lo, A. Q. Liu, and D. L. Kwong. A nanoelectromechanical systems optical switch driven by optical gradient force. *Applied Physics Letters*, 102(2):023103–023103, 2013.

[10] M. Gad-el Hak. *MEMS: introduction and fundamentals*. CRC press, 2010.

[11] D. Van Thourhout and J. Roels. Optomechanical device actuation through the optical gradient force. *Nature Photonics*, 4(4):211–217, April 2010.

[12] X. Zhao, J. M. Tsai, H. Cai, X. M. Ji, J. Zhou, M. H. Bao, Y. P. Huang, D. L. Kwong, and A. Q. Liu. A nano-opto-mechanical pressure sensor via ring resonator. *Optics express*, 20(8):8535–42, April 2012.

[13] J. Ma and M.L. Povinelli. Applications of optomechanical effects for on-chip manipulation of light signals. *Curr. Op. in. Sol. St. and Mat. Sci*, 16:82–90, 2012.

[14] W. M. Zhu, T. Zhong, A. Q. Liu, X. M. Zhang, and M. Yu. Micromachined optical well structure for thermo-optic switching. *Applied Physics Letters*, 91(26):261106–261106, 2007.

[15] Y. Liu, M. Davanço, V. Aksyuk, and K. Srinivasan. Electromagnetically induced transparency and wideband wavelength conversion in silicon nitride microdisk optomechanical resonators. *Phys. Rev. Lett.*, 110:223603, May 2013.

[16] Y. Tanaka, J. Upham, T. Nagashima, T. Sugiya, T. Asano, and S. Noda. Dynamic control of the q factor in a photonic crystal nanocavity. *Nature materials*, 6(11):862–865, 2007.

[17] J. Upham, Y. Tanaka, T. Asano, and S. Noda. On-the-fly wavelength conversion of photons by dynamic control of photonic waveguides. *Applied physics express*, 3(6):2001, 2010.

[18] M. Aspelmeyer, S. Groblacher, K. Hammerer, and N. Kiesel. Quantum optomechanics–throwing a glance. *JOSA-B*, 27:189–197, 2010.

[19] E. Gavartin, P. Verlot, and T. F. Kippenberg. A hybrid on-chip optomechanical transducer for ultrasensitive force measurements. *Nature Nanotechnology*, 7(8):509–514, 2012.

Chapter 2

Optical forces in photonic system

2.1 Introduction

The mechanical interaction between light and matter has been a topic of theoretical interests for the last century but, until recently, the discussion has mainly been focused on the Abraham-Minkowski dilemma [1–4] and, in general, over the correct formulation of the electromagnetic stress tensor in both classical and relativistic systems [5]. The first applications of optical forces date back to more than a decade [6–8], however, this first attempts, lack of the fine fabrication capabilities [9], simulation tools [10, 11] and precise spatial control of electromagnetic radiation [12] that it is now available. While fabrication and simulation tools were slowly improved year after year, our ability of controlling light has been boosted by the development of photonic crystals [13]. This structures, which are formed by adding periodic perturbations to otherwise smooth systems, are well suited to an Eigenvalue description, at least as long as non lossy materials are considered [14]. The Eigenvalue formulation of electromagnetism [15] is at the base of the recent developments in optomechanics where forces are induced by localized-evanescent fields [16] rather than free propagating photons. Moreover, the improved resolution of nanofabrication techniques allows the fabrication of small, suspended, mechanical structures [17] that can be deformed with relative ease, which is important since the magnitude of optical forces is quite small compared to mechanical ones [18]. Finally, due to the ever growing and cheaper availability of computational power, it has become easier to run high resolution full-electromagnetic and mechanical simulations; especially important in electromagnetic related

problems which depend on the exact distribution of the electromagnetic fields as we will demonstrate along this thesis.

In this chapter we review the basic theoretical concepts and numerical methods that will be used though out the thesis. In section 2.2.1 the basic eigenmode formulation of Maxwell equations will be introduced with an accent on the relationship between eigenfrequency, group velocity and field distribution. We make use of mainly two numerical tools: MPB and MEEP [10, 11]. The first one is a Block iterative eigensolver in a planewave basis, while the second is and FDTD solver. Eigenmode solvers are especially useful when well defined periodic systems are under study, while FDTD is a versatile technique well suited for more complex studies where the finite dimensionality of the photonic systems or added non-periodic elements need to be taken into account. Both methods will be introduced in section 2.3. The link between optical forces and field distribution will be discussed in section 2.4, where the coupling to specific mechanical deformations will be investigated. Methods useful to modulate the refractive index of dielectric materials will be presented in section 2.6. Instead, in section 2.7 we will describe some mechanical and mathematical properties of mechanical modes and in section 2.8 we look at more detailed properties of mechanical excitation and nonlinear properties or solids. In this chapter, as in the following ones, we use Lorentz-Heaviside units, for which the speed of light, the vacuum permittivity and permeability are all equal to 1 [5] and, where possible, we prefer using non-dimensional quantities.

2.2 Nanophotonic waveguides

An example of photonic crystal are dielectric waveguides which are, in fact, one dimensional photonic systems [15]. Even smooth waveguides can be thought as periodic waveguides with zero length unit-cells and, as such, can still be described as a periodic Bloch system. This is important since designing single mode waveguides is relatively simple and, as a result, a modal simulation is enough to investigate the light flow through the waveguide itself. In the next few section we will discuss such eigenmode expansion of light in photonic systems by closely following the discussion found in [15].

2.2.1 Eigenmode solution of Maxwell equations

In here we assume that the systems under study are composed by linear, non-lossy materials and that the electromagnetic fields are harmonic in time. This

allows us to split the electric (or magnetic) field distribution into spatial and time varying parts as:

$$\begin{aligned}\mathbf{E}(r,t) &= \mathbf{E}(r)e^{i\omega t} \\ \mathbf{H}(r,t) &= \mathbf{H}(r)e^{i\omega t}.\end{aligned} \tag{2.1}$$

This, once inserted into Maxwell equations, leads to decoupling the electric and magnetic fields into two independent equations. For example, for $\mathbf{E}$ we can write:

$$\frac{1}{\sqrt{\varepsilon(r)}}\nabla\times\nabla\times\mathbf{E}(r) = \left(\frac{\omega}{c}\right)^2\sqrt{\varepsilon(r)}\mathbf{E}(r). \tag{2.2}$$

This equations is at the basis of the eigenvalue problem, where an *operator* $\mathbf{\Theta} = \frac{1}{\sqrt{\varepsilon(r)}}\nabla\times\nabla\times\frac{1}{\sqrt{\varepsilon(r)}}$ acts on an *eigenfunction*, $\sqrt{\varepsilon(r)}\mathbf{E}$, and the results is the eigenfunction itself multiplied by a *eigenvalue* $(\omega/c)^2$. It can be also demonstrated that $\mathbf{\Theta}$ possesses some important properties as linearity and hermiticity and, as a consequence of the later, all its eigenvalues are real and eigenfunctions associated to non-identical eigenvalues are orthogonal. The hermiticity of Equation 2.2 can be demonstrated by showing that $(\mathbf{A},\mathbf{\Theta B}) = (\mathbf{A\Theta},\mathbf{B})$. To do so the inner product between two vector fields is define as

$$(\mathbf{A},\mathbf{B}) = \int \mathbf{A}^*(r)\cdot\mathbf{B}(r)dr. \tag{2.3}$$

We can now show that $\mathbf{\Theta}$ is Hermitian in few simple steps:

$$\begin{aligned}(\mathbf{A},\mathbf{\Theta B}) &= \int \mathbf{A}^*\frac{1}{\sqrt{\varepsilon}}\cdot\nabla\times\nabla\times\frac{\mathbf{B}}{\sqrt{\varepsilon}}\,dr \\ &= -\int\nabla\times\left(\frac{1}{\sqrt{\varepsilon}}\mathbf{A}\right)^*\cdot\nabla\times\frac{\mathbf{B}}{\sqrt{\varepsilon}}\,dr \\ &= \int\frac{1}{\sqrt{\varepsilon}}\left(\nabla\times\nabla\times\frac{\mathbf{A}}{\sqrt{\varepsilon}}\right)^*\cdot\mathbf{B}\,dr = (\Theta\mathbf{A},\mathbf{B}).\end{aligned} \tag{2.4}$$

It is important to notice that in Equation 2.4 the surface integrals were disregarded since we are only interested in localized modes whose fields decay to zero at large enough separations from the photonic system. Now that the hermiticity has been demonstrated we can try to gain more information about the distribution of the fields. To do so it is convenient to use the *Variational theorem* that states that the lowest eigenvalue corresponds to the eigenfunction (that is to say field distribution) that minimizes the following functional:

$$\left(\frac{\omega}{c}\right)^2 = \min_{\mathbf{E}}\frac{(\sqrt{\varepsilon}\mathbf{E},\Theta\sqrt{\varepsilon}\mathbf{E})}{(\sqrt{\varepsilon}\mathbf{E},\sqrt{\varepsilon}\mathbf{E})} = \min_{\mathbf{E}}\frac{\int|\nabla\times\mathbf{E}|^2\,dr}{\int\varepsilon\,|\mathbf{E}|^2\,dr}. \tag{2.5}$$

Much information can be extracted out of this simple function and will be at the foundation of Chapter 3. However, here, we limit ourselves to discuss the difference between the eigenvalue $(\omega/c)^2$ and the total energy of the electromagnetic field and the amplitude of the fields. As can be seen from Equation 2.5 ω is independent on the amplitude of the fields, while, classically, the energy of the fields depends quadratically on their amplitude. Thus, as expected from a parallelism to quantum mechanics, the energy stored should be expressed as the number of electromagnetic quanta ($U_{EM} = N\hbar\omega$) stored inside the system rather than as the field amplitude, which now becomes and arbitrary parameter of the system. As a result we can use a convenient normalization of the electric and magnetic fields where

$$\left(\sqrt{\varepsilon}\mathbf{E}, \sqrt{\varepsilon}\mathbf{E}\right) = 1, \quad (\mathbf{H}, \mathbf{H}) = 1. \tag{2.6}$$

This is relevant when we want to find the electromagnetic force in a photonic system since, $F = -dU/d\zeta$, where ζ is a parameter that describes the virtual mechanical deformation. Before describing the nature of the electromagnetic forces we will, first of all, explain the effect of periodicity on the fields and their description.

2.2.2 Dielectric waveguides and slow-light modes

The description of electromagnetic fields can be significantly "simplified" by the presence of symmetries and periodicity. In order to do so, in a similar fashion to what is commonly done in crystallography, it is necessary to first define an irreducible unit cell of the photonic-crystal structure: that is to say the smallest element that can be used to remap the entire crystal base on a defined set of symmetries. This is not only a geometrical process but has direct consequences on the form of the eigenfunction $\mathbf{E}$ which can be re written as:

$$\mathbf{E}(r) = \mathbf{E}_{\mathbf{k}}(r`)\mathbf{P}(k, r). \tag{2.7}$$

Where $\mathbf{E}_{\mathbf{k}}(r`)$ is the vector field defined over the unit cell space $r`$, $P(k, r)$ is a function that propagates $\mathbf{E}_{\mathbf{k}}(r`)$ over the entire space r and it is usually formed by a phase and a rotation, and k is a wave-vector. In this thesis, since we are only considering one dimensional structures we will only be concerned with translational symmetry and mirror symmetries, which, in principle, is a subcase of translational symmetry, where the phase of the translation is ± 1. We start by looking at this case and the information that adds to the eigenvalue problem. For example, imagine that we are studying a smooth waveguide. The waveguide is translationally identical along its axis, parallel to the x-axis

in Cartesian coordinates, while the cross-section of the waveguides is assume to be mirror symmetric respect to the y or z axis. As a result we expect, from simple intuition, that the electromagnetic field should also be y or z axis symmetric. For the z coordinate we express this in a short form as:

$$\begin{aligned} \mathbf{E}(z) &= \mathcal{M} \cdot \mathbf{E_0}(Abs(z)) \\ \mathbf{H}(z) &= (\mathcal{M}\ sig(z)) \cdot \mathbf{H_0}(Abs(z)). \end{aligned} \tag{2.8}$$

Where the *sig* function extracts the sign of the z coordinate, $\mathbf{E_0}$ and $\mathbf{H_0}$ is a function of the fields that do not depends on the sign of z and $\mathcal{M}$ is the following unitary matrix:

$$\mathcal{M} = \begin{pmatrix} 1 & 0 & 0 \\ 0 & 1 & 0 \\ 0 & 0 & sig(z) \end{pmatrix}. \tag{2.9}$$

It is now obvious, from the concepts developed in section 2.2.1, that $\mathcal{M}$ can also be interpreted as the eigenvalue of an eigenfunction "$\mathbf{S}$", that changes the sign of z and measures the eigenfunction $\mathbf{E}$ as $\mathbf{SE}(-z) = \mathcal{M}(-z)\mathbf{E}(z)$. Now, assume that the waveguide we have been looking at it is periodically modulated with a period Δx. Obviously, if we were to shift the waveguide of a length equal to its period (or a multiple of it) the geometry will not be changed and so should the fields, except for, possibly, a phase. This is the basic concept behind *Bloch theorem*, which states that any periodic system can be written as the product of a periodic function and a plane-wave, envelope function. In our case, where only translations along the x-axis are considered, the block theorem translates to:

$$\mathbf{E}(k, r) = \mathbf{E_{nk}}(x', y, z)e^{ikx} \tag{2.10}$$

Where x' runs between $-a/2$ and $a/2$, k is the wavevector, n is the band index and $x = n\ \Delta x + x'$. Obviously, if $\Delta x = 0$ we reduce ourselves to the smooth waveguide case where the periodic function is only a function of y and z. The band index ranks, from low to high, each eigenfunction according to its associated eigenvalue. An example of different bands are those determined by the mirror symmetries defined by the matrix $\mathcal{M}$. In Equation 2.8 we have defined the eigenvalue $\mathcal{M}$ associated to the $\mathbf{E}$ and $\mathcal{M} \times sig(z)$ to $\mathbf{B}$. None the less it is easy to demonstrate that the opposite is also true. As a result, we expect that at least two bands, should exist, with orthogonal fields and associated to the even $\mathcal{M}$ or odd $\mathcal{M} \times sig(z)$ symmetry operator. Of course we can build an ideally infinite number of bands with progressively higher energy.

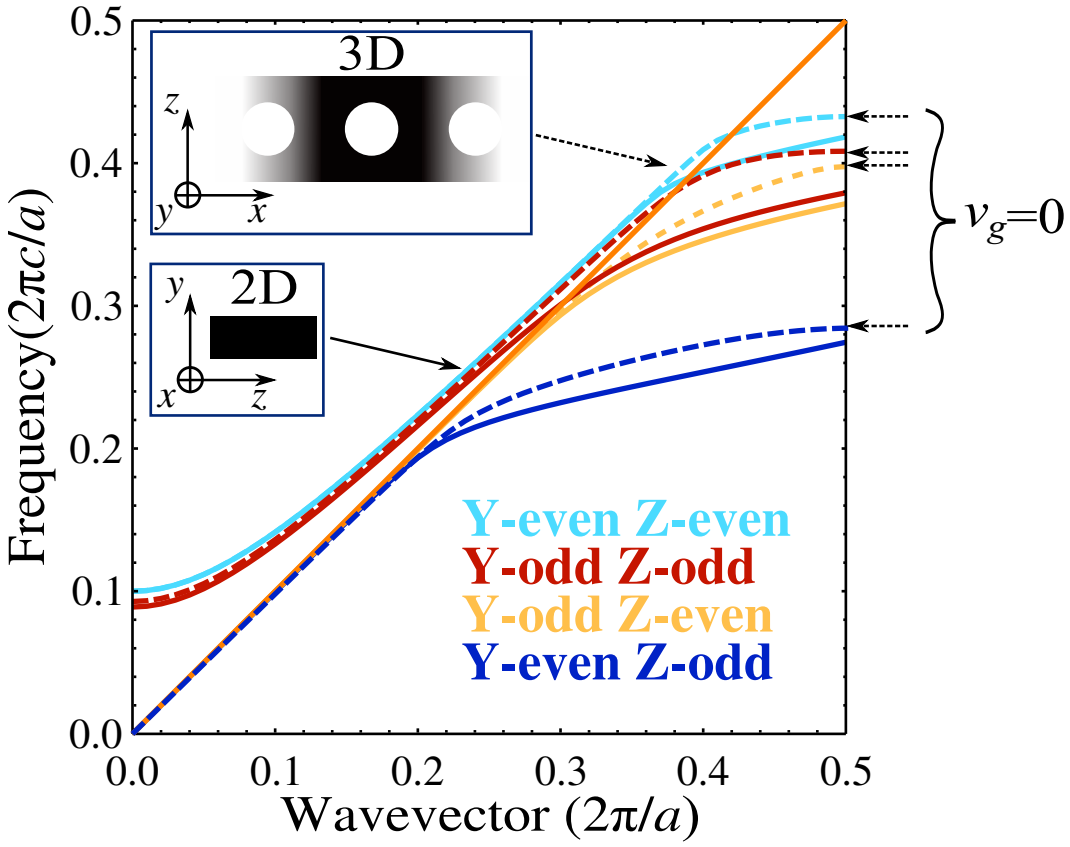

Figure 2.1: Dispersion diagram for the four first modes, in order frequency ω, of the two geometries shown in inset. We use smooth line for 2D dielectric waveguide with constant rectangular cross-section ($a \times 0.4a$) and dashed lines for the periodic waveguide with identical cross-section to the 2D case and periodically perforated by air-made cylinders of radius $0.25a$.

However, at a given k, modes can only be considered localized if $(\omega/c)^2 < |k|^2$. If such condition is broken, that is to say the band crosses what is usually called *light line* ($(\omega/c)^2 = |k|^2$), the modes become *radiative* or *leaky* mode, characterized by complex values of ω. It follows that the whole discussion section 2.2.1 is no longer valid since, obviously, the operators associated to such modes are no longer Hermitian [19]. In Figure 2.1 we show an example of dispersion diagram for the fundamental modes associated to each of the four possible mirror symmetries of the geometries shown in inset. We consider both a smooth waveguide with rectangular cross-section and a periodically perforated one with identical cross-section. Since the characteristic of the fields are going to be analyzed in great detail in the following chapters here we

limit to observe the main difference in the dispersion of both cases. There are three main features that we need to highlight. First in a smooth waveguide can run freely from $k = 0$ to $k = \infty$, even if in Figure 2.1 we only show the dispersion diagram up to $k = \pi/a$ for convenience. In this case increasing k is equivalent to a proportionally increase of the dimension of the waveguide. However for the periodic dielectric waveguides k is usually defined between 0 and π/a due to the Bloch theorem in combination with the *time-reversal invariance*, which states that $\omega^*(k) = \omega(-k)$. We also notice that, at the band edge ($k = \pi/a$), $v_g = \partial\omega/\partial k$, which represents the speed of energy flow though the waveguide, goes to 0. This phenomenon is called slow light [20] and implies that the amount of electromagnetic energy per unit-length inside the waveguide for non 0 input-power (P) increases as v_g decreases following the relation:

$$U = Pa/v_g. \tag{2.11}$$

None the less, in a finite systems, 0 group velocity means no energy flow since, because of the perfect match between the periodicity of electromagnetic signal and the system itself, all input power will be reflected. In fact, in the next chapter we will demonstrate that it is more convenient to work *close* rather than *at* the band-edge. Demonstrating that, at the band edge, $v_g = 0$ is quite straight forward. We do so by letting k range from $-\infty$ to ∞ by writing $k = mG + k'$, where k' is defined between $-\pi/a$ and π/a and $G = 2\pi/a$. If we expand $\mathbf{E}(k, r)$ we will now find:

$$\mathbf{E}(mG + k', x) = \mathbf{E}_{\mathbf{mG+k'}}(r)e^{imGx}e^{ik'x} = \mathbf{E}_{\mathbf{k'}}(r)e^{ik'x}. \tag{2.12}$$

The last step is possible because, in order to satisfy the Bloch theorem, $\mathbf{E}_{\mathbf{k}}(r)$ needs to be a periodic function along the direction of propagation x, which also satisfied by $\mathbf{E}_{\mathbf{mG+k'}}(r)e^{imGx}$. Since $\mathbf{E}(k, x)$ is periodic along x as well as k, we can look at the ω as we approach from $k^+ = \pi/a + \Delta k$ and $k^- = \pi/a - \Delta k$. It is obvious that, as a consequence of the periodicity and time-reversal invariance, $\omega(k^+) = \omega(k^+ - G) = \omega(-k^+) = \omega(k^-)$, which implies that:

$$\lim_{x\to 0} \Delta\omega/\Delta k = \lim_{x\to 0}(\omega(k^+) - \omega(k^+))/(k^+ - k^-) = 0. \tag{2.13}$$

2.2.3 $k \cdot p$ theory for electromagnetism

While these insights give us some information about the basic characteristics of optical forces it would be quite useful if we had a more intuitive relation between the eigenmode field distribution $\mathbf{E}$ and group velocity. A relatively

simple formula is given in [15, 21], where the group is found to be related to the electric and magnetic field as:

$$v_g = \frac{Re\left(\int_V \mathbf{E}^* \times \mathbf{B} dV\right)}{\frac{1}{2}\int_V |\mathbf{H}|^2 dV + \frac{1}{2}\int_V |\mathbf{E}|^2 dV}. \tag{2.14}$$

The denominator is the classical electromagnetic energy of the system, which according to Equation 2.6 is usually set to unity. As a consequence we find that the group velocity is the electromagnetic energy flowing (integral of the pointing vector) inside the unit cell per unit energy. However, even if Equation 2.14 allows us to measure the group velocity once the electric and magnetic fields are known, it tells us very little about the relation between field distribution and group velocity. A step forward can be done via $k \cdot p$-theory applied to electromagnetism, although we find it useful only in two dimensional systems.

$k \cdot p$ theory is very popular perturbative method, usually used to calculate the band dispersion and effective masses as well as extrapolating the band structure over the entire Brillouin zone of crystalline solids [22]. In photonics, however, it is not commonly used. Following perturbation theory applied to k and ω applied to Equation 2.2 and using Equation 2.10 to describe the wave-function, we can write:

$$\nabla \times \nabla \times \mathbf{E}_{\mathbf{k}'}(r) e^{i\mathbf{k}'\cdot\mathbf{r}} = -\varepsilon(r)\left(\frac{\omega'}{c}\right)^2 \mathbf{E}_{\mathbf{k}'}(r) e^{i\mathbf{k}'\cdot\mathbf{r}}. \tag{2.15}$$

Which, since $\nabla \times \nabla \times = \nabla(\nabla\cdot) - \nabla^2$, $k' = k + dk$ and $\omega' = \omega + d\omega$, at the first order becomes:

$$\begin{aligned} (\nabla^2 + 2i\mathbf{k}\cdot\nabla + |\mathbf{k}|^2)\mathbf{E}_{\mathbf{k}}(r) &= -\varepsilon(r)\left(\frac{\omega}{c}\right)^2 \mathbf{E}_{\mathbf{k}}(r) \\ (2id\mathbf{k}\cdot\nabla + 2|\mathbf{k}||d\mathbf{k}|)\mathbf{E}_{\mathbf{k}}(r) &= -\varepsilon(r)\frac{2\omega d\omega}{c^2}\mathbf{E}_{\mathbf{k}}(r). \end{aligned} \tag{2.16}$$

Where we used the fact that, according to perturbation theory, just as the eigenvalues, the wave-function $\mathbf{E}_{\mathbf{k}+\mathbf{dk}}(r) = \mathbf{E}_{\mathbf{k}}(r) + d\mathbf{E}_{\mathbf{k}}(r)$. By remembering that for two dimensional system $\mathbf{k} = \{k_x, 0, 0\}$ and $\mathbf{E}_{\mathbf{k}}(r) = \mathbf{E}_{\mathbf{k}}(y, z)$ we obtain:

$$\frac{d\omega}{dk_x} = v_g = \frac{k_x c^2}{\omega}\frac{\int_v |\mathbf{E}(\mathbf{k_x}, \mathbf{r})|^2 dV}{\int_v \varepsilon(r)|\mathbf{E}(\mathbf{k_x}, \mathbf{r})|^2 dV} \tag{2.17}$$

Where $|\mathbf{E}(\mathbf{k}, \mathbf{r})| = |\mathbf{E}_{\mathbf{k}}(\mathbf{r})|$ by definition. Equation 2.17 can be interpreted as a measurement of the amount of field distributed inside or outside the high refractive index regions (ε_2). In fact, if we assume that none of the fields

penetrate the waveguides, $v_g = c/n_1$, where n_1 is the refractive index of media surrounding the waveguides. That is to say the fields are not localized and the group velocity is equal to the phase velocity of the surrounding media. On the contrary, if the fields (or most of them) are localized inside the waveguides, we find that $v_g \approx c/n_2$. This also gives us some useful insight about the lower limit value of the group velocity: in two dimensional systems the group velocity can only be as low as the phase velocity in the media with the largest refractive index. This usually happens for large enough wave-vectors where the wavelength of light becomes much smaller than the features of the waveguides themselves so that, for all intents and purposes, the light behaves as if it were propagating inside an infinite media with refractive index n_2. This is a simple and useful tool that will be used in Chapter 3 to explain the behavior of the group velocity for different separations between two parallel waveguides.

2.3 Numeric tools

2.3.1 Plane wave basis Eigensolver - MPB

Now that we have described the basic mathematical properties of the eigenvalue formulation of Maxwell equations, we can move forward to consider some method to solve such equations in both periodic and non-periodic systems. The most used numeric tool thought out this thesis is MPB, a freely available block-iterative eigensolver on a plane-wave basis. While, so far, we have used the electric field only, MPB works by using the magnetic field $\mathbf{H}$ instead. This is quite useful in photonics, where most of the materials used for fabrication of such structures are pure dielectrics and, as a result, $\mathbf{H}$ is continuous over all boundaries. In a similar procedure to what was done for $\mathbf{E}$ we can rewrite the eigenvalue problem for $\mathbf{H}$ as:

$$\nabla \times \frac{1}{\varepsilon(r)^{-1}} \nabla \times \mathbf{H}(r) = \left(\frac{\omega}{c}\right)^2 \mathbf{H}(r). \tag{2.18}$$

The choice of a plane-wave expansion is justified by the fact that such base can be computed quite quickly by making use of FFT (Fast Fourier Transformed) algorithm and, most importantly because it intrinsically satisfies the transversality of the fields, which is imposed by the lack of free magnetic charge $\nabla \cdot \mathbf{H} = 0$. In order to better understand the core conceptual decomposition of the electromagnetic eigenproblem, let's take a look at the properties of the Fourier transformed of a periodic function such as the periodic part of

Equation 2.18.

$$\mathbf{H_k}(\mathbf{r}) = \int \mathbf{c_k}(\mathbf{q}) e^{i\mathbf{q}\cdot\mathbf{r}} d^3\mathbf{q}, \tag{2.19}$$

where $\mathbf{c}(\mathbf{q})$ are the coefficients of the Fourier transformed on a plane-wave basis with wavevector $\mathbf{q}$. Moreover, Equation 2.19, is required to be periodic on a lattice, so that:

$$\mathbf{H_k}(\mathbf{r}+\mathbf{R}) = \int \mathbf{c_k}(\mathbf{q}) e^{i\mathbf{q}\cdot(\mathbf{r}+\mathbf{R})} d^3\mathbf{q} = \mathbf{H_k}(\mathbf{r}) = \int \mathbf{c_k}(\mathbf{q}) e^{i\mathbf{q}\cdot\mathbf{r}} d^3\mathbf{q}. \tag{2.20}$$

It follows that, in order for Equation 2.20 to be valid, either $\mathbf{c_k}(\mathbf{q}) = 0$ or $e^{i\mathbf{q}\cdot\mathbf{R}} = 1$ and the former is a sub-case of the later, which implies that Equation 2.20 is true if $e^{i\mathbf{q}\cdot\mathbf{R}} = 1$: that is to say for those wave-vectors such as $\mathbf{q} = 2m\pi/\mathbf{R}$ (m is an integer) usually called *reciprocal lattice vectors*. Since G vectors form a lattice of their own, we can express the periodic part of the electric field as a weighted sum over the reciprocal lattice vector space

$$\mathbf{H_k}(\mathbf{r}) = \sum_G \mathbf{c_G}(\mathbf{k}) e^{i\mathbf{G}\cdot\mathbf{r}}. \tag{2.21}$$

By applying the transversality constrain to Equation 2.21 we find the simple constrain: $(\mathbf{k}+\mathbf{G})\cdot\mathbf{c_G}(\mathbf{k}) = 0$. It is obvious that not only will the sum of two vectors $\mathbf{c_G^1}$ and $\mathbf{c_G^2}$ still respect the transversality constrain, but any field distribution formed by a sum of transverse plane waves will still be transverse. As a consequence we can proceed disregarding the transversality condition which becomes an intrinsic property of the chosen basis. In order to project Equation 2.18 on a plane-wave basis we simply take its Fourier transform and substitute the periodic par of $\mathbf{H}$ with Equation 2.21, which yields:

$$\sum_G \left[-\varepsilon^{-1}_{\mathbf{G}'-\mathbf{G}} \cdot (\mathbf{k}+\mathbf{G}') \times (\mathbf{k}+\mathbf{G}) \times\right] \mathbf{c_G} = \frac{\omega^2}{c^2} \mathbf{c_{G'}} \tag{2.22}$$

This equation can now be solved by approximating $\varepsilon^{-1}_{\mathbf{G}'-\mathbf{G}}$ via the Discrete Fourier Transform. Finally we have reduced Equation 2.18 to a simple linear-matrix, eignevalue problem, which can be solved in several ways. MPB, as we have previously mentioned uses a block-iterative method [23], that is to say, it finds the lowest order eigenmode first, and then, by requiring orthogonality, if finds the remaining ones one by one. In general MPB is a very reliable, versatile and efficient computational tool for calculating photonic bands of dielectric photonic systems.

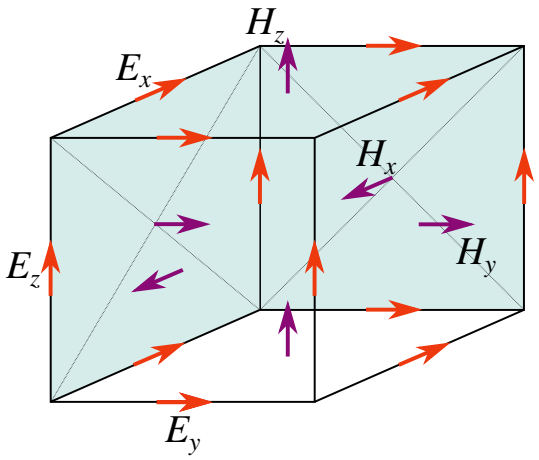

Figure 2.2: Representation of the Yee grid for a single voxel. As can be seen electric and magnetic fields are sampled in different Cartesian coordinates: the **E**-field is sampled along the edges of the voxel while the **H** is sampled at the center and normally to its faces.

2.3.2 FDTD method

In the last chapter of this thesis we have also made use of FDTD techniques. The Finite Difference Time Domain (FDTD) is the workhorse of computational photonics since it is extremely malleable and reliable computational method for solving Maxwell equations [24]. This method is well suited for treating nearly any know material, like non-isotropic, lossy and non-linear materials as well as moving objects, non-homogeneous structures and other effects like Casimir forces or quasi crystalline structures. Both periodic and absorbing boundary conditions are allowed. The major drawback of the FDTD method, albeit its strength too, is the regular Yee grid over which Maxwell equations are solved. A regular grid is a powerful tool that allows all the features we have previously mentioned, whoever, it quickly scales in memory requirements and computational time. This is especially true when studying structures with features that are significantly smaller than the average wavelength of the spectral region of interest, like is often the case when using metals, or large structures like random photonic systems. For all this cases a rather high resolution is often required since the increased resolution will not be shape specific but will be homogeneously distributed so that the computational time required increases roughly with the fourth power of the resolution. On the up side FDTD is a time-domain technique and it is best suited for time-dependent simulations or when a large range of frequencies are of interest. In this case a

single broad band pulse can be used and all the spectral information can be extracted with a single simulation. FDTDs, just like any other finite different method, works by meshing the simulations space in order to solve the spatial derivative of Maxwell equations. If we took a look at them, we could see that, at a given point, a change of the **E**-field in time depends on the curl of **H** at the same point and vice versa. While a time stepping procedure with such work flow might seem simple to implement, in higher dimensions the implementation of the numerical curl on a regular grid is problematic. The solution of this problem was proposed by Kane Yee in 1966 [25] by sampling different components of the electric and magnetic field at different points in the Cartesian space, like shown in Figure 2.2, which allows for second order accuracy in homogeneous regions. However, only first order accuracy can be obtained in non-homogeneous regions and special smoothing or multi graded mesh might be required to gain back second order accuracy. For such purpose several techniques like sub-meshing or sub-pixel smoothing can be used in order to improve accuracy.

2.4 Optical forces as a surface integral

In this section we will describe the fundamental nature of optical forces. At first, we will describe the classical Maxwell stress tensor formulation of optical forces [5] and then, we will consider a formulation based of perturbation theory for Maxwell equations and thermodynamics.

2.4.1 Maxwell stress tensor

The Maxwell stress tensor is by far the best know formulation of optical forces although not the only one. However, this is unimportant for our porpoise since, as we will do in the following chapters, we only consider non deformable dielectric media immersed in air or, at least, we require that the actual geometrical deformation does not significantly changes the refractive index of the system under study. The Maxwell stress tensor is derived from the Lorentz force which is usually written as:

$$F = \int_V (\rho\ \mathbf{E} + \mathbf{J} \times \mathbf{E})\ dV = \int_V f\ dV. \tag{2.23}$$

Where ρ is the charge density and **J** is the current density. Of course this two are measurable quantities, however, we would like to look for a functional form of the force that depends on ε and some more familiar elements like energy

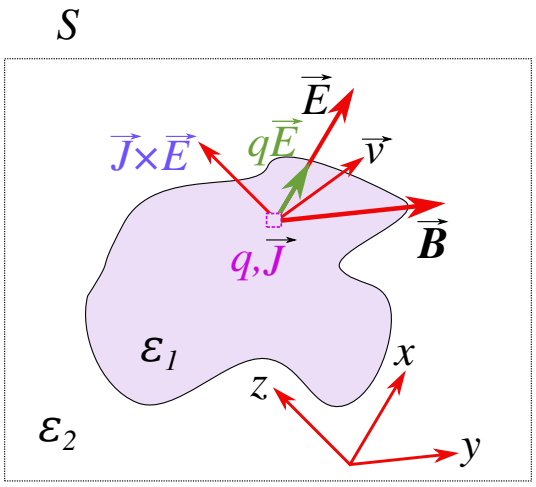

Figure 2.3: Representation of the optical forces acting on an unit element with charge q and current $\mathbf{J}$.

and flux. To do so we rewrite the charge and current density via Gauss and Ampere's law so that Equation 2.23 becomes:

$$f = (\nabla \cdot \mathbf{E})\mathbf{E} + \nabla \times \mathbf{B} \times \mathbf{B} - \frac{\partial \mathbf{E}}{\partial t} \times \mathbf{B}. \tag{2.24}$$

By expanding the time derivative with the product rule and using Faraday's induction law we can get:

$$f = [(\nabla \cdot \mathbf{E})\mathbf{E} + \mathbf{E} \times \nabla \times \mathbf{E}] + [(\nabla \cdot \mathbf{B})\mathbf{B} + \mathbf{B} \times \nabla \times \mathbf{B}] - \frac{\partial}{\partial t}(\mathbf{E} \times \mathbf{B}). \tag{2.25}$$

Where we added the $(\nabla \cdot \mathbf{B})\mathbf{B}$ to obtain a symmetry between $\mathbf{E}$ and $\mathbf{B}$. Finally by using, in order, the vector calculus identity $\frac{1}{2}\nabla(\mathbf{A} \cdot \mathbf{A}) = \mathbf{A} \times (\nabla \times \mathbf{A}) + (\mathbf{A} \cdot \nabla)\mathbf{A}$ and $\nabla(\mathbf{A} \otimes \mathbf{B}) = (\mathbf{A} \cdot \nabla)\mathbf{B} + (\nabla \cdot \mathbf{B})\mathbf{A}$ we obtain:

$$f = \nabla \cdot \mathcal{T} - \frac{\partial \mathbf{S}}{\partial t}. \tag{2.26}$$

Where $\mathcal{T}_{ij} = E_i E_j + B_i B_j - \frac{1}{2}(|\mathbf{E}|^2 + |\mathbf{B}|^2)\delta_{ij}$ commonly known as the Maxwell Stress tensor and $\mathbf{S}$ is the Poynting vector. If we try to obtain the total force acting over an object, as shown in Figure 2.3, where we plotted an object of arbitrary shape and refractive index ε_1, immersed in a media with refractive index ε_2, we find that the total force will be given by a surface integral over a surface (S in Figure 2.3) surrounding the object and the space integral of the

time derivative of the pointing vector. However, in the frequency domain, the time derivative of the Poynting vector will add an $i\omega$ term to the space integral so that, when the time averaged force is measured, the electromagnetic power flow will give no net contribution to optical forces and the only contribution to the force arises from the surface integral of $\mathcal{T}$. While we have assumed that $\varepsilon_2 \geq 1$, Equation 2.26 is in fact only really correct when $\varepsilon_2 = 1$. For $\varepsilon_2 > 1$ the Maxwell stress tensor is only a component of the force and the mechanical interaction of the light with the system cannot be disregarded [4].

2.4.2 Optical Torque

Optical force can also induce Torque [26]. This should be at least possible when the geometric disposition of the dielectric masses is not mirror symmetric. The derivation of the optical torque via Maxwell stress tensor can be derived easily as:

$$f = \nabla \cdot \mathcal{T} \times \mathbf{r}. \tag{2.27}$$

Where $\mathbf{r}$, by definition of torque, is the vector that joins every point to the center of mass. We can rewrite Equation 2.27 in index notation as:

$$l_k = (\nabla \cdot \mathcal{T}_j) r_i \epsilon_{ijk} \mathbf{e}_k. \tag{2.28}$$

Since $\mathcal{T}_j$ is a vector and r_i is a scalar, we make use of the following property of the divergence $\nabla \cdot (A\mathbf{B}) = (\nabla A) \cdot \mathbf{B} + A \nabla \cdot \mathbf{B}$.

$$l_k = \nabla \cdot (\mathcal{T}_j r_i \epsilon_{ijk} \mathbf{e}_k) - (\nabla r_i \cdot \mathcal{T}_j) \epsilon_{ijk} \mathbf{e}_k. \tag{2.29}$$

Now, by remembering that $\mathcal{T}$ is a symmetric matrix and noticing that $\nabla r_i = \{1, 1, 1\}\delta_{ji}$, we find that $(\nabla r_i \cdot \mathcal{T}_j)\epsilon_{ijk}\mathbf{e}_k = 0$. So that, by integrating on a volume the total torque becomes:

$$L = \int_S \mathcal{T} \cdot (\mathbf{r} \times \mathbf{n}) dS. \tag{2.30}$$

This is a pleasant but expected surprise. In fact, since Equation 2.26, when integrated over a volume, tells us that, in the steady state, all the forces inside such volume will cancel themselves out only leaving their contribution at the surface of the volume, it is reasonable to assume that also the torque, which is generated by such forces will only have non zero contributions only at its surface.

2.4.3 Surface integral formulation of optical forces

While the Maxwell stress tensor is a solution to our problem it gives little or no information about the characteristic of the forces because of the complexity of its functional form. Here we demonstrate that an alternative formulation (indeed one of many [27]) of optical forces, with a more clear meaning, can be derived with few, simple steps. In fact, while this formulation is derived from perturbation theory and the concepts developed in section 2.2.1, an identical result can be reached from Equation 2.23 as we will show in Chapter 5. For non-deformable objects and assuming translations along the z-axis the mechanical force can be written as:

$$F = -\frac{dU}{dz}. \tag{2.31}$$

Where U is the potential energy of the system. In electrodynamics and non lossy media the only source of energy is of electromagnetic origin so that U is the energy of the fields $N\hbar\omega$. By substituting this into Equation 2.31 we obtain [28]:

$$F = -\frac{1}{\omega}\frac{d\omega}{dz}U. \tag{2.32}$$

This simple equation, at first, would seem better suited to the analysis of optical forces in photonic crystal structures since, as we have shown in section 2.2.1, most of the theoretical framework of such field has been developed to deal with entities like ω, k and v_g rather than the electromagnetic field distribution. However, after some thought, we realize that Equation 2.32 is as obscure as Equation 2.26 was. Obviously, ω can only be calculated (except for few elementary cases) via numeric solvers so that we are still clueless on the relation between the geometry of the specific geometry of the system. Fortunately, Equation 2.32, can be rewritten via perturbation theory for electromagnetism [29] as a surface integral that only depends on ε and $\mathbf{E}$.

By applying classical perturbation theory to Equation 2.2, at the first order, in the limit of infinitesimal displacements, we can obtain:

$$\frac{d\omega}{d\zeta} = \frac{\omega}{2}\frac{\int_V \mathbf{E}^* \frac{d\varepsilon}{d\zeta}\mathbf{E}\, dV}{\int_V \mathbf{E}^* \varepsilon \mathbf{E}\, dV}. \tag{2.33}$$

Where ζ is a parametrization of the deformation of the system. In fact, we will now drop the constrain of rigid deformations and assume that the system can be deformed freely, as long as the refractive index does not change. We show an example of this in Figure 2.4, where the interface between two materials is shifted by $h(\zeta)$. Obviously, the denominator of Equation 2.33, according to

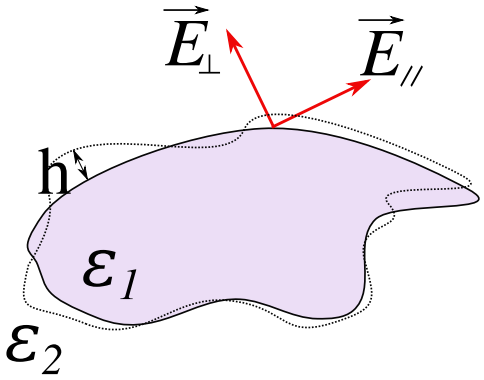

Figure 2.4: Schematic of the perturbation of the system where the boundaries between two different materials are shifted by an infinitesimal amount h which can change along the surface. We also show the component of the electric field normal and parallel to the initial surface.

section 2.2.1, can be set equal to 1 as this is the normalization of the fields we have agreed upon. Integrating the numerators it is not that easy. In fact, $\frac{d\varepsilon}{d\zeta}$ can only be non 0 at the interface between both materials, where according to classical electrodynamics the value of $\mathbf{E}$ is undetermined: the valued of the electric field component normal to the surface is doubly valued, according to where the E_{perp} is measured: inside $\varepsilon_1(E^1_{perp})$ or inside ε_2 (E^2_{perp}). In order to solve this problem, instead of sharp transitions from ε_1 to ε_2, we assume a smooth variation of ε_1 into ε_2. As a consequence, at each point on the boundary surface, the contribution to $d\omega$ will be given by a line integral that crosses the interface from x to $x + dx$ and, by choosing a correct smoothing function [30], even if not unique, we can obtain [29]:

$$\frac{d\omega}{d\zeta} = \frac{\omega}{2}\int_A \frac{\Delta\varepsilon}{2}\frac{dh}{d\zeta}\left(\left|E_\parallel\right|^2 + \frac{1}{\varepsilon_1\varepsilon_2}\left|D_\perp\right|^2\right)\, dA. \tag{2.34}$$

Where $\Delta\varepsilon = (\varepsilon_1 - \varepsilon_2)$, $E_\parallel$ and $D_\perp$ represent the electric and electric-displacement fields parallel and normal to A, which is the surface of integration and $\mathbf{n}$ is a vector, directed into ε_2, and normal to A. Equation 2.32 now becomes:

$$\frac{\mathbf{F}}{U} = \int_A \frac{\Delta\varepsilon}{2}\left(\left|E_\parallel\right|^2 + \frac{1}{\varepsilon_1\varepsilon_2}\left|D_\perp\right|^2\right)\mathbf{n}\, dA. \tag{2.35}$$

Where we impose back the condition of rigid translations by setting $\frac{dh}{d\zeta} = \mathbf{n}$. As we can notice from Equation 2.33 and Equation 2.35, this derivation is more of an a posteriori description of the force rather than an actual measurement

of it. In fact, the measured quantity, is the change of eigenfrequency, which is a scalar value unlike $\mathbf{F}$, which is a vector. For rigid translations along the axis this is not a problem since a displacement of an object in a group is equivalent to an opposite displacement of the group itself. For example, if we had two parallel waveguides, and moved one of them of a quantity dz along the z-axis, this would be equivalent to moving the remaining waveguide by $-dz$ or moving both of them of a quantity $dz/2$ and $-dz/2$ respectively. This is no longer true if we consider another rigid deformation of the system: rotations. Rotating one of the waveguides of an angle θ is not necessarily equivalent to a rotation of the other waveguide of an angle $\pm\theta$ (unless the two are identical) or to a rotations of both of half the angle. Even more if we also consider non rigid deformations, the force, according to Equation 2.34, should depend on the deformation itself. This is clearly not right when very slow mechanical deformations are considered since the instantaneous optical force, although it might not be decouple from its mechanical counterpart, should only be a function of the instantaneous field distribution. In fact, a correct interpretation of Equation 2.34, is as a measure of the work done on the electromagnetic fields by an external force which deforms the geometry arbitrarily so that, in order to obtain the correct value of the force, that is to say to measure how will the system deform due to the optical force, we have to guess the correct deformation to apply to the system first. Obviously, in case of rigid translations, this is straight forward. In Chapter 3 we will discuss the advantages of Equation 2.35 over Equation 2.32 and Equation 2.26 for the case of rigid translations. Moreover, in Chapter 5 we will demonstrate that this equation can be derived directly from Equation 2.23, which extends its use to non-dielectric media and not periodic structures.

2.5 Normalized units and optical forces

As we have previously mentioned, here we use the Lorentz-Heaviside unit system as applies to MPB and MEEP [10, 11]. While dimensionally both programs share the same unit system they do not share normalization, which can make them slightly difficult to compare in a direct analysis. However, when we get to use Meep for force measurements as in Chapter 5, we are more interested in a proof of concept than the actual magnitude so that we prefer using arbitrary units. However, it is useful for the reader to understand the link between the normalized forces that we commonly use and the actual magnitude of the force. A fast and simple derivation can be obtained from

Equation 2.32 and Equation 2.11 so that we can obtain:

$$\frac{F}{P} = \frac{L}{\omega v_g}\frac{d\omega}{ds}. \tag{2.36}$$

Since we almost always use normalized units, which allow us not using specified sizes since Maxwell equations are scalable [15], we will usually express length and group velocity in S.I. as $s/a = s^m$ and $v_g/c = v_g^m$, where s^m and v_g^m are the normalized units commonly used along this paper. For commodity we also assume that $L = a$ so that Equation 2.36 becomes:

$$F = \frac{a}{\omega v_g^m}\frac{d\omega}{ds^m}\frac{P}{ac}. \tag{2.37}$$

This equation clearly states the relation between the normalized unit system we use and the magnitude of the force in Newtons. The only thing we have left is finding the actual length of a at a given frequency. In Equation 2.37 the frequency is "self-normalized" by $d\omega/\omega$, however in Lorentz-Heaviside units, frequency and wavelength are normalized too. Since the speed of light in vacuum is fixed to 1, we can write:

$$\frac{\lambda_0\omega_0}{\lambda\omega} = 1. \tag{2.38}$$

Where we simply assume a reference wavelength (λ_0 and ω_0 in S.I.) and frequency that satisfy this equation. It is then streight forward to define $\lambda^m = \lambda_0/\lambda$ and $\omega^m = \omega_0/\omega$ so that:

$$\lambda^m = \frac{\lambda_0}{\lambda} = \frac{\omega}{\omega_0} = \frac{1}{\omega^m}. \tag{2.39}$$

Since the wavelength λ is effectively an unit of length, we can set $\lambda^m = a^m$ and $\lambda = a$. The actual relation between length in international units and frequency or wavelength of light will be given by the refractive index used. In fact, for dispersive media, epsilon is a function of frequency so that the value of ω is in S.I. is given by $\epsilon(\lambda)$, where we conveniently substitute frequency with wavelength since both of them are free space quantities and thus invariant for any system taken into consideration. Once this is known we have that

$$\lambda/\omega^m = a, \tag{2.40}$$

which links the normalized frequency to the length in S.I. Normalized units are very convenient to handle numerically, not only because it simplifies the unit system, but because it allows us to focus on the geometrical proportions of each geometry rather than on its absolute dimensions.

2.6 Refractive index modulation techniques

While most of our studies will be concern with tailoring forces via specific geometries, we also consider the possibility of using changes in the refractive index to manipulate the amplitude and direction of the forces. This is particularly useful since most of these methods are reversible: after some time the system will return to its unperturbed state and a new type of perturbation might be chosen. In this thesis we will make use of free carrier injection [31] because, it was conceptually more familiar to us, however other techniques might be used to modulate the refractive index of dielectric materials temporarily like the Thermo-optic effect [32], the Electro-optic effect [33] or acoustic waves [34].

2.6.1 Free carrier injection

Free carrier injection allows us to change the refractive index of media by modifying its free carrier density by adding free electrons above the conduction band. This is usually done by removing electrons from the valence band via optical excitation. Such process is nearly instantaneous and the effect will last until all the electrons have decayed to their initial state [35]. It is also relatively simple to implement since it can be done by simply focusing a laser on the region of interest without need for fabrication of heaters or electric contacts. On the down side such a variation of the refractive index is not painless: after the absorption process has finished, the induced free carriers will recombine, mostly non-radiatively, producing heat that will itself modify the refractive index and, in our case, possibly produce unwanted mechanical stress on the system. The free carrier lifetime and the amount of heat generated changes significantly according to the materials used. In order to describe the effect of carrier injection in the conduction band we use the Drude model where free electrons are modeled via a driven harmonic oscillation:

$$m_{el}\frac{d^2x(t)}{dt^2} - \frac{m_{el}}{\tau_{el}}\frac{dx(t)}{dt} = -eE(t,\omega). \tag{2.41}$$

Where $x(t)$ is the amplitude response of the oscillator, e is the electric charge, τ_{el} is the relaxation time of the free electrons and m_{el} is the effective mass. For a time harmonic driving force $eE(t,\omega)$ of frequency ω, $x(t)$ has the following solution:

$$x(t,\omega) = \frac{e}{m_{el}}\frac{E(t,\omega)}{\omega^2 + i\omega/\tau_{el}}. \tag{2.42}$$

As the oscillator is driven by the $E(t)$, the moving charge generates its own electric field usually denominated as polarization $P = -eN_{el}x(t)$, where N_{el}

is the carrier density. The total electric field becomes $D(t) = P(t,\omega) + \varepsilon_0\varepsilon_d E(t,\omega) = \varepsilon_0\varepsilon'_d(\omega)E(t,\omega)$, where ε_d is the unexcited dielectric function and

$$\varepsilon'_d(\omega) = \varepsilon_d - \frac{eN_e}{m_{eff}}\frac{1}{\omega^2 + i\omega/\tau_{el}} \tag{2.43}$$

is the dielectric function after carrier injection. Also, since we excite the medium optically, for each electron exited to conduction band we generate an equal number of hole in the valence band so that the effective mass will be given by the sum of the inverse of the holes and free carrier effective masses m_e^* and m_h^* respectively. As it can be seen from Equation 2.43, via carrier injection we only can reduce the initial dielectric function and, in addition, a certain amount of loss will be added to the system. In other words, as free carriers are injected dielectric materials will become "slightly" metallic and, since metals are usually characterized by negative refractive index, it makes sense that the resulting effect of both contributions is a reduction of the initial dielectric function and loss. However, we also notice that the added loss is quite small, and only significant if in the presence of slow light or cavity modes. Fortunately, for the system used in Chapter 5, the induced loss has negligible effects.

2.6.2 Thermo optical effect

In this case it might be more reasonable to use other techniques such as the thermo-optic effect. The thermo-optic effect should induce no losses since temperature effects mainly reduce the density of the material while no free charge is induced. However, unlike free carrier injection, heat transfer is slow and dissipation of heat in the system can take up to few microseconds, depending on the dimensions and temperature gradient of the system. We should also mention than the thermo-optic change of the refractive index is also a byproduct of free carrier injection, as we have mentioned before, due to the heat produced by the carrier recombination. In optomechanical systems, thought, heat induced deformations as well as heat transfer should be taken into consideration since the moving parts are suspended and not in direct contact with the heat treated region. An efficient evaluation of such effect is quite challenging and still an area of open research [36]. On the positive side the thermo-optical effect induces larger changes to the refractive index compared to free-carrier injection, and thus, it should be more effective for our porpoises.

2.7 Partial differential equations of motion

So far we have treated optical forces and the basic properties of photonic structures since our main interest lays on the photon management via optomechanics. However, a proper description of such effect would not be complete without, at least, a basic description of the mechanical properties, both physical and mathematical, of the system we will focus on. In this section we will introduce the partial differential equation that describes the time and space depended motion of a double clamped beams and discuss its most simple solution. Our discussion closely follows [37].

2.7.1 Beam deformation

For commodity, and since our major interest lays on the manipulation of optical forces rather than on the characteristic of the mechanical reaction induced by them, we will only consider the most simple description that still gives us the information we required. Throughout our work we only consider beams or plates which, mechanically, can be described by the same partial differential equation. The simplest description of the dynamics of a beam is schematically described in Figure 2.5. This description basically approximates the beam or plate to a infinite number of non-deformable "blocks" with infinitesimal thickness dx. The actual geometrical characteristics, cross sectional geometry for a beam and thickness for plates, is described via a parameter called flexural stiffness $EI(x)$, where E is the Young modulus of the material and $I(x)$ is an exclusive function of the cross-sectional shape of the object at a given value of x. Another important parameter is $p(x,t)$, which in this case represents the load over the structure. In this approximation the non-deformable "blocks" are subjected to the forces shown in the inset of Figure 2.5. The equation of motion for such system can be readily found by considering the balance of the forces acting on a "block".

$$V + p\ dx - (V + \frac{\partial V}{\partial x}dx) - f\ dx = 0 \tag{2.44}$$

In which f is the inertial force, simple given by the product of the cross-sectional mass $m(x)$ and the local acceleration as $f = m(x)\partial^2 v(x)/\partial t^2$. The second equilibrium relation can be found by adding the momentum about the elastic axis:

$$M + V\ dx - (M\frac{\partial M}{\partial x}dx) = 0. \tag{2.45}$$

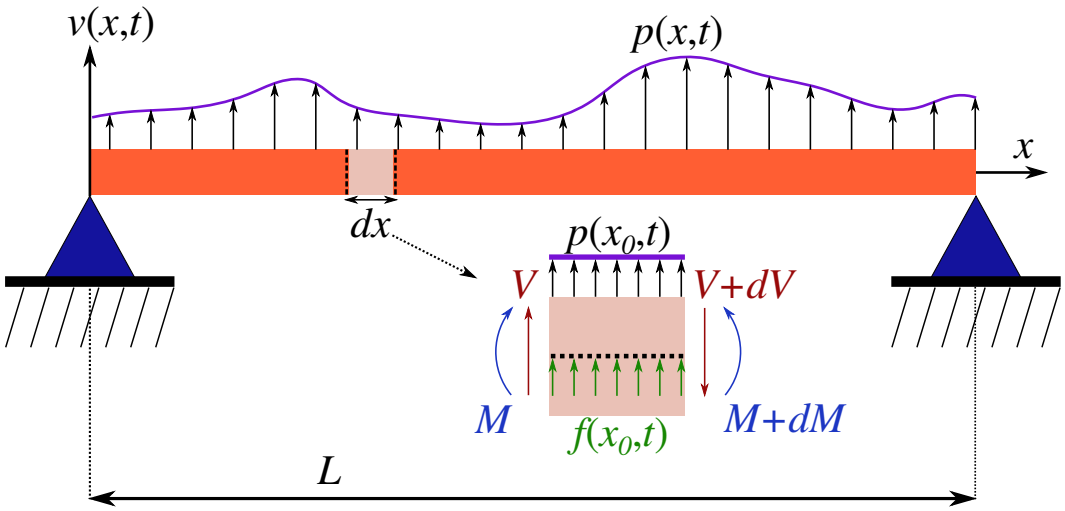

Figure 2.5: Schematics of a double clamped beam, with rigid point-contacts, subjected to loading and the forces acting upon it.

Where it can be demonstrated that the distributed lateral forces only provide a second order contribution to the total moment. Finally, combining these two equations we obtain:

$$\frac{\partial^2}{\partial x^2}\left(EI\frac{\partial^2 v}{\partial x^2}\right) + m\frac{\partial^2 v}{\partial t^2} = p. \tag{2.46}$$

Where v is the local displacement of the structure and we have imposed that $M = \partial^2 v/\partial x^2$, which is the basic relation between curvature and moment of elementary beam theory [37]. This partial differential equation is the simplest description of the mechanical dynamics of a nanobeam under time and space dependent loads, Young modulus, geometry and mass. Obviously, in Chapter 5 we will only take into account beams or plates with constant cross section and material composition. Other parameters can be added to this equation in order to improve its accuracy, like an axial contribution to the momentum of the force, shear deformations, rotatory inertia and, of course, damping, which can be either viscous, thermo-elastic or piezo-elastic.

2.7.2 Free vibration

We start by looking at the simpler case of free vibrations, that is to say solutions for which $p(x,t) = 0$, rather than directly looking for a general solution to Equation 2.46. Such solution can be obtained via a separation of variables

in which case $v(x,t)$ can be given as: $v(x,t) = \phi(x)Y(t)$. This is obviously an appropriate solution if we are looking for harmonic oscillations, moreover much like in section 2.2.1, any other generic function of time can be represented as the sum of harmonic ones. Equation 2.46, with some simple manipulations, now becomes:

$$\frac{1}{\phi(x)}\frac{\partial^4\phi(x)}{\partial x^4} + \frac{m}{EI\ Y(t)}\left(EI\frac{\partial^2 Y(t)}{\partial t^2}\right) = 0 \tag{2.47}$$

Where E, I and m are constant along x. Since the two terms in Equation 2.47 depend on different variables, this equation can be satisfied by independent values of x and t as long as both parts are equal to a constant K so that:

$$\frac{1}{\phi(x)}\frac{\partial^4\phi(x)}{\partial x^4} = K = -\frac{m}{EI\ Y(t)}\left(EI\frac{\partial^2 Y(t)}{\partial t^2}\right). \tag{2.48}$$

This equation can now be split in two independent functions of t and x as:

$$\begin{aligned} \frac{\partial^2 Y(t)}{\partial t^2} - \omega^2 Y(t) &= 0 \\ \frac{\partial^4\phi(x)}{\partial x^4} - a^4\phi(x) &= 0. \end{aligned} \tag{2.49}$$

Where:

$$\omega^2 = \frac{a^4 EI}{m} \quad \& \quad K = a^4 \tag{2.50}$$

The first row of Equation 2.49 is the familiar description of the undamped free harmonic oscillator and has the solution of the type:

$$Y(t) = A\sin(\omega t) + B\cos(\omega t). \tag{2.51}$$

The second row can be solved by assuming a solution of the type $\phi(x) = Ce^{lx}$, so that Equation 2.51 now becomes:

$$(l^4 + a^4)Ce^{lx} = 0. \tag{2.52}$$

The roots of the fourth order polynomial give us the values of $l = \pm a$ and $\pm ia$, which, by substituting in Equation 2.51, leads to:

$$\phi(x) = A_1\sin(ax) + A_2\cos(ax) + A_3\sinh(ax) + A_4\cosh(ax). \tag{2.53}$$

In which we have substituted the exponential terms with $\cosh(ax)$ and $\sinh(ax)$ and complex exponential ones with $\cos(ax)$ and $\sin(ax)$.

Now that we finally have a proper solution of $\phi(x)$ and $Y(t)$ we need to find the values of A, B and A_j. While we obviously cannot find all the parameters in the system since the value of some of them will be a function of the amplitude and phase of the oscillation, which are a function of the initial conditions of the beam, we can impose the fixed boundary conditions of the problem in order to reduce the remaining ones to a more suitable form. In Figure 2.5 the beam or plate is connected to the rigid holders (blue triangles) through a line so that, at the borders of the beam, $x = 0$ and $x = 0$, the forces must be 0 and there should be no deformation at such point:

$$\begin{aligned} \phi(0) &= 0 \\ M(0) &= EI\frac{\partial^2\phi(0)}{\partial x^2} = 0 \\ \phi(L) &= 0 \\ M(L) &= EI\frac{\partial^2\phi(L)}{\partial x^2} = 0 \end{aligned} \tag{2.54}$$

By substituting Equation 2.53 into Equation 2.54 the following conditions are derived:

$$\begin{aligned} A_4 + A_2 &= 0 \\ A_4 - A_2 &= 0 \\ A_1\sin(al) + A_3\sinh(al) &= 0 \\ A_1\sin(al) - A_3\sinh(al) &= 0. \end{aligned} \tag{2.55}$$

In which every condition its ordered as Equation 2.54. This leads to the conclusion that $A_2 = A_4 = 0$ and $A_1\sin(al) = A_3\sinh(al) = 0$. However, since $\sinh(al)$ cannot be 0, this implies that $A_3 = 0$. The remaining condition, $\phi(L) = A_1\sin(aL) = 0$, can only be true if $\sin(al) = 0$ and excluding the trivial condition $A_1 = 0$. Obviously, this only happens if $aL = n \times \pi$, where n is a positive integer. We can now obtain the oscillation frequency of each n since $a^4 = \omega^2 m/EI$ so that:

$$\omega_n = n^2\pi^2\sqrt{\frac{EI}{mL^4}}. \tag{2.56}$$

Instead the vibrational shape; spatial part of the solution of Equation 2.46, for the system shown in Figure 2.5 is:

$$\phi_n(x) = A_1\sin\left(\frac{n\pi}{L}\right). \tag{2.57}$$

This simple equation is a good representation of the transverse oscillation modes.

2.7.3 Orthogonality of modal shapes

Just as we have demonstrated for non lossy optical modes in section 2.2.1 mechanical modes are orthogonal to each order; which implies that no mechanical mode can excite another mechanical mode without an external perturbation and, ideally, that each mechanical mode could be exited independently from each other. A straight forward application of this concept can be found via *Betti's law*, which states that: *the work done by one set of loads on the deflection due to a second set of loads is equal to the work of the second set of loads acting on the deflections due to the first* [37]. In other words the inertia forces of a given mode m that create a load on the mode n, must be equal to the work done by the inertial force of the mode n acting on the mode m, so that:

$$\int_0^L v_m(x) f_{In}(x) dx = \int_0^L v_n(x) f_{Im}(x) dx \tag{2.58}$$

Where $v_i(x,t)$ is the displacement of the i^{th} mode, its derivative is $v_i(x,t) = \omega_i \phi_i(x) Y_i(t,\omega)$ and the inertial forces are $f_i = m(x)\omega_i^2 \phi_i(x) Y_i(t,\omega)$, according to the solution proposed in the previous section so that Equation 2.58 can be rewritten as:

$$Y_m Y_n \omega_n^2 \int_0^L \phi_m(x) m(x) \phi_n(x) dx = Y_n Y_m \omega_m^2 \int_0^L \phi_n(x) m(x) \phi_m(x) dx. \tag{2.59}$$

We would like to notice that in this section we allow the beam to have varying stiffness and mass along its length as well as arbitrary boundary conditions. Equation 2.59 can be simplified so that we obtain:

$$(\omega_n^2 - \omega_m^2) \int_0^L \phi_m(x) m(x) \phi_n(x) dx = 0. \tag{2.60}$$

Since by construction $(\omega_n^2 - \omega_m^2) \neq 0$, we obtain the orthogonality condition:

$$\frac{1}{N} \int_0^L \phi_m(x) m(x) \phi_n(x) dx = \delta_{mn}. \tag{2.61}$$

Where N is a normalization constant. A second orthogonality condition can be obtained by multiplying Equation 2.46 by ϕ_m and setting $p(x,y) = 0$:

$$\int_0^L \phi_m(x) \frac{\partial^2}{\partial x^2} \left(EI(x) \frac{\partial^2 v_n(x,t)}{\partial x^2} \right) dx = - \int_0^L \phi_m(x) m(x) \frac{\partial^2 v_n(x,t)}{\partial t^2} dx \tag{2.62}$$

and, by remembering that the time derivative of $v(x,t)$ is equal to $\omega_n \phi_n(x) Y(\omega, t)$, Equation 2.62 becomes:

$$\int_0^L \phi_m(x) \frac{\partial^2}{\partial x^2} \left(EI(x) \frac{\partial^2 \phi_n(x)}{\partial x^2} \right) dx = 0, \tag{2.63}$$

which can be integrated by parts twice gives:

$$\phi_m(x) V_n|_0^L - \frac{d\phi_m(x)}{dx} M_m \Big|_0^L + \int_0^L \frac{d^2\phi_m(x)}{dx^2} \frac{d^2\phi_n(x)}{dx^2} EI(x) dx = 0 \tag{2.64}$$

Where the first term of Equation 2.64 represents the work done at the extremities by the shear forces and moments of the mode m on the displacements and rotations of the mode n. For rigid boundaries like the ones represent in Figure 2.5 or free ones this terms vanish, however, for beams with discontinuous momentum of inertial, such as when a lumped mass is present at one end or elastic supports are used, this terms contribute to Equation 2.64.

2.7.4 Mechanical mode basis and uncoupled equations of motion

The orthogonality conditions presented in the previous chapter can be used to create an orthogonal basis in $\phi_m(x)$ and $Y_m(t)$, since an infinite number of vibrational modes exits, so that an arbitrary displacement of a beam can be transformed into a superposition of modal vibrations as:

$$v(x,t) = \sum_{i=1}^{\infty} \phi_i(x) Y_i(t). \tag{2.65}$$

We notice that our basis, while orthogonal, it is not normalized. In fact, we have not yet found a proper normalization of either of the orthogonality conditions. Finding a normalization term for Equation 2.61 is easy. However, by looking and the left side of Equation 2.62, we notice that Equation 2.61 and Equation 2.64 do not share the same normalization and we find the very useful relation:

$$\omega^2 = \frac{\int_0^L \phi_m(x) \frac{\partial^2}{\partial x^2} \left(EI(x) \frac{\partial^2 \phi_m(x)}{\partial x^2} \right) dx}{\int_0^L \phi_m(x) m(x) \phi_n(x,t) dx}, \tag{2.66}$$

which is a formulation equivalent to Equation 2.5 form mechanical modes, where the wave function is defined as $\Phi_n(x) = \phi_n(x)\sqrt{m(x)}$ and operator $\theta = \frac{d^2x}{dx^2}(EI(x)\frac{d^2x}{dx^2})$. Moreover, it is straight forward to notice that Equation 2.64,

in this framework, is in fact the requirement for hermiticity of the operator θ. So that Equation 2.65 can be rewritten as

$$v(x,t) = \sum_{i=1}^{\infty} A_i \phi_i(x) Y_i(t). \tag{2.67}$$

Where A_i represents the magnitude of the mechanical vibration and is defined as:

$$A_m Y_m(t) = \int_0^L \phi_m(x) m(x) v(x,t) dx. \tag{2.68}$$

Now, we finally want to study the effect of load on Equation 2.46 by substituting Equation 2.67 into it.

$$\sum_{i=1}^{\infty} A_i \left(\frac{\partial^2}{\partial x^2} \left(EI(x) \frac{\partial^2 \phi_i(x)}{\partial x^2} \right) Y_i(t) + \phi_i(x) m(x) \frac{\partial^2 Y(x)}{\partial t^2} \right) = p(x,t). \tag{2.69}$$

Which, can be rearranged via Equation 2.62, Equation 2.68 and projected on the basis formed by $\phi_n(x)$ so that Equation 2.69 leads to

$$\omega_n^2 A_n Y_n(t) + A_n \frac{\partial^2 Y_n(x)}{\partial t^2} = p_n(t). \tag{2.70}$$

Where $p_n(t) = \int_0^L \phi_m(x) p(x,t) dx$ is the generalized load associated with the mode shape $\phi_n(x)$. Equation 2.70 is the familiar differential equation associated to an undamped harmonic oscillator where A_n is a participation factor of the n^{th} mode. Since for realistic systems damping is always present, but it is usually small, we can introduce it phenomenologically so that we obtain:

$$\frac{\partial^2 Y_n(x)}{\partial t^2} + \gamma(x,\omega) \frac{\partial Y_n(x)}{\partial t} + \omega_n^2 Y_n(t) = \frac{p_n(t)}{A_n}, \tag{2.71}$$

where $\gamma(x,\omega)$ is a damping term that depends on the inner (strain) damping and external (viscous) damping and the frequency of the frequency of oscillation.

2.8 Driving forces and mechanical non-linenarities

So far we have paid little attention to load $p(x,t)$ and its effects. While the deformation considered in Chapter 3 and 4 are static, in Chapter 5 we will look

at dynamic loads and they description. In fact, is the load p that starts, damps and/or maintains the oscillation of the nanobeam. In fact, for the purpose of driving the mechanical oscillator, the actual characteristic of the mechanical mode displacement is "nearly irrelevant". Once the load has been properly matched to a given mode or modes, the most relevant characteristics is its time dependence. And harmonically oscillating load can be used to induce *resonant* or *parametric* driving [38]. Resonant driving is described by Equation 2.71. The solution is a characteristic Lorentzian distribution, function of ω^2 and proportional to the amplitude of $p(t)$. So that, at resonance, the amplitude of the oscillation is lager and it diminishes as the frequency of the load moves away from the resonance. Instead, parametric driving is a different effect where the load not only changes in time and along the beam (x), but also along the direction of displacement y, so that Equation 2.71 [39] can be rewritten as:

$$\frac{\partial^2 Y_n(x)}{\partial t^2} + \gamma(x,\omega)\frac{\partial Y_n(x)}{\partial t} + (\omega_n^2 + h(t))Y_n(t) = \frac{p_n(t)}{A_n}. \tag{2.72}$$

Where the load has been written as $h(t)Y(t) + p(t)$. For this kind of load the characteristic response of the system to an harmonic load is much sharper than in the resonant excitation case and, this time, it is centered around $2\omega_n$. Parametric amplification can also lead to an exponential amplification of the resonance for appropriate parameters, although other mechanical non-linearities will have to be added to Equation 2.72 like the Duffing and Van der Pol ones [39] or other effects like the Euler instability [40].

2.9 Summary

In conclusion we have reviewed the basic theory of periodic, photonic, dielectric structures. With specific focus on 1D periodic waveguides and the computation and properties of their field-distribution via eigenmode and FDTD solvers. We have also derived the Maxwell stress tensor formulation of optical forces as well as a surface integral formulation based on perturbation theory. This concepts will mainly be used in a more conceptual rather than analytical form in the next chapter where we will discuss how to predict the field distribution between two parallel waveguides and its immediate consequence on the forces. We discussed methodologies useful to tune the refractive index of dielectric media such as free-carrier injection and the thermo-optic effect which will be of use in Chapter 5. We also looked at the vibrational properties of suspended beams as to give the reader a clear insight over the basic dynamics of solids. All this tools are useful to understand the characteristics of optical forces in photonic system

as well as tailor its behavior. Further studies would require a larger focus on the force matter interaction, in the form of energy transfer between optical and mechanical oscillations as well as the forces induced in metallic media where optical forces are expected to be orders of magnitude larger than in dielectric media. While a general theory has already been developed a couple of decades ago, this concepts are not of common use in the scientific community. Further insight should not only allow a more careful understanding of the mechanical interaction between light and matter, but also open the door to new interesting applications.

Bibliography

[1] R. N. C. Pfeifer, T. A. Nieminen, N. R. Heckenberg, and H. Rubinsztein-Dunlop. Momentum of an electromagnetic wave in dielectric media. *Reviews of Modern Physics*, 79:1197, 2007.

[2] J. P. Penfield and H. A. Haus. Electrodynamics of moving media. Technical report, DTIC Document, 1967.

[3] S. M. Barnett. Resolution of the Abraham-Minkowski Dilemma. *Physical Review Letters*, 104(7):1–4, February 2010.

[4] S. Bobbio. *Electrodynamics of materials*. Academic Press, 1999.

[5] J. D. Jackson. *Classical Electrodynamics*. Wiley, New York, third edition, 1998.

[6] F. Chollet, M. De Labachelerie, and H. Fujita. Compact evanescent optical switch and attenuator with electromechanical actuation. *IEEE Journal of Selected Topics in Quantum Electronics*, 5(1):52–59, 1999.

[7] E. Ollier. Optical mems devices based on moving waveguides. *IEEE Journal of Selected Topics in Quantum Electronics*, 8(1):155–162, 2002.

[8] A. Bruno, G. Lemestreallan, S. Francois, M. Filoche, S. Fouchet, A. Ougazzaden, J. Brandon, N. Bouadma, M.Carre, and A. Carenco. Micro-opt0 mechanical switch integrated. 31(23):2003–2005, 2003.

[9] W. Wegener J. Fischer. Three-dimensional optical laser lithography beyond the diffraction limit. *Laser & Photonics Reviews*, 7(1):22–44, 2013.

[10] A. F. Oskooi, D. Roundy, M. Ibanescu, P. Bermel, J. D. Joannopoulos, and S. G. Johnson. Meep: A flexible free-software package for electromagnetic simulations by the fdtd method. *Computer Physics Communications*, 181(3):687–702, 2010.

[11] Steven G. Johnson and J. D. Joannopoulos. Block-iterative frequency-domain methods for Maxwell's equations in a planewave basis. *Opt. Express*, 8(3):173–190, 2001.

[12] K. Ishizaki, M. Koumura, K. Suzuki, K. Gondaira, and S. Noda. Realization of three-dimensional guiding of photons in photonic crystals. *Nature Photonics*, 2013.

[13] M. Notomi. Manipulating light with strongly modulated photonic crystals. *Reports on progress in physics*, 73(9):096501, 2010.

[14] S. Iezekiel. *Microwave photonics: devices and applications*, volume 3. John Wiley & Sons, 2009.

[15] J. D. Joannopoulos, R. D. Meade, and J. N. Winn. *Photonic Crystals: Molding the Flow of Light*. Princeton Univ. Press, 1995.

[16] M. Eichenfield, J. Chan, R.M. Camacho, K.J. Vahala, and O. Painter. Optomechanical crystals. *Nature*, 462:78–82, 2009.

[17] M. Eichenfield, R. Camacho, J. Chan, K. J. Vahala, and O. Painter. A picogram-and nanometre-scale photonic-crystal optomechanical cavity. *Nature*, 459(7246):550–555, 2009.

[18] M. Li, W.H.P. Pernice, C. Xiong, T. Baehr-Jones, M. Hochberg, and H.X. Tang. Harnessing optical forces in integrated photonic circuits. *Nature*, 456:480–484, 2008.

[19] R. Shankar, R. Shankar, and R. Shankar. *Principles of quantum mechanics*, volume 233. Plenum Press New York, 1994.

[20] T. Baba. Slow light in photonic crystals. *Nature Photonics*, 2(8):465–473, 2008.

[21] J. E. Sipe. Vector k p approach for photonic band structures. *Physical Review E*, 62(4):5672–5677, 2000.

[22] P. Y. Yu and M. Cardona. *Fundamentals of semiconductors: physics and materials properties*. Springer Berlin etc, 1999.

[23] and T. A. Arias S. Ismail-Beigi. New algebraic formulation of density functional calculation. *Computer Physics Communications*, 128:1–45, 2008.

[24] U. S. Inan and R. A. Marshall. *Numerical electromagnetics: the FDTD method*. Cambridge University Press, 2011.

[25] K. Yee. Numerical solution of initial boundary value problems involving maxwell's equations in isotropic media. *Antennas and Propagation, IEEE Transactions on*, 14(3):302–307, 1966.

[26] L. Jia and E. L. Thomas. Optical forces and optical torques on various materials arising from optical lattices in the lorentz-mie regime. *Physical Review B*, 84(12):125128, 2011.

[27] F. N. L. Robinson. Electromagnetic stress and momentum in matter. *Physics Reports*, 16(6):313–354, 1975.

[28] M.L. Povinelli, M. Loncar, M. Ibanescu, E.J. Smythe, S.G. Johnson, F. Capasso, and J.D. Joannopoulos. Evanescent-wave bonding between optical waveguides. *Opt. Lett.*, 30(22):3042–3044, 2005.

[29] S.G. Johnson, M. Ibanescu, M.A. Skorobogatiy, O. Weisberg, and J.D. Joannopoulos. Perturbation theory for maxwell's equations with shifting material boundaries. *Phys. Rev. E*, 65(066611), 2002.

[30] D. E. Aspnes. Local-field effects and effective-medium theory: A microscopic perspective. *American Journal of Physics*, 50:704, 1982.

[31] M I. Gallant and H. M. Van Driel. Infrared reflectivity probing of thermal and spatial properties of laser-generated carriers in germanium. *Physical Review B*, 26(4):2133, 1982.

[32] B. J. Frey, D. B. Leviton, and T. J. Madison. Temperature-dependent refractive index of silicon and germanium. In *Astronomical Telescopes and Instrumentation*, pages 62732J–62732J. International Society for Optics and Photonics, 2006.

[33] and B. Bennett R. Soref. Electrooptical effects in silicon. *Quantum Electronics, IEEE Journal of*, 23(1):123–129, 1987.

[34] P. V. Santons J. De Lima, M. S. Mauricio. Modulation of photonic structures by surface acoustic waves. *Reports on Progress in Physics*, 68(7):1639, 2005.

[35] P. E. Barclay, K. Srinivasan, and O. Painter. Nonlinear response of silicon photonic crystal microresonators excited via an integrated waveguide and fiber taper. *Optics express*, 13(3):801–820, 2005.

[36] A. W. Rodriguezand M. T. H. Reid and S. G. Johnson. Fluctuating-surface-current formulation of radiative heat transfer for arbitrary geometries. *Physical Review B*, 86(22):220302, 2012.

[37] R. W. Clough and J. Penzien. *Dinamics of Structures*. McGraw-Hill, New York, first edition, 1975.

[38] B. K. Donaldson. *Introduction to structural dynamics*. Cambridge University Press, 2006.

[39] R. Lifshitz and M. C. Cross. Nonlinear dynamics of nanomechanical and micromechanical resonators. *Reviews of nonlinear dynamics and complexity*, 1:1–48, 2008.

[40] Davide Bigoni. *Nonlinear Solid Mechanics: Bifurcation Theory and Material Instability*. Cambridge University Press, 2012.

Chapter 3

Ab-initio design of nanophotonic waveguides for tunable, bidirectional optical forces

3.1 Introduction

In this chapter we introduce a semi-empirical methodology to predict and tailor optical forces between two parallel nanophotonic waveguides. Our method is based on the use of symmetries in relation with the variational theorem (Equation 2.5) and the surface formulation of optical forces (Equation 2.35) to find a proper geometry that allows us to change the sign an magnitude of the optical force, in relation to a selected optical eigenmode. At first we develop such methodology by studying the behavior of the electric-field distribution on a cross-section of dielectric waveguides, later we demonstrate that the same method can be adapted to study the field distribution and force of periodically modulated waveguides, where the fields have to be studied over a three dimensional unit cell.

In this chapter, our main goal is to find structures that exhibit forces whose sign is constant as the distance between the waveguides is changed. We are able to do this in both three dimensional structures (periodically modulate waveguides) and two dimensional structures (waveguides with no modulation). While in the second case, as we will see, the proposed geometry is a consequence of the geometrical properties of the system only, in three dimensional systems the slow light effect can be used to manipulate the field distribution

as well as its magnitude. Most importantly, due to the further degree of freedom available in three dimensional structures, we obtain single signed forces using structures that are amenable to fabrication with common lithographic techniques.

In summary, we will first study the characteristics of the optical-force between two parallel dielectric waveguides with constant square cross-section along its axis, induced by the four, symmetry-defined fundamental eigenmodes. The different choices of normalization, power and energy, will be considered. Afterwards we will demonstrate that the sign of the optical forces between parallel waveguides with semi-cylindrical cross-section is constant for all separations. We will use this structure and its eigenmode field-distribution to develop our semi empirical method, formed by five principles applied in three recursive steps, and demonstrate that a similar procedure can be applied to waveguides with square cross section. When we take into account three dimensional structures we discuss the effect of the slow-light band-edge modes on the electric-field distribution and demonstrate that such effect can be used to manipulate the field distribution via a specific choice of the morphology of the waveguides without modification of our methodology. The chapter is closed by discussing a few structures that behave as required. The field-distribution of each structure is discussed and shown to be consistent with the method we proposed.

3.2 Forces between parallel photonic waveguides

As we have previously mentioned in Chapter 1, one of the first examples of optical forces in microphotonic system was given by [1]. In this article Povinelli et al. discusses the optical forces between parallel photonic waveguides induced by localized modal fields propagating along two parallel waveguides with square cross section. They identify two basic operational-modes of such system which are commonly known as bonding as antibonding forces. This is an obvious heritage of basic molecular-bond theory where the wavefunctions of the electron-orbitals are combined in-and out of phase as two atoms come in contact crating new states at higher (antibonding, out of phase orbitals) energy or lower (bonding, in phase orbitals) energy. The former state is unstable, and thus repulsive forces between the two atoms are created, while the latter is stable, creating an attraction between both atoms which forms the molecular-bond. The same concepts can be extended to photonics without so much effort

since most theory behind photonic structures, just as we have described at the beginning of Chapter 2, has been "borrowed" from crystallography [2]. In photonics the linear combination of isolated "atomic" (photonic wise) states is called coupled mode theory and, just like in molecular-bond theory, assumes that a field distribution between two photonic structures, divided by a finite (but not too small) distance, can be expressed as the linear combination of the uncoupled-fields of each waveguide [3]. As an example, we look at two parallel photonic waveguides with square cross-section that are initially separated by $ds = \infty$ (as defined in Figure 3.1). Both waveguides can allow the non lossy propagation of light along its axis and we assume that both are loaded with the fundamental propagative eigenmode supported at a given wavevector k_x. As a straight forward consequence of coupled mode theory, when the separation between both waveguides is slowly reduced, the modes will mix in an out of phase. Coincidentally, just as in molecular-bond theory, in phase mixing induces attractive forces (bonding) while repulsive force are obtained with out-of phase mixing (antibonding). Moreover, given the generic nature of coupled mode theory, we should expect similar behaviors for any structure or mode taken into consideration. However couple mode theory, while elegant and useful is limited to weak couplings, so that, as the waveguides come closer and closer together, it fails to give an appropriate description of the system since the final field distribution is not just a linear combination of the initial, uncoupled fields [4]. In fact, at short separation, that is to say when ds is a fraction of a (as defined in Figure 3.1), the forces are stronger or change sign from repulsive to attractive accordingly to the characteristics of the mode considered. It follows that a general method useful to deduce the magnitude and sign of the forces should be of outmost importance for the development and design of photonic structures that make use of optical forces. Here we chose to develop a heuristic method that should aid the researcher to design structures for optomechanical porpoises with an intelligible intuition on how and why the force behaves in the chosen structure. We prefer this to approximate analytic methods like the one presented in reference [4] which, while precise in its given approximation, it severely limits the design space to very simple geometries.

3.2.1 Forces between squared waveguides

Before proceeding forward we will simply describe the forces between suspended, parallel waveguides with square cross-section of side a, an arbitrary unit length (see section 2.5), shown in Figure 3.1, where we also show the dispersion diagram of the system at a separation $s = 0.25a$. As shown in this figure, the four lowest frequency modes are associated to the four mirror sym-

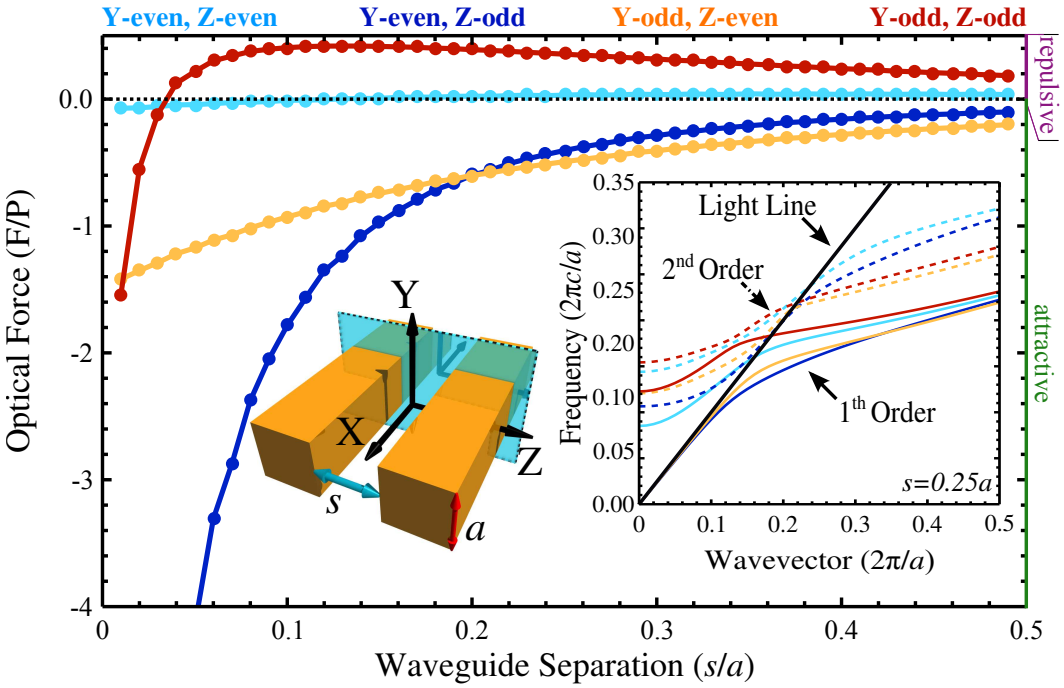

Figure 3.1: Optical forced normalized by input power on the system formed by two parallel waveguides of side a and separation s as a function of the normalized separation s/a. In the inset we show an schematic representation of the waveguides and the coordinate system which is centered symmetrically. The other inset is the dispersion diagram of the same system at a separation $s = 0.25a$. Both the first and second order modes for each symmetry set is shown

metries of the system: y-even/z-even (EE), y-even/z-odd (EO), y-odd/z-even (OE), y-odd/z-odd (OO). The main graphics of Figure 3.1 plots the optical force normalized by input power for each mode. In general we define attractive forces as negative. These represent forces acting of each waveguide, of equal magnitude but opposite direction, that pull both waveguides towards each other, while repulsive forces push both waveguides away from each other. Moreover, because of the y-axis symmetry, we assume that there are no y-axis oriented forces so that the waveguides only move along the z-axis. Always due to symmetry considerations, no net torque is observed in the waveguides either.

As expected via coupled mode theory, approximately for $s > 0.25a$, the specific geometry used has no significant effect on the forces: these are reduced as the separation is increased but the orientation of the forces is constant for each

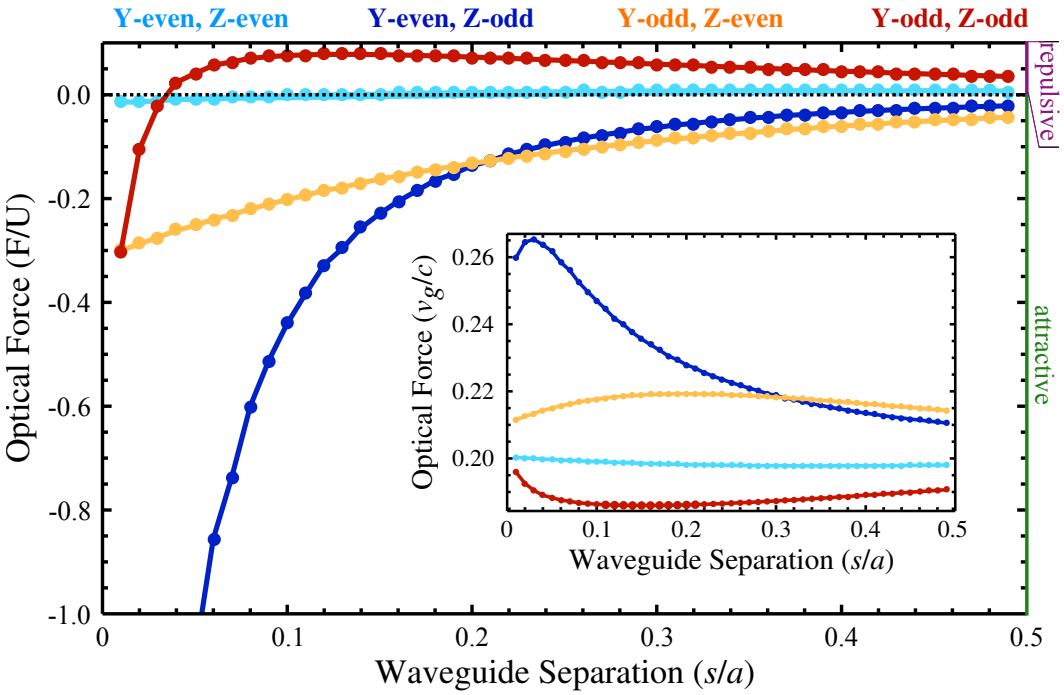

Figure 3.2: Optical force per unit energy as a function of the normalized separation s/a for the same system represented in Figure 3.1. In the inset we show the group velocity as a function of the separation between the waveguides for each mode

mode. The EE and OO modes are repulsive while the EO and OE modes are attractive. In addition, we observe that the repulsive forces induced by the EE mode are roughly an order of magnitude smaller than the force induced by the OO mode. However, when the two waveguides get closer together, roughly for $s < 0.25a$, the forces change considerably. Most noticeable, the forces induced by the EE and OO start saturating to reach a maximum at nearly $s \sim 0.1a$ after what the force varies rapidly until it becomes negative. Also the magnitude of the force associated to the EO mode grows rapidly as the separation is reduced more and more.

In Figure 3.2, we show the force per unit energy, U, instead of input power P, which is the prevalent normalization in literature: here we prefer using the per U normalization which is an index of how efficiently we can use a unit of electromagnetic energy to crate mechanical work. It can be seen that the expected behavior of the force is non-significantly altered by such normalization, except for an obvious change in magnitude, due to the fact that, in this case, the group velocity does not weight the force any longer. In fact, in the case of

per P normalization, the force is proportional to f/v_g, where f is the force per unit energy, so that, in order to correctly predict the forces, we should predict the magnitude of v_g as well. As we have shown in section 2.2.3 it is not easy to guess the magnitude of the group velocity and in both two and three dimensional systems. Fortunately, for the kind of systems considered in this chapter the group velocity is "fairly constant" for all modes and geometries and only changes significantly if slow light band edge modes are considered. So, if the group velocity chances quickly, will the forces change quickly too? The answer is complex and will be made clear in the following sections.

3.2.2 Forces between semi-circular waveguides

Here we only focus on a simple question, is it possible to tailor optical forces? How? In fact, is the behavior shown in Figure 3.2 followed by every possible system. Obviously the possible variables are the dielectric function ε, the absolute size a, the geometry and the wave-vector. From section 2.5 it is

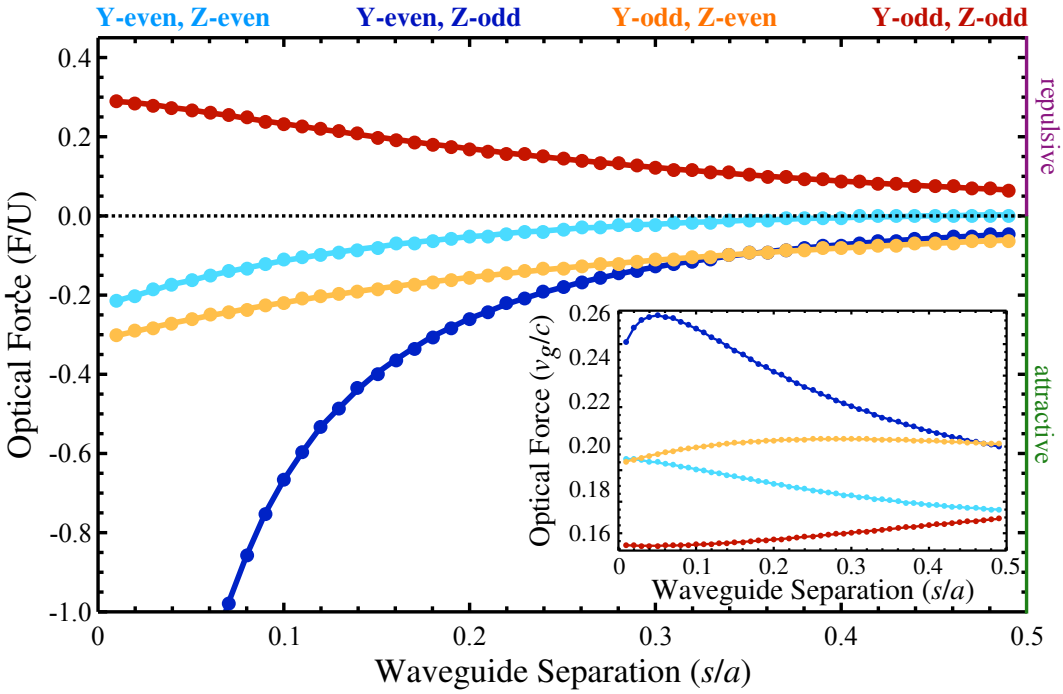

Figure 3.3: Optical force per unit energy as a function of the normalized separation s/a for the same system represented in Figure 3.4(a). In the inset we show the group velocity as a function of the separation between the waveguides for each mode

obvious that, in two dimensional systems, changing a is proportional to a change of k since $\delta k \propto \delta a$ and since $a = \omega^m \lambda = \omega^m 2\pi/k$. Moreover, changing ε should decrease the localization of the fields in the high dielectric media, but there is no reason to expect that it should also change the behavior of the forces as separation between the waveguides is changed. A very good candidate is indeed the geometry. In fact, since according to Equation 2.32 the force depends on the variation of the eigenfrequency, which according to the variational theorem depends on the electric field distribution and since from coupled mode theory we expect that the field distribution depends on the mixing of the fields localized in both waveguides [3], it is reasonable to assume that geometry can be used to gain some degree of control on the characteristics of the fields as the separation between the waveguides is changed. A possible example is given in Figure 3.3, where we use waveguides with semi-circular cross section schematically shown in Figure 3.4(a). The salient features of this structure are the monotonically growing repulsive forces associated to the OO mode and the larger attractive forces associated to the EE mode. We notice from that the magnitude and features of the group velocity are roughly unchanged by the new geometry as shown in insets of Figure 3.1 and Figure 3.3. We attempt and explanation of this behavior with Equation 2.17.

3.3 Intuitive description of the electric field behavior

The electric-field distribution induced by this geometry are shown in Figure 3.4 at a separation of $s = 0.05a$. In this section, plots of the electric-field distribution, share the same normalization or colors and arrow length, except for inevitable small resizing due to the rendering software used and Latex image resizing procedure, however, the proportion to the nominative lengths of the geometries shown in every figure are constant. Before moving forward, it is worth to underline some properties of the electric field due to the geometrical symmetry of the structures we analyze: $\mathbf{E}$ is symmetric respect to mirror transformation about the x-y plane (z-symmetry) and the x-z plane (z-symmetry) and translationally symmetric along the x-axis as shown in Figure 3.4(a). We can now simplify Equation 2.35 from vectorial to scalar form, since its direction is known, by substituting $\mathbf{n}$ with its projection along the z-axis as $(\mathbf{n} \cdot \mathbf{z})$, where $\mathbf{z}$ is the z-axis unit vector. Equation 2.35 shows that the sign of the force depends only on the field distribution along these two waveguide boundaries:

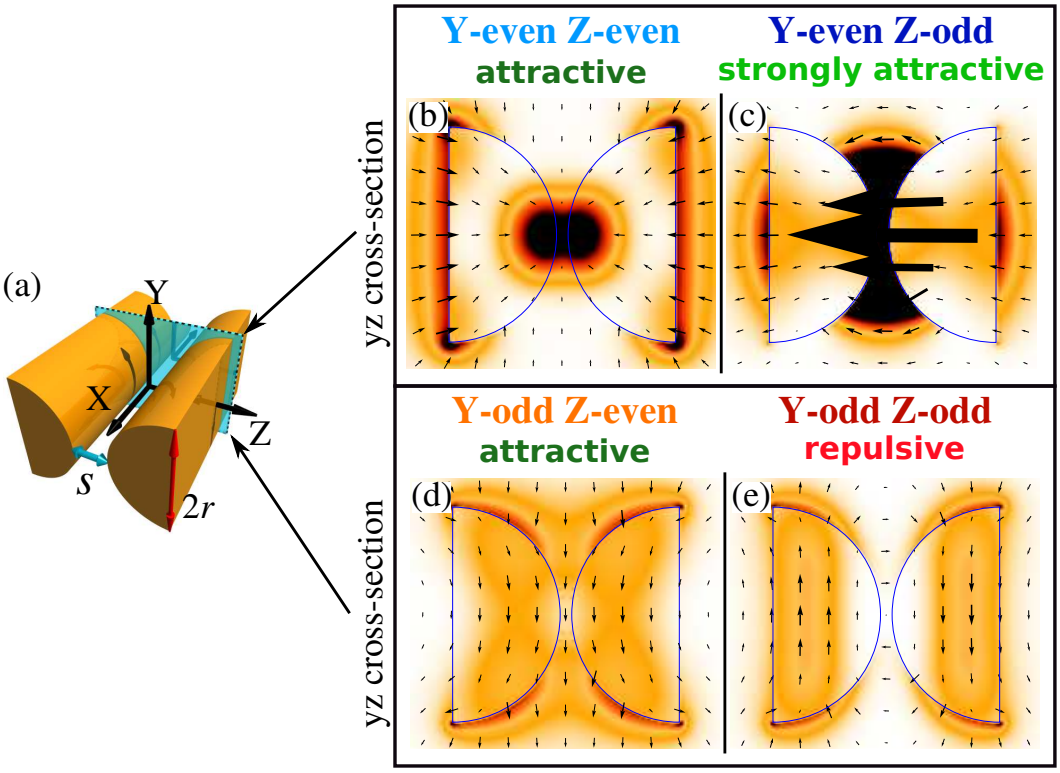

Figure 3.4: **(a)** Schematics of the geometry in use. **from (b) to (e)**: In-plane $\mathbf{E_{yz}}$ vector-field distribution (larger arrows mean more intense) with the total $|E|^2$ in the background (darker is more intense) for the four fundamental modes of parallel waveguides with a semicircle profile ($r = a/2$) at an axial wave-vector of π/a and a fixed distance $s = 0.05a$. All arrows lengths and color scales share the same normalization.

fields localized along the "*inner*" surfaces, along which the dot product $\mathbf{z} \cdot \mathbf{n}$ is negative, will contribute to an *attractive* force, while those along the"*outer*" ones (for which $\mathbf{z} \cdot \mathbf{n} > 0$) will be *repulsive*. In this section we present *five* principles based on the variational theorem,Equation 2.5, and Equation 2.35 that can be used to *infer* and tailor the direction and relative amplitude of optical forces via an educated guess of the field distribution for a given mode and geometry; enabling us to tailor optical forces in 2D and 3D systems. As we have previously mentioned, in order to consistently evaluate the force for different shapes, modes and group velocities, the force is normalized by U, instead of the mode *power*, that would bear a force inversely proportional to the group velocity (v_g) [1, 5]. So that, from the given definition of $\mathbf{E}$ and the

arbitrariness of U (assumed constant and set to unity for all systems), the denominators on both sides of Equation 2.35 can be neglected without loss of generality. We will now postulate the five principles that form the basis of our semi empirical method.

First, we know from the variational theorem, as extensively discussed in literature [6], that a general tendency of the fundamental mode is to concentrate **E** within the waveguides while trying to reduce its spatial variations [5]. It follows two competitive effects: the fields will tend to cross at normal incidence or parallel to the waveguide's surface, and, at the same time, those components of **E** localized in the air regions will tend to have a smaller magnitude compare to components localized inside the waveguides.
Second, when a given set of symmetries is applied, more stringent conditions need to be considered: any symmetry will *repel* those field's components with a node over the mirror plane and *localize* the remaining ones along such plane. An example, in combination with the first principle, is the well-known slot-waveguide (SW) effect [7], which can arise if an odd-symmetry mirror is located between two high dielectric index regions separated by a small gap. This effect can be observed in Figure 3.4(c): the EO mode shows a large confinement of the E_z component (large black arrows) in the narrow, void region separating the waveguides that induces a strong, attractive force.
Third, the chosen symmetries define the relative magnitude of each field component: most of the mode energy will be carried by the component of E with the lesser number of *symmetry-induced* nodes over the unit cell. For example, the OE mode (Figure 3.4(d)) behavior is dominated by E_y since the y-odd and z-even symmetries induce no nodes for that field component. As a result the field is mainly localized between the two waveguides inducing an attractive force. We would like to notice that accidental nodes (usually single points in 2D or lines in 3D) where one or more components have zero magnitudes do not have to be considered.
Fourth, at the same intensity, the force induced by the $E_\perp$ (measured inside the high dielectric index region) is $\varepsilon_1/\varepsilon_2$ times larger than the force induced by $E_\parallel$. The EE mode (Figure 3.4(b)) is attractive due to a marked localization of E_x (third principle) between the waveguides, yet the force is smaller relatively to the EO mode as the attraction is offset by the repulsive contribution of the vertical E_z component along the outer boundary which is enhance by a factor of $\varepsilon_1/\varepsilon_2$ even if the magnitude of E_z (not even visible in Figure 3.4(b)) is much smaller that E_x.
Fifth, according to Equation 2.35, since we are only interested in the component of the force parallel to the z-axis, those regions where the surfaces

are mostly oriented toward the y-axis ($\mathbf{z} \cdot \mathbf{n} \approx 0$) have a reduced contribution to the total force proportional to $\mathbf{z} \cdot \mathbf{n}$ itself. For example the OO mode (Figure 3.4(e)) induces a repulsive force as the fields along the inner surfaces are mainly localized at the very tip of the semicircle, where $\mathbf{z} \cdot \mathbf{n}$ is small, while the fields along outer surfaces fully contribute to the force.

3.4 Predicting the electric field distribution

This principles are at the core of this chapter and represent a "map" of the most common features of the electric fields in relation to the geometry and its final effect on the forces. From our point of view, it should also be enough to allow the reader to predict the field distribution of other two dimensional structures. However we want to facilitate such procedure by also describing how and in which order such principles should be applied. Here we propose the following recursive recipe, ideally formed by three steps which however can be altered according to the readers' commodity.

Step one, we choose a set of symmetries and, with no regard for the shape of the waveguide, we fix the global modal field distribution via the second principle. The main goal is to determine the position of each field component respect to the symmetry planes. We notice that, unless we change the symmetries, no geometry can change such distribution.
Step two, we superimpose the chosen geometry to the fields and, by following the third and first principle, we deduce the field pattern with respect to the waveguide and the relative magnitude of each $\mathbf{E}$ component. In fact, while in step one we consider no interaction between the fields and the waveguide's geometry, via the first principle, if guided modes are considered, it is possible to pin the field distribution to the waveguide geometry. With the third principle, the relative magnitude between the different components of $\mathbf{E}$ is fixed. Once this is done we have to check the fields for consistency with the first principle. For example, if the mode's dominant component were localized in air, according to the third principle other field components that are localized in the high dielectric index region might be enhanced instead. In addition, components that can induce a SW effect are often favored by the first principle, and, as a rule of thumb, we assume that the SW effect always dominates the mode's behavior. In some cases, however, it is possible to suppress such effect by a proper choice of waveguide geometry. In Figure 3.4(e) rounded inner walls were used to increase the spatial variations of the SW effect as we move away from the origin (where SW is suppressed by the y-even symmetry), along the

y-axis. For fairness we would like to mention that, while not necessary, it is useful to have an example where the exact **E**-field is known. This is particularly important when analyzing very different axial-wavevectors (k_x) and materials, since the mode confinement in the high dielectric index regions and the coupling between the two waveguides depends on the relation between the waveguide's cross-sectional area, refractive index and and k_x.
Step three, we apply the fourth and fifth principles and evaluate direction and magnitude of the force. This step is essential to a proper choice of geometry and symmetry. While here, for simplicity, we only treat attractive and repulsive forces, this frame work can be applied to complex mechanical vibrational modes [8], where a large superposition of the mechanical and electromagnetic modes can induce a significant increase in optomechanical coupling.
Finally, if the resulting force does not agree with our requirements, we can either change the symmetries and/or waveguide's geometry in order to eliminate, as we will show later, those regions over which the force is applied, or change the field themselves [5]; repeating the procedure until a proper geometry and symmetries are found.

3.5 Forces and group velocity in 2D systems

In Figure 3.5 we show the field distribution of each of the four modes considered in this chapter at $s = 0.05a$ for waveguides with square cross section. Let's start by taking a look at Figure 3.5(c) where the field distribution associated to the EO mode is shown. In this case, just like in the case of the waveguides with semicircular shape the mode is dominated by a strong slot waveguide effect, as dictated by the third principle. This is in fact and ideal example where E_z component is trapped between to straight and parallel surfaces, although, as can be seen from Figure 3.3 and Figure 3.2 the attractive force induced by the EO mode in this geometry is smaller than the forces induced by the same mode between semicircular waveguides. A possible explanation can be found via the third and first principle: the E_z is promoted by the y-axis symmetry even inside the waveguides where it is favored by the first principle to increase its magnitude. As a result, part of the energy that is taken away from the slot mode, which reduces the attractive force. The characteristic of the OE mode can easily be explained by the third principle since the mode is dominated, just as in the semi-circular waveguides, by the E_y mode. Instead we now observe that the OO mode is attractive rather than repulsive. This is due to the fact that, unlike the semicircular waveguides where the slot waveguide effect was inhibited by its rounded walls in agreement with the first principle, flat

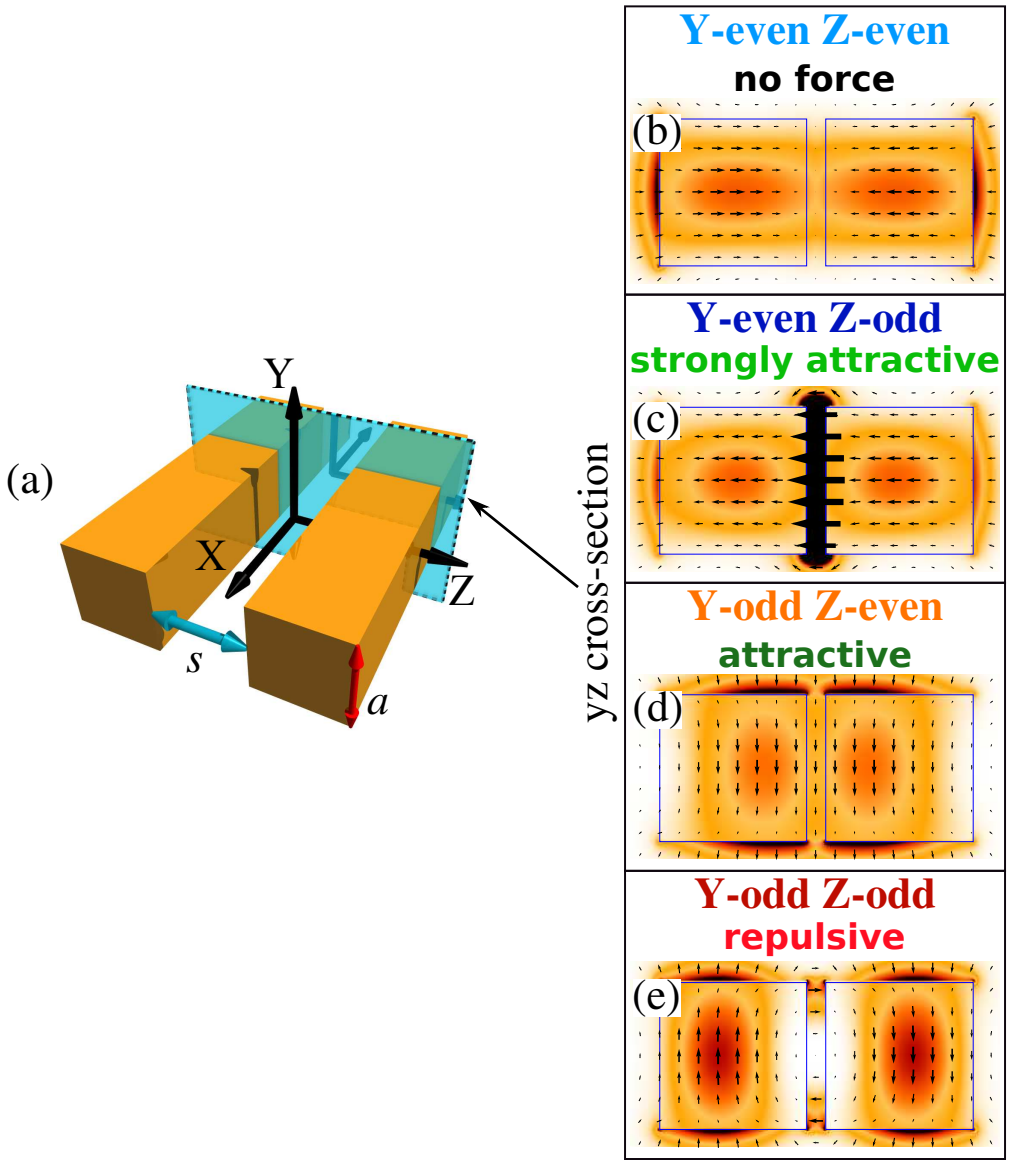

Figure 3.5: **(a)** Schematics of the geometry in use. From **(b)** to **(e)**: In-plane $\mathbf{E_{yz}}$ vector-field distribution (larger arrows mean more intense) with the total $|E|^2$ in the background (darker is more intense) for the four fundamental modes of parallel waveguides with squared cross section of side a at an axial wave-vector of π/a and a fixed distance $s = 0.05a$. All arrows lengths and color scales share the same normalization. The separation shown in (a) is not in scale with the geometry.

surfaces do not inhibit such process any longer inducing an attractive force at short separations between waveguides of rectangular cross section. The EE mode also behaves slightly different from the previous geometry. However, as expected by the very small induced forces, the changes are subtle and not always easy to individuate. In this case the difference is once more due to the first principle. In fact, given the larger area of the waveguide, much like in the case of the EO mode, the mode is dominated both the E_x and E_z component. The first is localized inside the waveguides, which induces a repulsive force due to the z-even symmetry, while the second, which is localized between the waveguides, induces an attractive force. As a result the attractive and repulsive effects are well balance inducing a very weak force.
Now that we have two different systems to compare to, we can also try to apply Equation 2.17 and see if we can describe the dynamics of the group velocity for reducing separations. Unfortunately the information required to the paragraph was shown a couple of pages before ad for brevity, we do not propose it back in this section. Instead of focusing on the differences we focus on the similarities. In the inset of Figure 3.2 and Figure 3.3 we can see that the EO mode is the one with the most common features between both geometries. Since, as we have intuitively demonstrated in section 2.2.3, the value of the group velocity is roughly a function of the localization of the electric field inside or outside the waveguides, the behavior of the EO mode can also be explained by looking at its field distribution. As the two waveguides come closer together more field is expected to be in air due to the growing effect of the slot waveguide mode: inducing a constant grow of the group velocity. However, at short separations, the slot waveguide should saturate the amount of field localized in air; creating the saturation and reduction of the group velocity shown in Figure 3.2 and Figure 3.3. From this description, unlike what shown in the figures, we would expect a change in the group velocity at short separation for almost all modes. While this is mainly the case of Figure 3.2, for the remaining modes, the group velocity changes monotonically with separation in Figure 3.3. If we look at the OO mode we see that the group velocity initially decreases for large separation in both geometries. This can be interpreted as due to the k_x/ω term in Equation 2.17. In this case, the action of the y-axis symmetry, which repels the E_y component, does not significantly changes the localization of the fields inside or outside the waveguides. However, since the forces are positive, a reduction of s implies and increase in eigenfrequency, ω, according to Equation 2.32 so that the group velocity is also reduced. Instead, at short separation, waveguides with squared cross-section shift a large part of their electromagnetic field to the gap between the waveguides due to the slot waveguide effect, increasing the group velocity, while, in

the semicircular waveguides, the group velocity keeps decreasing. We can also see that the for the EE mode in Figure 3.2 that the group velocity is constant for all separations. This is in line with a very small force which implies little change in the distribution of the electric field (according to Equation 2.32 and Equation 2.5) as the separation is changed, which, obviously, implies little change in the group velocity as well. For semicircular waveguides, instead, the group velocity grows. This is mostly due to the larger localization of the E_x component in the air gap between both waveguides. Finally the reduction of the group velocity for a reduction of s can be seen as due to a constantly growing ω, although at a close look we notice that, in Figure 3.2 the group velocity is slightly larger at larger separations, due to a the fields shifting to the air region between the waveguides, before it diminishes at short separations.
In conclusion, from the examples we have just shown, an a posteriori description of the relation between the electric field distribution and the group velocity seems possible, although complicated and clearly not free from interpretation. The complexity of such descriptions is a good example of why using the group velocity to weight the forces might not be an optimum choice.

3.6 Forces between periodic waveguides

We now want to extend our method to periodic, coupled waveguides, where the fields need to be considered over the full 3D unit cell. In this case our method would often (but not always) fail to describe the attractive or repulsive nature of the optical modes, since the field distribution along the propagation axis cannot be described with only two symmetry planes. If a third symmetry plane were to be found, the extension of our method to 3D is straightforward. We do so via slow light modes, that have been previously used to markedly enhance the magnitude of the force [5,9], as the field energy is inversely proportional to v_g (via $U = LP/v_g$) [10]. In fact, at $k_x = \pi/a$ (a is the length of the periodicity) the Bloch plane-wave, envelope function regains the symmetry along the x-axis; so does the Hermitian eigenproblem [11] and, as a consequence, the E-field becomes symmetric as well (if the geometry considered is symmetric along the x-axis). Moreover, for any given mode, once small enough values of v_g have been reached (we observe no important changes for $v_g < 0.15c$, where c is the speed of light in vacuum), further reductions of v_g will not significantly alter such mode's **E**-field *distribution* in the unit cell: in fact v_g is given by $v_g = d\omega/dk_x$ and, as the Brillouin-zone boundary is approached, the eigenfrequency and by extension the eigenmode itself changes less and less (as they are inextricably linked through the variational theorem). This

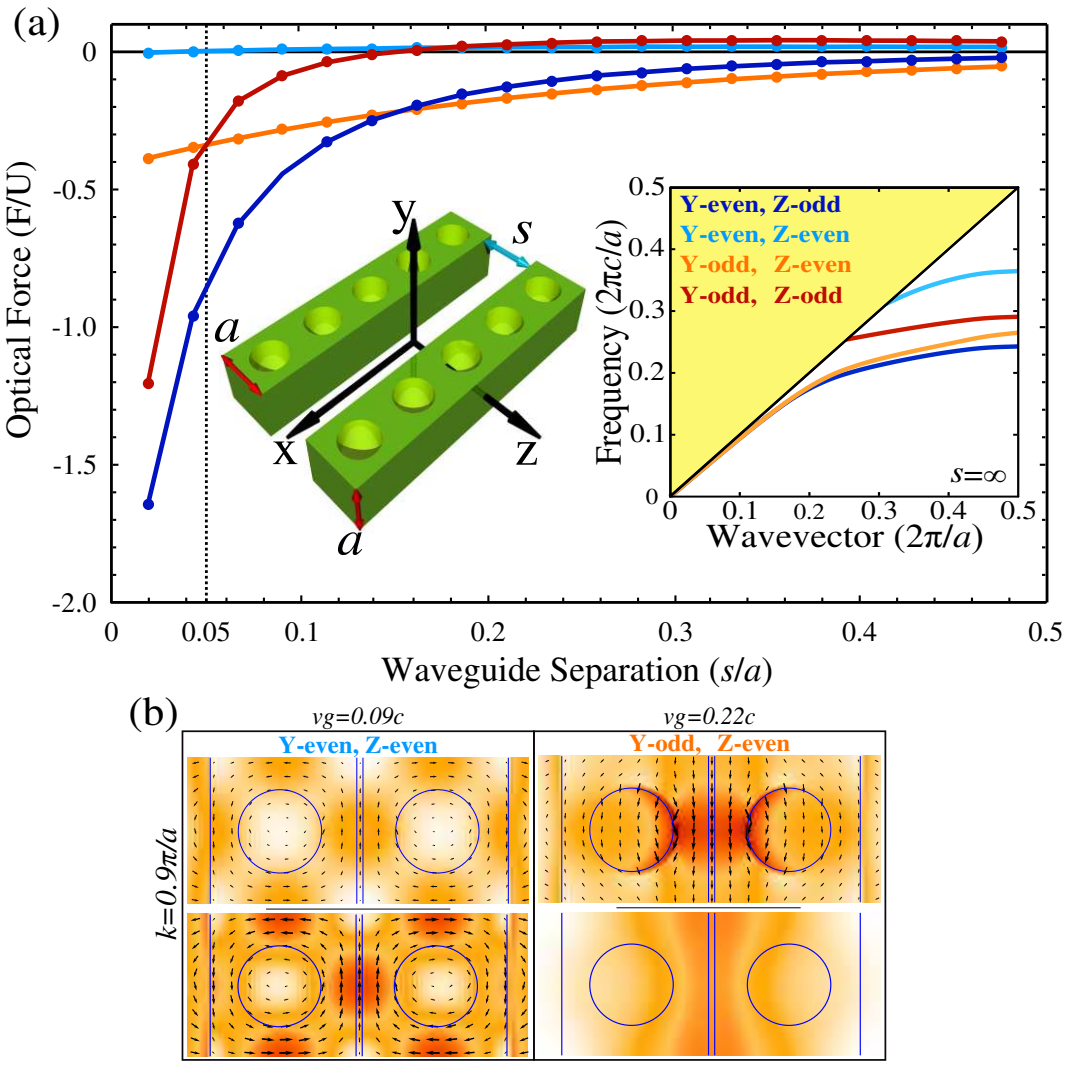

Figure 3.6: Normalized force per unit energy as a function of the waveguide-separation distance s/a for the four fundamental slow-light modes ($k_x = 0.98\pi/a$) of two parallel-waveguides shown in inset (periodicity a, diameter $d = 0.3a$).The inset also shows the dispersion diagram of the four modes studied. (b) Electric field distribution (at the cross-section $y = 0$ and $y = 0.45a$ from the bottom) of the y-even/z-even and y-odd/z-even modes at the wavevector $k_x = 0.9\pi/a$

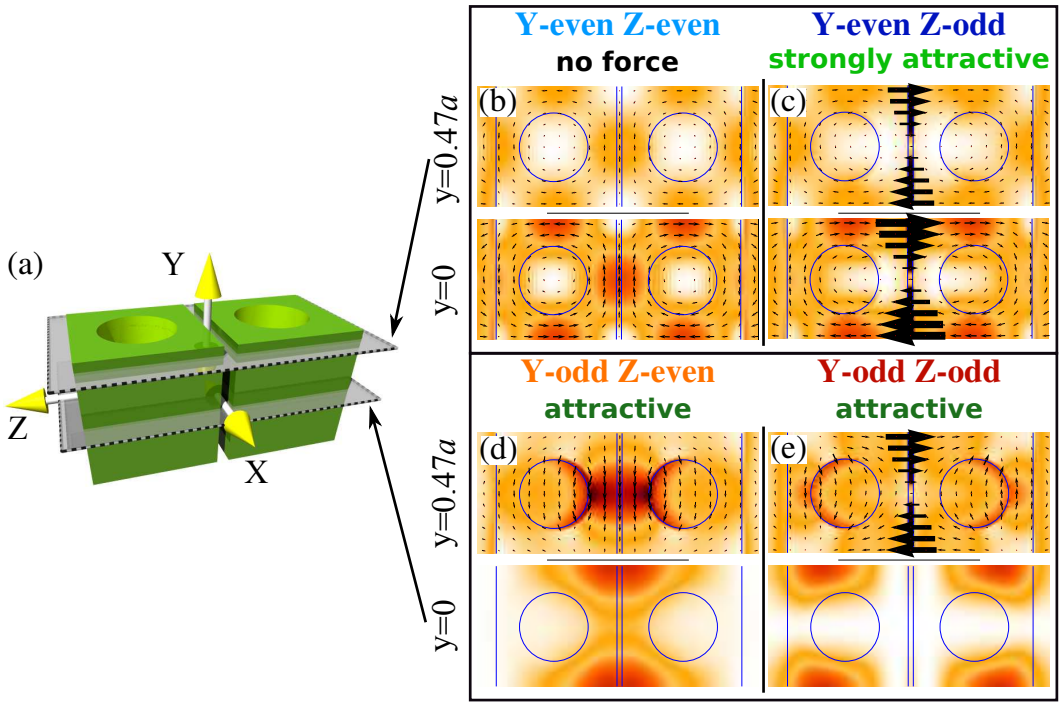

Figure 3.7: **(a)** Waveguide's unit cell. **From (b) to (e)**: In plane $\mathbf{E_{zx}}$ vector-field distribution (larger arrows mean more intense) with the total $|E|^2$ in the background (darker is more intense) for the four fundamental modes of parallel periodic waveguides (periodicity a, radius $0.3a$, separation $s/a = 0.05$) cut along $y = 0$ and $y = 0.47a$ at $k_x = 0.98\pi/a$. Arrows and colors of all figures share the same normalization.

therefore enables us to analyze the field profile of modes slightly offset from the band edge, which can be experimentally probed. As a first example we look at a commonly use 3D periodic waveguide with cylindrical, periodic holes. Forces, fields and schematic of the geometry are shown in Fig. 3.6 and 3.7. We can see from Figure 3.6(b) that the field distribution of the EE mode, at $v_g = 0.09c$, shows no change from $k_x = 0.90\pi/a$ to $k_x = 0.98\pi/a$ ($v_g = 0.02c$, shown in Figure 3.7(b)); while, the OE mode, associated to a larger v_g at $k_x = 0.90\pi/a$ (inset of Figure 3.6(b)), shows visible (even if the general features remain) changes from the corresponding fields at $k_x = 0.98\pi/a$ and $v_g = 0.14c$ (Figure 3.7(d)).

From Figure 3.6 we notice that, for this particular geometry, none of the four modes exhibits strong repulsive forces. Such behavior is fully justified by the geometry in use: in fact, no matter what the parity of the x-mirror symme-

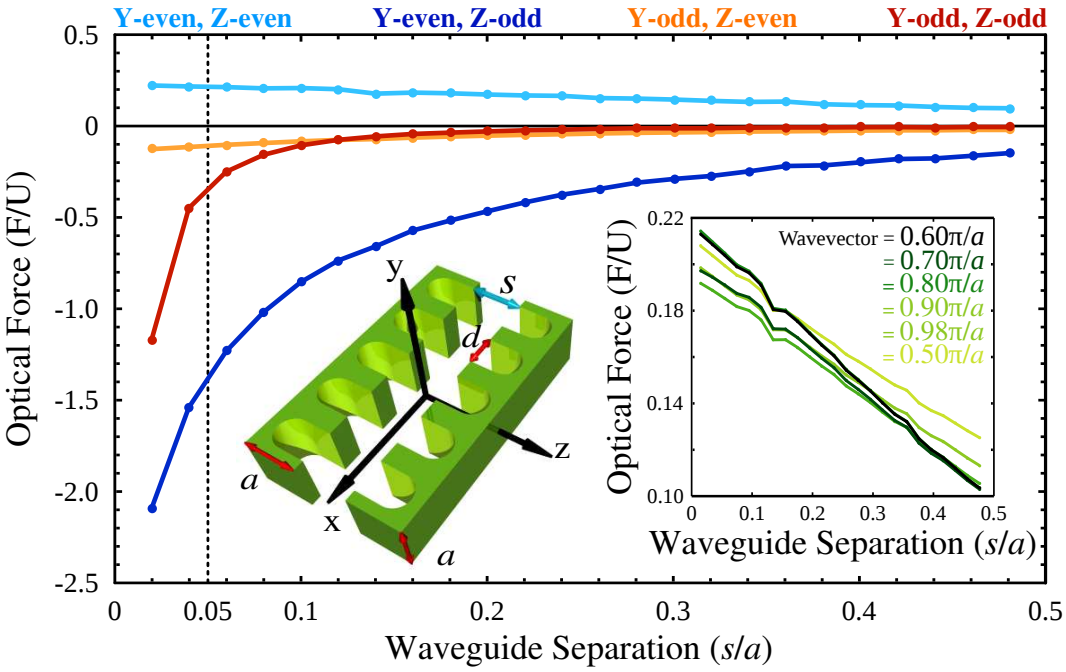

Figure 3.8: Normalized force per unit energy as a function of the waveguide-separation distance s/a for the four fundamental slow-light modes ($k_x = 0.98\pi/a$) of two parallel-waveguides shown in inset (periodicity a, diameter $d = 0.6a$).The inset also shows the normalized force of the y-even/z-even mode for several different wavevectors.

try might be, a fast analysis via the method discussed above will demonstrate that strong repulsive forces cannot appear. In Figure 3.7 we show the field distributions of each eigenmode in the middle and near the top of the unit cell (cross section in the xz-plane), which should be sufficient for revealing its main features as the fields vary continuously. While EO and OE modes behave similarly to their 2D counterparts, the OO and the EE modes deserve a more detailed explanation as both modes can be used to induce strong repulsive forces if a proper geometry is chosen. At short distances the OO mode is attractive due to the presence of a SW effect while is repulsive at large separations where E_y dominates.

The field distribution of the EE mode is a consequence of the band-edge induced x-mirror. With our method we first study EE at large separations. From step one and the first part of step two we notice that E_x is localized along the z-axis, where the low dielectric index air-hole is present, and E_z (repelled by z-even and x-odd while promoter by y-even) is mainly localized inside the

lateral high dielectric index regions. From the last part of step two, we would at first expect E_x to dominate, however from the third principle we would soon realize that, since E_x is mainly localized in air, an enhancement of the magnitude of E_z is expected. Moreover, we also expect E_x to be localized along the small dielectric bridges around the air hole, with a preference for flat surfaces (through which E_x can cross continuously). In conclusion, since the E_x field is well balanced between inner and outer regions, the effect is dominated by the E_z component; inducing a very weak repulsive force (Figure 3.6(a)). However, as the two waveguides come closer together (Figure 3.7(b)), the increasing amount of dielectric at the origin allows E_x to increase its presence at the center of the unit cell, therefore inducing an extremely-weak, attractive force (negligible at $s/a = 0.05$).

3.7 Tailoring optical forces via morphology and slow light

In this section we demonstrate that repulsive optical forces at all separation can be obtained with geometries that are amenable to fabrication. In order to do so, we use the EE mode to ab initio tailor the field distribution of this mode via a proper choice of the geometry of the waveguide. In fact, we notice from step three that the attractive effect of E_x is induced along the dielectric bridges closer to the z-symmetry plane. If we remove them (the new geometry is shown in Figure 3.8(b)), from step two, the EE mode should be dominated by E_x because of the presence of a SW effect and the distribution of E_x over the remaining dielectric bridge should be unchanged. By applying step three to this geometry we notice that, even if most of the energy is localized at the center of the unit cell, where no dielectric walls are present, no attractive force can be induced. As a consequence, the total force over the unit cell is repulsive. Our predictions are confirmed by Figure 3.8 where it can be observed that the EE mode exhibits a monotonically growing repulsive force as the distance between the two waveguides is reduced, while the behavior of the remaining modes is consistent with our model. The EO and OO modes, in fact, exhibits no significant change since the SW effect (E_z), as shown in Figure 3.7, was already pushed toward the edge of the unit cell by the x-odd symmetry, while the magnitude of the attractive force induced by OE mode is reduced roughly by half due to the reduced amount of dielectric at the center of the unit cell as shown in Figure 3.9(d). The EE's attractive force is stronger when the two waveguides are in contact, however we only measure forces up

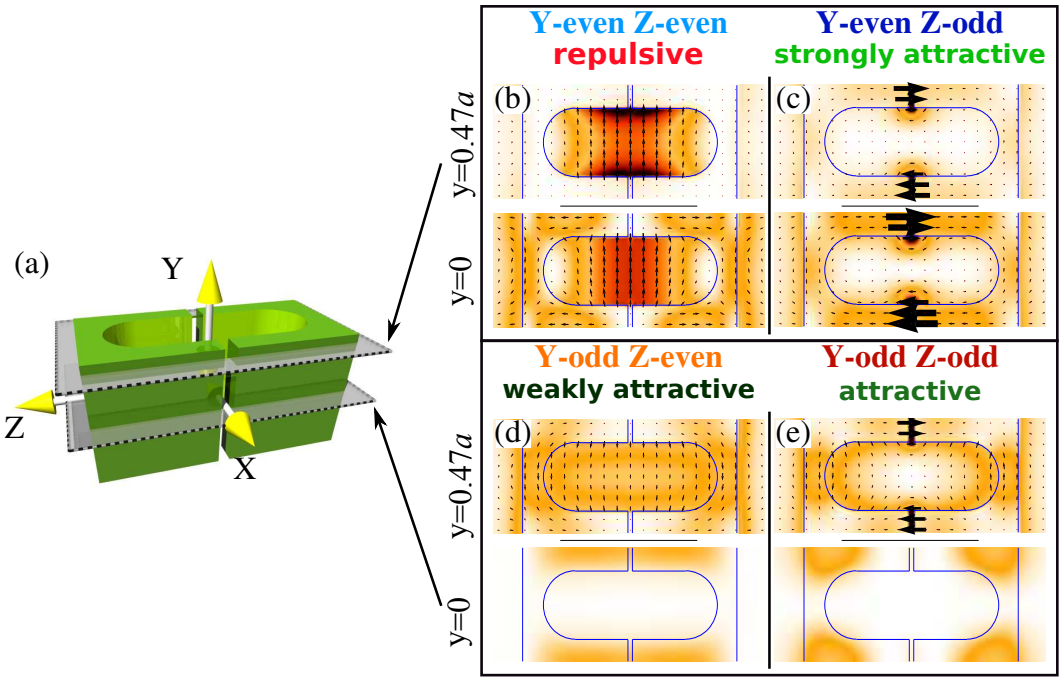

Figure 3.9: **(a)**: Waveguide's unit cell. **From (b) to (e)**: In plane $\mathbf{E_{zx}}$ vector-field distribution (larger arrows mean more intense) with the total $|E|^2$ in the background (darker is more intense) for the four fundamental modes of parallel waveguides (periodicity a, radius $0.3a$, separation $s/a = 0.05$) cut along $y = 0$ and $y = 0.47a$ at $k_x = 0.98\pi/a$. Arrows and colors of all the figures share the same normalization.

to a minimum separation of $s/a = 0.02$ since, at $s = 0$ Equation 2.35 it is not properly defined. At $s/a = 0.02$ the repulsive force induced by the EE mode shown in Figure 3.8 is 5.8 and 17.9 times larger compared to the strongest repulsive forces ($s/a = 0.34$) shown in Figure 3.6, calculated for the OO and EE modes, respectively. As separation is increased, the force of the EE mode in Figure 3.8 gradually decreases but, at $s/a = 0.34$, only a 40% reduction from its peak force is observed. In physical units this is equal to (per unit cell, with $n = 3.45$ at a wavelength $\lambda = 1.55$ μm, assuming a realistic value of $v_g = 0.01c$, an input power of $P = 0.1$ W at $s/a = 0.34$) a repulsive and attractive force of $F = 4.5$ nN (EE mode) and $F = -7.6$ nN (EO mode), respectively. These values are similar to those we previously reported [5], where, for the same parameters, a repulsive and attractive force of $F = 4.8$ nN (OO mode) and $F = -3.9$ nN (OE mode) were observed, albeit with geometries not amenable to fabrication by simple lithographic techniques.

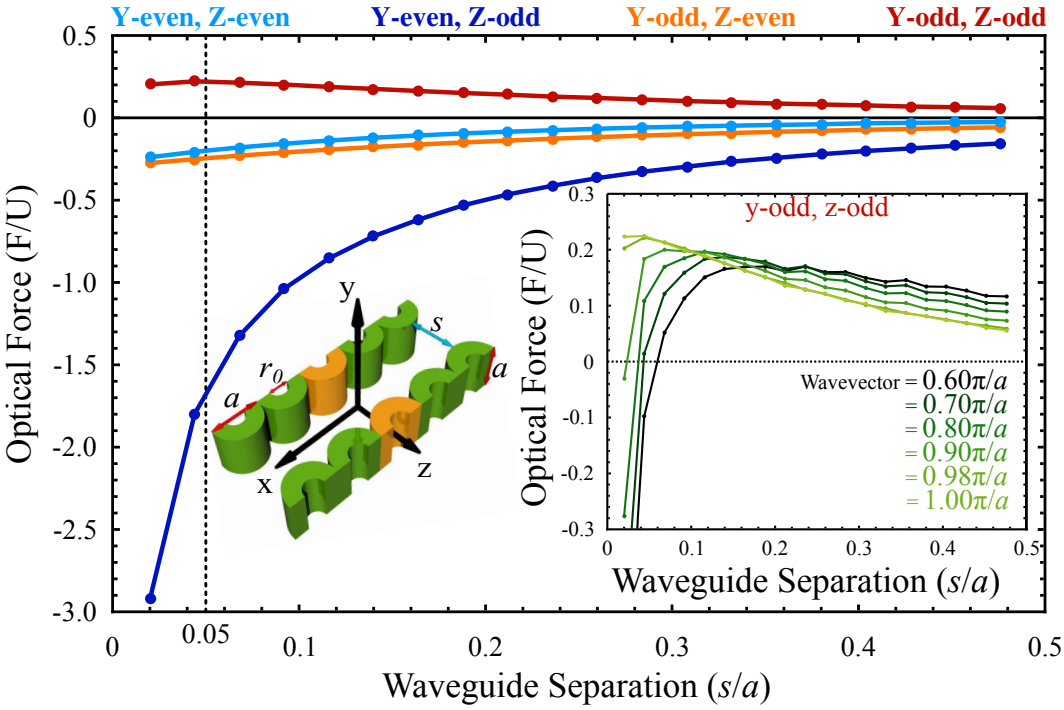

Figure 3.10: **(a)**: Waveguide's unit cell. **From (b) to (e)**: In plane $\mathbf{E_{zx}}$ vector-field distribution (larger arrows mean more intense) with the total $|E|^2$ in the background (darker is more intense) for the four fundamental modes of parallel waveguides (periodicity a, radius $0.3a$, separation $s/a = 0.05$) cut along $y = 0$ and $y = 0.47a$ at $k_x = 0.98\pi/a$. Arrows and colors of all the figures share the same normalization.

A similar procedure can also be applied to the OO mode of our initial structure (Figure 3.6(a)), by following the lesson learned with waveguides of semicircular, transverse cross-section but this time the semicircular structure is on the xz plane as shown in Figure 3.10. Obviously, the same effect could be obtained by adding a periodic perturbation the semicircular waveguides shown in Figure 3.4 as we have already demonstrated in [5]. Although this geometry seems hard to fabricate as it should require the use of stereo-lithographic techniques [12] or aliment of nano-fabricated, tapered, optical-fibers [13]. In the case of Figure 3.10, the constant repulsive force for all separations should appear, either at the first or second order mode, at which time the x-symmetry plane should become odd symmetric, repelling the E_z component, which as we has explained induced the slot waveguide effect and thus the attraction between the waveguides at short separation. Moreover, as we can see from the

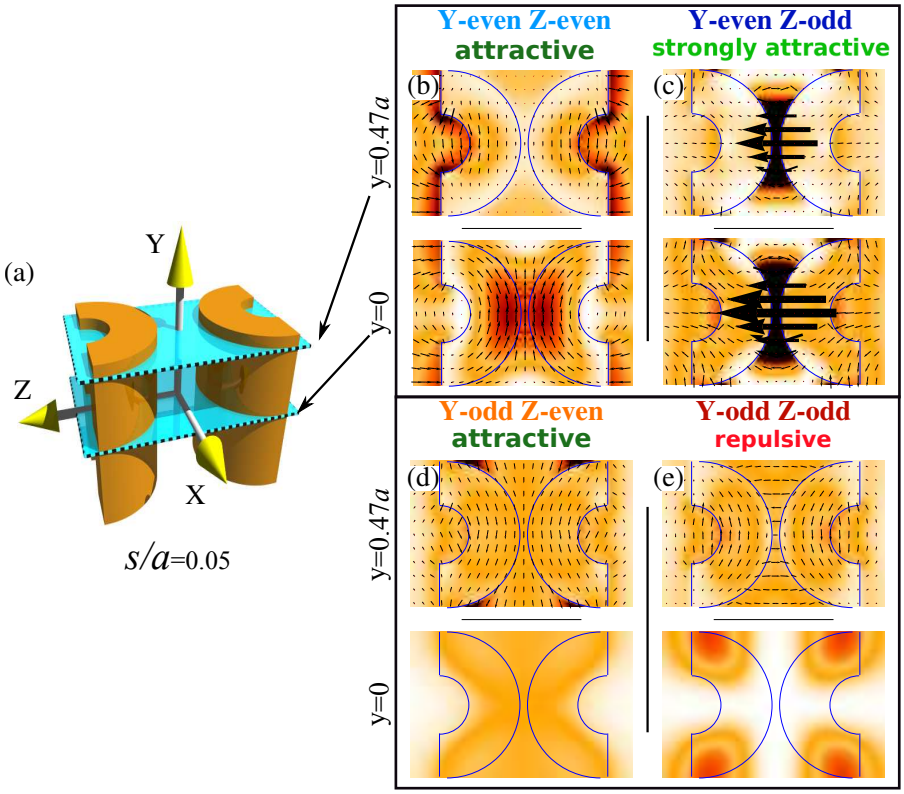

Figure 3.11: **(a)**: Waveguide's unit cell. **From (b) to (e)**: In plane $\mathbf{E_{zx}}$ vector-field distribution (larger arrows mean more intense) with the total $|E|^2$ in the background (darker is more intense) for the four fundamental modes of parallel waveguides (periodicity a, radius $0.3a$, separation $s/a = 0.05$) cut along $y = 0$ and $y = 0.47a$ at $k_x = 0.98\pi/a$. Arrows and colors of all the figures share the same normalization.

inset of Figure 3.10, the effect only appears for values of the wave-vector in proximity to the band-edge and, as the wave-vector is reduced, the behavior the OO mode becomes more and more "attractive" at short separations. In Figure 3.11 we show the field distribution for the four fundamental symmetric modes at an axis wave-vector, $k_x = 0.98\pi/a$, and the xz cross-sections at $y = 0$ and $y = 0.47a$. This semi-cylindrical structure, although an uncommon structure, is still well suited to fabrication via 2D lithography. In fact, in order to add realism, the semi-cylinders are connected by a thin layer. Finally the hole that makes our structure look much like a half of a 5-Yen coin, helps increasing the magnitude of the attractive force at short separation.

3.8 Summary

In summary, by following the same principles here discussed we have found structures that, while always feasible to conventional fabrication processes, exhibit strong repulsive forces by, for example, suppressing the SW effect commonly associated with the OO mode. Moreover, in 3D systems, the same method can be easily extended to the four, fundamental modes (given by x-odd) or to the analysis of other resonant structures. In conclusion we have demonstrated and described a methodology to ab-initio tailor optical forces between nanophotonic waveguides via careful design of the waveguide morphology through specific symmetry constrains and, when periodicity is introduced, via band-edge modes. As a result the geometries considered exhibit strong repulsive and attractive forces while being amenable to fabrication via standard lithography techniques. While this method is no substitute of rigorous eigenmode calculations, it avoids blind optimization of the waveguide geometry and should help find geometries and tools to develop novel optomechanical applications.

Bibliography

[1] M.L. Povinelli, M. Loncar, M. Ibanescu, E.J. Smythe, S.G. Johnson, F. Capasso, and J.D. Joannopoulos. Evanescent-wave bonding between optical waveguides. *Opt. Lett.*, 30(22):3042–3044, 2005.

[2] K. Sakoda. *Optical properties of photonic crystals*, volume 80. Springer, 2005.

[3] S. L. Chuang. *Physics of photonic devices*, volume 80. John Wiley & Sons, 2012.

[4] W. H. P. Pernice, M. Li, and H. X. Tang. Theoretical investigation of the transverse optical force between a silicon nanowire waveguide and a substrate. *Optics express*, 17(3):1806–1816, 2009.

[5] A. Oskooi, P.A. Favuzzi, Y. Kawakami, and S. Noda. Tailoring repulsive optical forces in nanophotonic waveguides. *Opt. Lett.*, 36:4638–4640, 2011.

[6] Steven G. Johnson and J. D. Joannopoulos. Block-iterative frequency-domain methods for Maxwell's equations in a planewave basis. *Opt. Express*, 8(3):173–190, 2001.

[7] V.R. Almeida, Q. Xu, C.A. Barrios, and M. Lipson. Guiding and confining light in void nanostructure. *Opt. Lett.*, 29:1209–1211, 2004.

[8] E. Gavartin, R. Braive, I. Sagnes, O. Arcizet, A. Beveratos, T. J. Kippenberg, and I. Robert-Philip. Optomechanical coupling in a two-dimensional photonic crystal defect cavity. *Phys. Rev. Lett.*, 106:203902, May 2011.

[9] J. Ma and M.L. Povinelli. Effect of periodicity on optical forces between a one-dimensional periodic photonic-crystal waveguide and an underlying substrate. *Appl. Phys. Lett.*, 97(151102), 2010.

[10] J. D. Joannopoulos, R. D. Meade, and J. N. Winn. *Photonic Crystals: Molding the Flow of Light*. Princeton Univ. Press, 1995.

[11] M. Tinkham. *Group theory and Quantum Meachanics*. Dover, second edition, 1992.

[12] S. Kirihara. Fabrication of photonic crystals by stereolithography technique. In *Progress in Advanced Structural and Functional Materials Design*, pages 195–211. Springer, 2013.

[13] T. S. Francis, S. Yin, and P. B. Ruffin. *Fiber optic sensors*. CRC press, 2010.

Chapter 4

In plane manipulation of a dielectric nanobeam with gradient optical forces

4.1 Introduction

While in the previous chapter we demonstrated how optical forces can be made repulsive even at very short separation, there are many other possibilities left to explore. For example, can the methodology proposed in the previous chapter be applied to non-axis symmetric systems? In fact, even if very few studies have taken into consideration non-axis symmetric geometries, these might yield useful properties and effects, like single-mode trapping. Moreover there is no real reason why we should only consider one dimensional forces (that is to say attractive or repulsive) acting on the plane where both waveguides lay but, intuitively, optical forces should exist also for displacements of the beam off such plane. As a matter of fact, while multi-mode trapping has already been demonstrated [1] it has significant limitations: first of all when more than one mode is considered the force along the waveguide will not be constant but, due to their non-identical group velocity, the modes will interfere inducing a time harmonic variation of the force; second the location of the potential it is hard to control, due to the characteristic dependence of the force on the separation between the waveguides.

In this chapter we do not only show that gradient forces can be used to induce trapping but also other effects such as levitation (a displacement along the y-axis as shown in Figure 4.1) and, in general, to actively control the position of a dielectric waveguide on the whole plane transverse to the direction

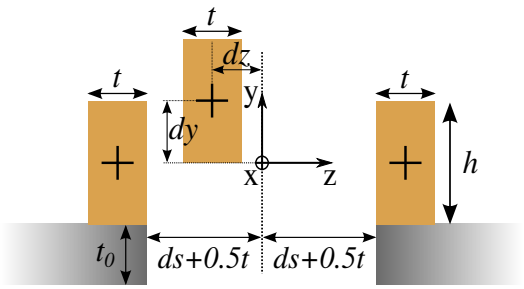

Figure 4.1: Schematic of the system studied in which only the central waveguide is free to move. The height and thickness of the waveguides is $h = a$ and $t = 0.5a$. The thickness of the thin SiO_2 layers is $t_0 = 0.5a$. The waveguides are made of Silicon and the separation between the external beams is fixed to $2ds + t$, where $ds = 0.25a$.

of propagation of light. To do so, we propose a system formed by three interacting modes (waveguides) rather than just two, where the two external waveguides are fixed to a substrate and only the central one is free to move, described in Figure 4.1. The force on the central beam (CB) can now be tailored by an appropriate choice of the cross sectional geometry of the waveguides, which can be done via the method developed in Chapter 3. Moreover, in order to guaranty predictability and intense forces among a large number of geometries and modes, we focus on the five *lowest*-energy, propagative eigenmodes. In fact, as discussed in chapter 2, according to the variational theorem, the eigenmode-field distribution should become more complex (more geometry sensitive) and less localized as the mode-frequency increases, inducing smaller forces with less predictable behaviors.

In order, we will first recall and summarize the procedure developed in Chapter 3. We will then apply it to a simple system formed by two parallel waveguides of rectangular cross-section, at a fixed separation along the $z - axis$, that are shifted along the y-axis, which gives as example of a system where forces are coupled along the axis. Then we investigate the behavior of the force induced on the CB in the 3WC by the modes considered; although the fifth mode in order of energy is considered separately, due to its distinctive properties. A short comparison with the two parallel waveguides system, studied in the previous chapter, is also carried out. Finally we quickly consider a simple method useful to tailor the position of the forces along the y and z axis independently via simple modifications of the cross-sectional shape of the waveguides.

4.2 Surface formulation of Gradient-Forces

Our discussion is once more based on Equation 2.35. In this chapter forces are defined positive if oriented toward positive directions of the coordinate system, shown in Figure 4.1, and vice versa. Hence, since Equation 2.35 depends exclusively on the field distribution **E**, just like we have done before, if we could predict the electric field distribution, we should be able to make and educated guess of the magnitude and direction of the force as well, even if in most cases the system considered will only have one plane of symmetry. Here we summarize the set of principles, described in the previous chapter.
First, the fields tend to be strongly localized, preferably in the high refractive index regions, and to have the least amount of spatial variations.
Second, those field components that have a node along any symmetry plane will be pushed away from it, and vice versa.
Third, the field component with the least number of nodes along the symmetries will dominate the direction and magnitude of the force.
Fourth, components of the field that are normal to the interface ($E_\perp$, measured inside the high dielectric index region) have a larger contribution to the force, proportional to $\varepsilon_1/\varepsilon_2$, respect to $E_\parallel$.

4.3 Optical forces in non-symmetric systems

In order gain a better understanding about the relation between symmetry breakage and its effect on the electromagnetic modes, in Figure 4.2 we use we plot the symmetries of the rigid-translations, according to the geometry of the waveguide. As we can see there are at least two ways of breaking the symmetry: the first is to change the geometry of the waveguide, the second is to translate on of the waveguides off its planes of symmetry. However, what kind of translation breaks the symmetry and how depend on the geometry of the waveguides. In fact, for cylindrical waveguides we see in Figure 4.2 that, no matter the translation the system is always axis symmetric. Instead, if we use rectangular waveguides, the entire geometry can be divided in four slices which are identical for mirror symmetries along the dashed lines. Of course, while keeping track of the force for different modes is easy in theory, in practice, as we will show in Chapter 3. However, since for now our objective is to map the optomechanical interaction for different deformation, we find such analysis quite useful. The lesson we learn is that, as long as the two waveguides lay on some plane of symmetry, shown in the gray thin line in Figure 4.2, the forces can be reduced to attraction/repulsion between the waveguides along

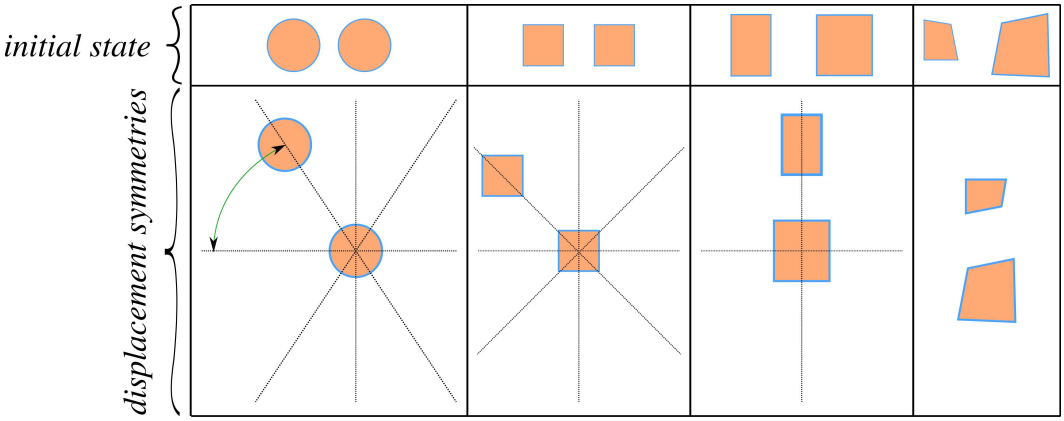

Figure 4.2: Symmetries of rigid translations according to the geometry of the waveguides

such planes.

4.3.1 y-direction displacements

When the waveguides are not located on such planes forces along both the y and z axis appear contemporarily and the system can not be reduced to the attractive/repulsive behavior. An example is given in Figure 4.3 where we plot the forces between two parallel waveguides and one of the waveguides is moved along the y-axis while the separation dz is keep constant at $dz = 0.25a$. In this case, just as expected, forces along both axis appear. It is interesting to notice that there seem to be a certain correlation between the sign of the F_y and F_z force: repulsive forces along the z-axis induce unstable equilibrium forces along the y-axis while attractive force along the z-axis induce and stable equilibrium forces along the y-axis.

4.4 Gradient-Forces between three parallel identical waveguides

The system is shown in Figure 4.1 is formed by three identical waveguides with a thickness of $t = 0.5a$ and height of $h = a$; when the CB is at the origin, $\{dz, dy\} = \{0, 0\}$, the beams are evenly spaced along the z-axis with an initial separation of $ds = 0.25a$ and they all lay on the xy-plane. For now we assume that the *thin* SiO_2 ($n = 1.5$) layer, used to fix the two external waveguides, does not significantly influence the field distribution of the modes we study due

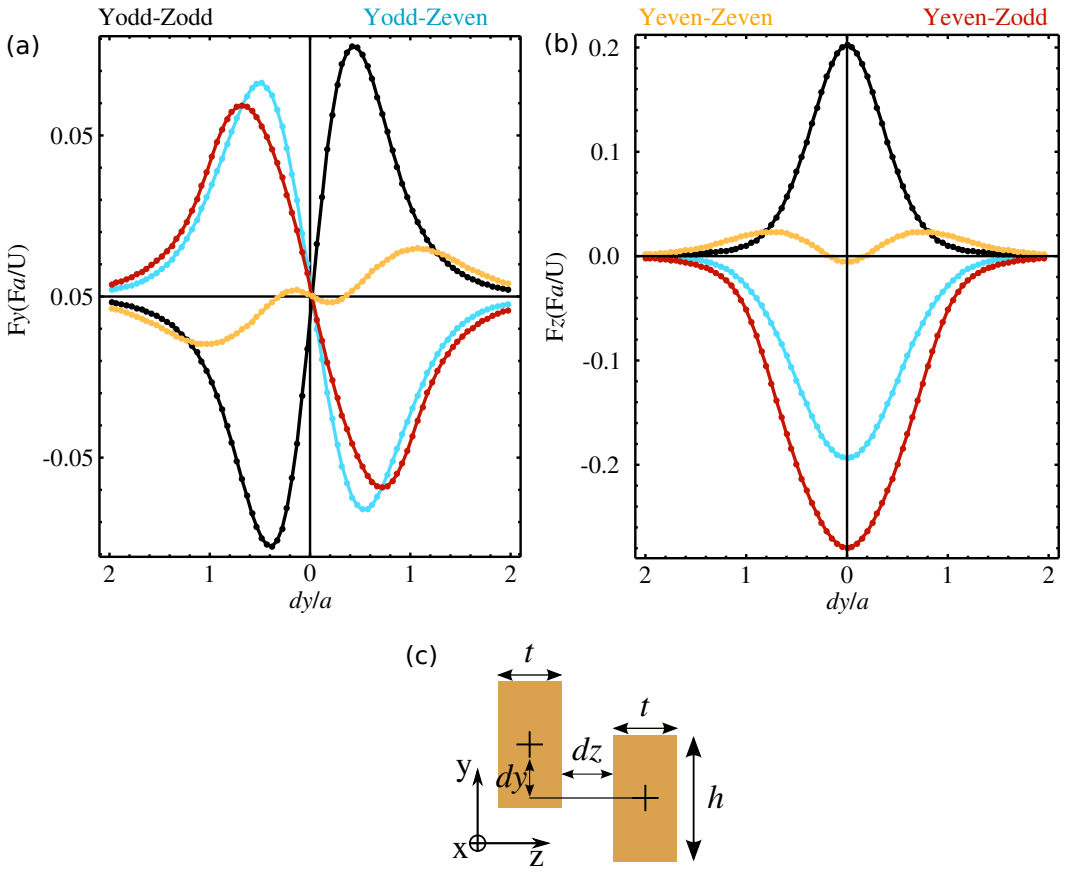

Figure 4.3: **(a)** y-Axis directed force per unit energy as a function of a displacement dy/a for the four fundamental symmetry modes at $k = \pi/a$. **(b)** y-Axis directed force per unit energy as a function of dy/a at the same dz. **(c)** Schematic of the geometry in use where a the normalized unit length $h = a$ and $t = 0.5a$ respectively.

to the very large index contrast between such layer and the Silicon waveguides ($n = 3.45$) so that our system is z-axis symmetric; a more rigorous justification will be given when displacements along the y-axis are considered.

The dispersion diagram of the 3WC at $\{dz, dy\} = \{0, 0\}$ is shown in Figure 4.4(b), where each mode is labeled after its parity [2]. We notice that a different choice of k_x will change the order of the modes as a function of frequency. However, this choice should not significantly affect the characteristic field distribution and forces of each mode since these are mainly defined by the symmetry of each mode and by the shape of the waveguides rather than by the mode's frequency or wavevector. When the forces are measured, all

modes are computed at a constant axial wave-vector, $k_x = \pi/a$. This value is chosen arbitrarily: just large enough to guarantee that all the five modes considered are non-radiative. At $k_x = \pi/a$ and when the CB is at the origin of the coordinate system the four lowest-energy modes correspond to the following mirror-symmetries: y-even/z-odd (EO), y-odd/z-odd (OO) and two y-odd/z-even (OE) modes, namely OE(1) and OE(2). We notice that these modes do not match the four distinct sets of mirror-symmetries of the system since the y-even/z-even (EE) mode, whose characteristics will be considered separately, lays at higher frequency as shown in Figure 4.4(b).

In the 3WC we identify three remarkable features of the optical forces: ***trapping***, ***pulling*** and ***levitating***. *Trapping-forces* oppose displacements of the CB away from the point of equilibrium, where the forces are 0. These forces can be directed either along one (one dimensional trapping) or both axis (two dimensional trapping). *Pulling-forces* are directed along the z-axis and towards one of the external waveguides, which is analogue to attractive forces in the two waveguides configuration (2WC). *Levitating-forces* are oriented along the y-axis such as to pull the beam away from both the point of equilibrium and the external beams.

4.4.1 z-axis oriented forces

Let's first consider the case in which the CB is free to move along the z-axis, as shown in Figure 4.4(a). In Figure 4.5 we also show $|\mathbf{E}|^2$ and E_{yz} for each mode at $\{dz, dy\} = \{0, 0\}$ and $\{dz, dy\} = \{0.075a, 0\}$ respectively. All pictures share the same normalization of arrows length and color scale: darker colors and longer arrows indicate stronger fields.

OE(1) mode

We first consider the OE(1) mode shown in Figure 4.5, which induces a pulling force, as shown in Figure 4.4(a). We can use such mode to describe the characteristics of the first three principles described in Section 2, which are the most used ones throughout this paper. At the beginning we find the dominant component of the mode via the third principle, which in this case is E_y as a result of the y-odd/z-even symmetry. This means that it is not necessary to consider other components in order to get an idea of the magnitude and direction of the optical force since most of the mode's energy, U, will be carried by this component. Next we need to roughly guess the spatial distribution of E_y in relation to the waveguides. By using the second principle we expect E_y to be localized long the axis of symmetry since it is continuous along both of them as can be seen from Figure 4.5. Finally we need to find the phase of E_y

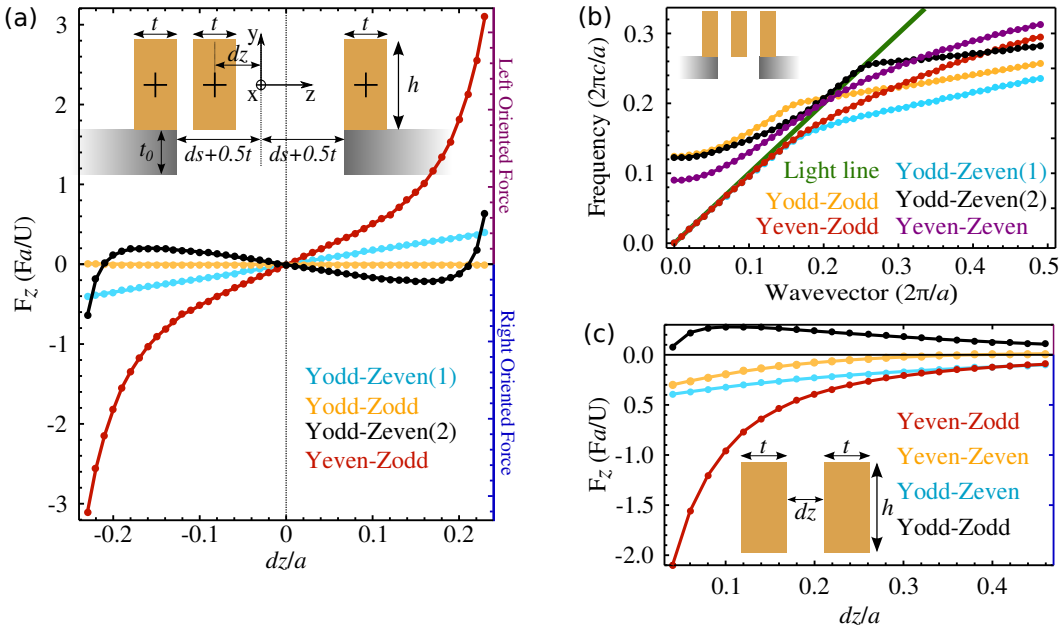

Figure 4.4: **(a)** Force per unit energy as a function of a displacement dz/a for the Yodd-Zeven(1), Yodd-Zodd, Yodd-Zeven(2) and Yeven-Zodd modes at a constant axial wave-vector $k_x = \pi/a$. In the inset we show a schematic of the geometry in use where a is the unit length, t_0 is the thickness of the SiO_2 support layer equal to $0.5a$ and the height and thickness of the waveguides is $h = a$ and $t = 0.5a$ respectively. **(b)** This figure shows the dispersion diagram for the five lowest frequency modes of the same geometry shown in (a) when all waveguides are evenly spaced. The field distribution of these modes at $k_x = \pi/a$ are shown in the first row of Figure 4.5 and in Figure 4.8(b). **(c)** Force per unit energy as a function of the displacement dz/a for the Yodd-Zeven, Yeven-Zodd, Yodd-Zodd and Yeven-Zeven fundamental modes at a constant axial wave-vector $k_x = \pi/a$ between two parallel waveguides with identical parameters to those shown in (a).

between the CB and the external waveguides. Since OE(1) is the fundamental mode of the y-odd/z-even symmetry-set we can expect E_y to be in phase between all waveguides since this minimizes the spatial variations while localizing most of the fields in the high index media, as dictated by the first principle. Unfortunately, for $\{dz, dy\} \neq \{0, 0\}$, our principles are not as useful. However we can still extrapolate their distribution from the known field-distribution at $\{dz, dy\} = \{0, 0\}$. We do so, via the first principle, by finding a new distribution that maintains the salient characteristics of each mode while mainly

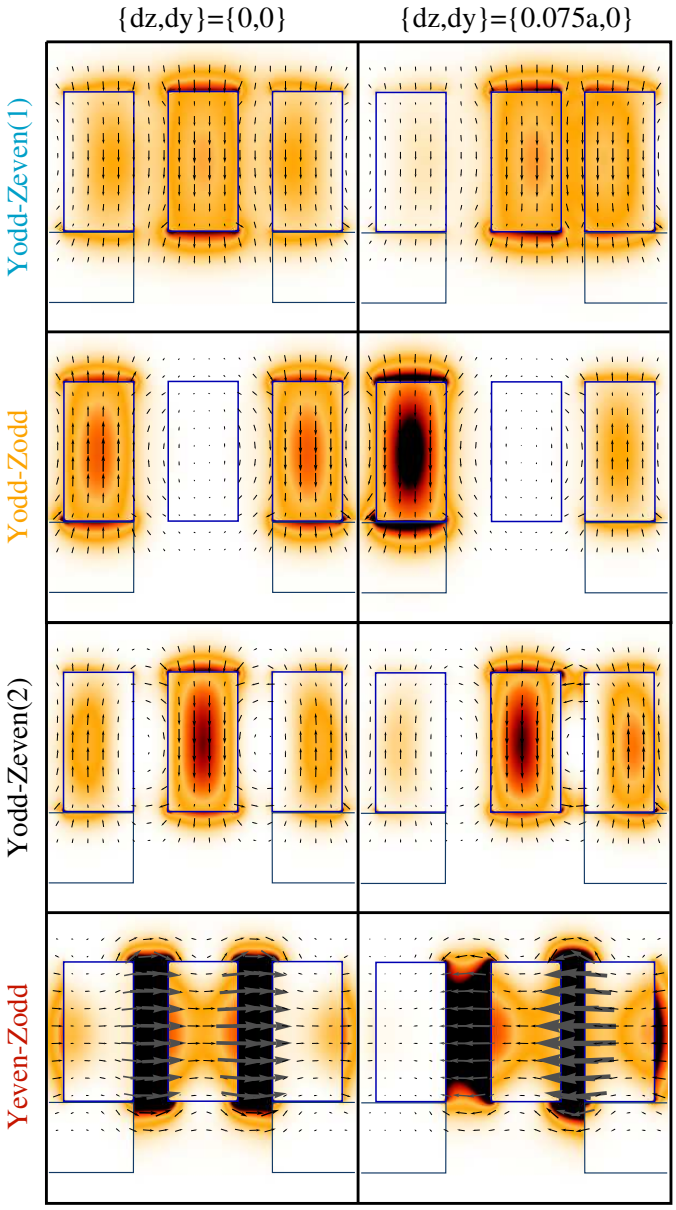

Figure 4.5: In-plane $\mathbf{E_{yz}}$ vector-field distribution (larger arrows mean more intense) with the total $|E|^2$ in the background (darker is more intense) for the Yodd-Zeven(1), Yodd-Zodd, Yodd-Zeven(2) and Yeven-Zodd modes at $k_x = \pi/a$. For the first row $dz = 0$ and for the second row $dz = 0.075a$. No displacement along the y-axis ($dy = 0$) is considered. All arrows lengths and color scales share the same normalization.

minimizing the spatial variations. In this case, for example, since E_y is in phase between all waveguides, if the CB gets closer to the right most beam, the center of field distribution in the CB will shift to the right too in order to satisfy the first principle. This increases the localization of the fields in the high index media without substantially increasing the spatial field-variations because E_y was originally in phase between all three waveguides. Altogether we observe a pulling force due to the increasing magnitude of the field between the two closer waveguides.

OO mode
Instead the OO mode induces a trapping-force. However this force is tiny: the maximum value of the dimensionless force is $F_z = \pm 0.001$ at $dz = \mp 01a$. This is due to the z-odd symmetry which forces E_y, the dominant component, outside the CB. As a result of a negligible magnitude of the fields on the central waveguide, as shown in Figure 4.5, a negligible force is formed.

OE(2) mode
The OE(2) mode is the second mode in order of energy associated to the OE symmetry set and, not surprisingly, characterized by E_y out of phase between the CB and the external waveguides as shown in Figure 4.5. As a result, for example, as the CB moves closer to the right most waveguide, the fields in the CB will shift to the left to avoid the fast spatial variations at the right wall (first principle), therefore increasing the amplitude of the fields on the left most wall of the CB, inducing a *one-dimensional trapping-force* along the z-axis. This effect is also shown in Figure 4.4(a) where, for positive values of dz the forces are negative and vice versa. On a section of the waveguide of length a the magnitude of the trapping force is in line with previous reports [3]: for a 0.1 W input power, at $dz = 0.15a$, the maximum magnitude of the force is ~ 0.4 nN; measured as insection 2.5. The group velocity of each mode has also been taken into account when the absolute force per input power is computed, though, for waveguides with constant cross-section, it is fairly constant through all modes.

EO mode
Finally, the EO mode induces large pulling forces, as shown in Figure 4.4(a). This mode is dominated by the E_z component (third principle) as can be seen in Figure 4.5, which results in the formation of a slot-mode between parallel surfaces (first principle) and detailed described in the previous chapter. However, E_z does not need to quickly decay inside the CB to ensure localization as it happens on the external beams, in accordance to the first principle. Most

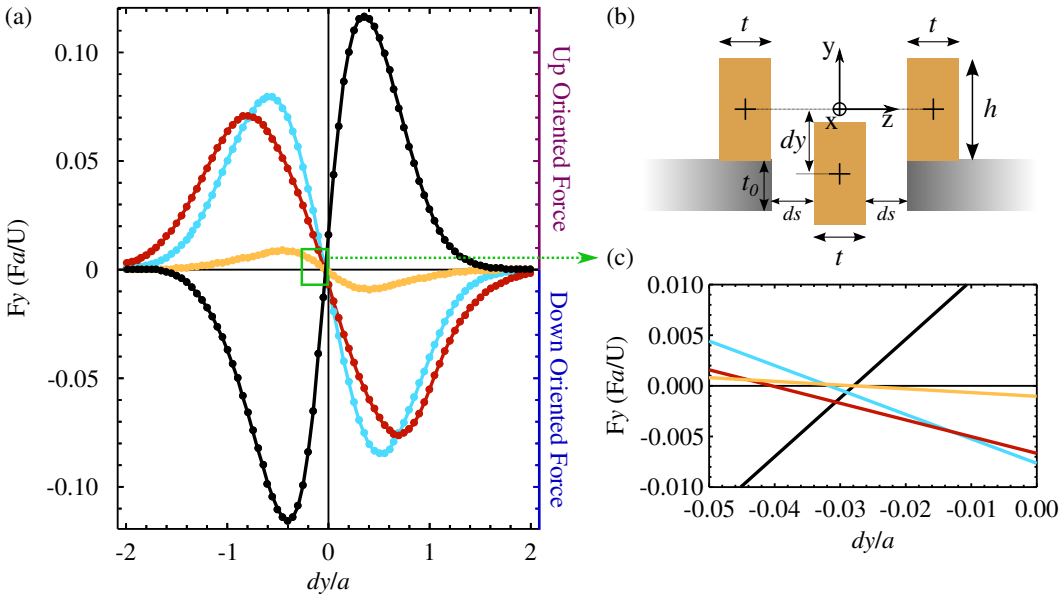

Figure 4.6: **(a)** Normalize force per unit energy as a function of a displacement dy/a for the Yodd-Zeven(1), Yodd-Zodd, Yodd-Zeven(2) and Yeven-Zodd modes at a constant axial wave-vector $k_x = \pi/a$. **(b)** Schematic of the geometry in use where a is the height of the blocks and t_0 is the thickness of the SiO_2 support layer equal to $0.5a$ and the height and thickness of the waveguides is $h = a$ and $t = 0.5a$ respectively. **(c)** detail of (a), approximately of the box shown in clear green. **(d)** In-plane $\mathbf{E_{yz}}$ vector-field distribution (larger arrows mean more intense) with the total $|E|^2$ in the background (darker is more intense) for the same geometry and modes described in (b). All arrows lengths and color scales share the same normalization.

notably, the large intensity of the E_z component along the walls of the CB then translates into a very large pulling force, accordingly to the fourth principle. In fact, on a section of the waveguide of length a and for an input power of 0.1 W, the attractive force between the two closest waveguides, at a minimum separation of $0.02a$ (which corresponds to $dz = \pm 0.23a$), is $\sim 4\ nN$. In comparison, the largest attractive force between two parallel waveguides (2WC), shown in Figure 4.4(c), with identical cross-sections, separation and wavevector to the ones considered in this work, is $\sim 2.5\ nN$.

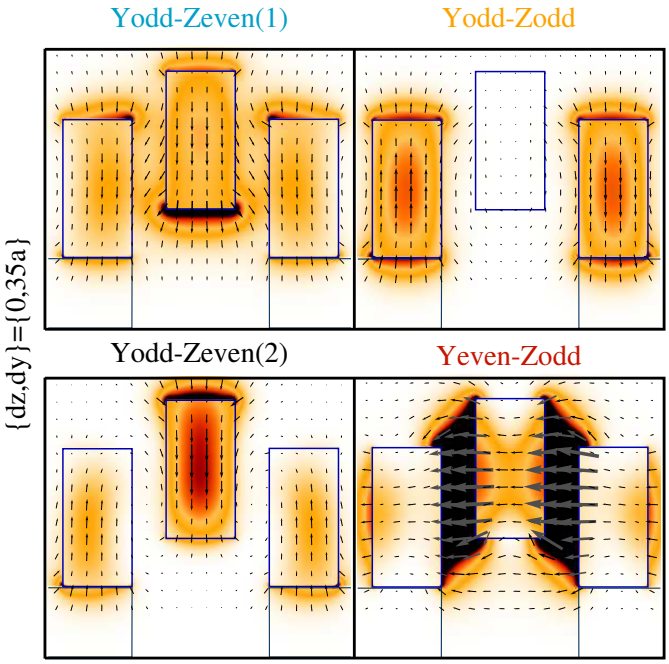

Figure 4.7: **(a)** Normalize force per unit energy as a function of a displacement dy/a for the Yodd-Zeven(1), Yodd-Zodd, Yodd-Zeven(2) and Yeven-Zodd modes at a constant axial wave-vector $k_x = \pi/a$. **(b)** Schematic of the geometry in use where a is the height of the blocks and t_0 is the thickness of the SiO_2 support layer equal to $0.5a$ and the height and thickness of the waveguides is $h = a$ and $t = 0.5a$ respectively. **(c)** detail of (a), approximately of the box shown in clear green. **(d)** In-plane $\mathbf{E_{yz}}$ vector-field distribution (larger arrows mean more intense) with the total $|E|^2$ in the background (darker is more intense) for the same geometry and modes described in (b). All arrows lengths and color scales share the same normalization.

4.4.2 y-axis oriented forces

In Figure 4.6(a) we show the behavior of the force for displacements along the y-axis and a detail of this figure is shown in Figure 4.6(c). We notice that for all modes the component of the optical force parallel to the y-axis is not 0 at $dy = 0$ but at $dy \approx 0.035a$. Such a small off-set justifies our initial assumption that, even in the presence of SiO_2 layers, we can assume the system to be optically z-axis symmetric. Also the presence of the SiO_2 is barely visible in the first row of Figure 4.5. As a result, since one of our objectives remains to illustrate the dynamic of the force via the field distribution of each mode, we conclude that our initial assumption was appropriate and that the SiO_2

plates only act as a mechanical support but has no significant impact on the field distribution of the modes considered.

As we have previously mentioned, the components of the force are decoupled along the axis of symmetry, so that induced displacements along the y-axis are independent on the forces along the z-axis, albeit related through their respective field distribution. From Figure 4.6(a) we observe that the OE(1), OO and EO induce trapping forces for displacements of the CB along the y-axis while only OE(2) induces levitation. As demonstrated in the previous section this behavior can be described by the field dynamics, shown in Figure 4.7.

OE(1), OO and EO modes

The trapping force induced by the EO and OE(1) are once more due to the first principle, since, in both cases, the dominant components are in phase through all three waveguides. As a consequence, for a displacement of the CB along the y-axis, the fields will tend to be centered close to $\{dz, dy\} = \{0, 0\}$, inducing a trapping force. A weak but now noticeable trapping force, due to the localization of the fields in the two external beams, is induced by the OO mode since, when CB moves, the fields stay localized along the z-axis.

OE(2) mode

Instead we observe a levitating force for the OE(2) mode. To better understand such behavior let's consider the case where the CB moves towards the origin from large and positive values of dy ($dy >> a$). In such condition the system can be thought as formed by two waveguides, one formed by the two external beams (that can now be thought as a single waveguide) and the CB, where the dominant field component of OE(2), E_y, is out of phase between the former and the later. As the separation between the waveguides is reduced, in order to satisfy the first-principle, the fields along the CB are expected to move towards its upper surface. The same behavior is observed when the CB penetrates the region between the two parallel waveguides, due to the fact that E_y is still out of phase between the CB and the external waveguides, as shown in Figure 4.7. As a result OE(2) induces a levitating force along the y-axis as can be seen in Figure 4.6(a).

4.5 2D trapping, the EE mode

If we were to disregard the magnitude of the force we can notice that the OO mode can be used to trap the nanobeam along both the y and z axis. How-

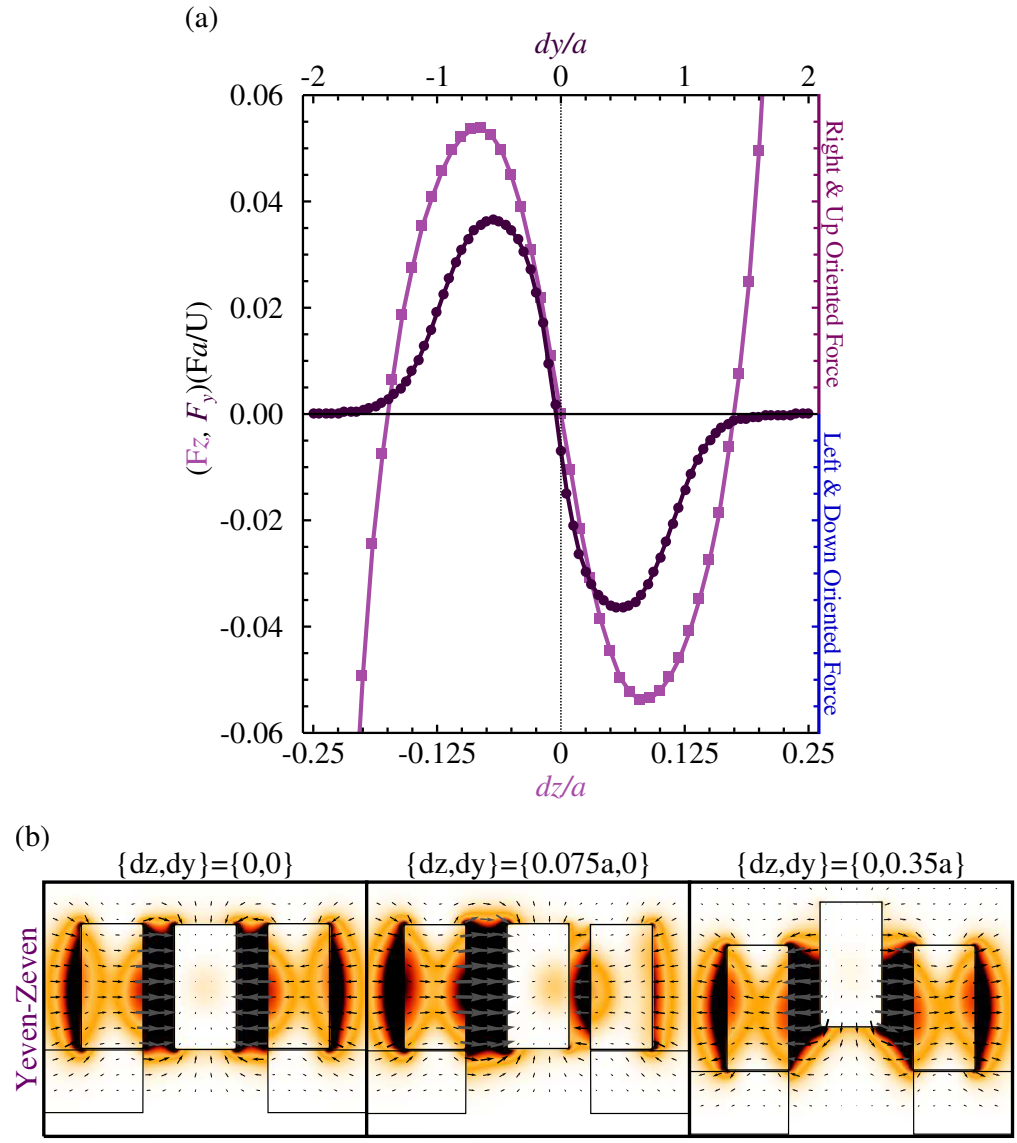

Figure 4.8: **(a)** Normalized force per unit energy as a function of a displacement dz/a and dy/a for the Yeven-Zeven mode at a constant axial wave-vector $k_x = \pi/a$ for the same geometry shown in the inset of Figure 4.4(a). **(b)** In-plane $\mathbf{E_{yz}}$ vector-field distribution (larger arrows mean more intense) with the total $|E|^2$ in the background (darker is more intense) of the Yeven-Zeven mode for three different displacements of the central beam. All arrows lengths and color scales share the same normalization

ever, since trapping force along the z direction is very small, two dimensional trapping does not seem feasible. A solution can be found by looking at higher frequency modes. In Figure 4.8(a) we plot the magnitude of the force along the y and z axis for the fifth mode in order of energy, which corresponds to the fundamental mode associated with the EE symmetry. From Figure 4.8(b) it can be seen that the mode is dominated by E_z, which is out of phase along the z-axis, but in phase along the y-axis. As a result the EE mode exhibits trapping force along both axis, even though the magnitude of the force is nearly two and five fold weaker compared to the trapping force induced by lower energy modes along the y and z axis respectively. However, since no optimization has been done on this system, it is reasonable to expect that larger values of the trapping force could be achieved.

A summary of the nature of the optical-force along both axis and for all the modes is illustrated in Table 4.1.

Table 4.1: Summary of the behavior of the force for each mode.

	Yodd-Zeven(1)	Yodd-Zodd	Yodd-Zeven(2)	Yeven-Zodd	Yeven-Zeven
z-axis	pulling	trapping	trapping	pulling	trapping
y-axis	trapping	trapping	levitating	trapping	trapping

4.6 Tailoring forces via geometry

It is important to notice the large scale difference for displacements along the two axis. The CB is free to move between $-2a$ and $2a$ along the y-axis and only between $-0.25a$ and $0.25a$ along the z-axis. In fact, in real scale scenarios where the maximum displacement of the beam is at most a fraction of a [4], forces along the y-axis will have little effect on the CB if no further means to enhance or tailor the intensity of the force are used. Here we chose to mold the component of the force along the y-axis and z-axis to have non zero magnitude when the CB is located at $\{dz, dy\} = \{0, 0\}$, thus allowing us to control the position of the trap and the direction of levitation in concordance with the mechanical properties of the CB. For example, the position of the point of equilibrium along the y-axis can be changed by breaking the z-axis symmetry. In fact, the forces at $dy = +\infty$ and $-\infty$ are expected to be of opposite sign, no matter the specific geometry of the system, and, for asymmetric systems, the point of equilibrium (where forces change sign) can happen at any point but the origin. As a case study, in Figure 4.9(a), we chose to tilt the walls of the waveguides in order to break the y-axis symmetry as shown in the inset.

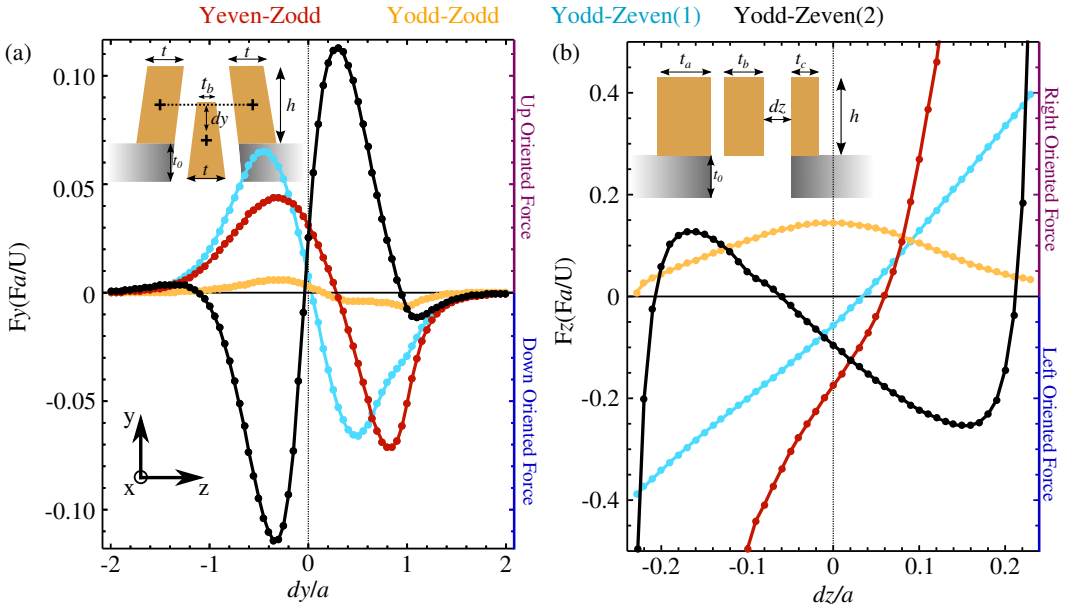

Figure 4.9: **(a)** Normalized force per unit energy as a function of a displacement dy/a for the Yodd-Zeven(1), Yodd-Zodd, Yodd-Zeven(2) and Yeven-Zodd modes at a constant axial wave-vector $k_x = \pi/a$. The height of the waveguides is $h = a$, $t_b = 0.25a$, $t = 0.5a$, $t_0 = 0.5a$ and, when all waveguides lay on the same plane, the walls of the external waveguides are parallel to the walls of the central waveguide. **(b)** Dimensionless force as a function of a displacement dz/a for the Yodd-Zeven(1), Yodd-Zodd, Yodd-Zeven(2) and Yeven-Zodd modes at a constant axial wave-vector $k_x = \pi/a$. In the inset we show the schematic of the geometry in use where a is the unit length, $h = a$, $t_a = 0.55a$, $t_b = 0.5a$, $t_c = 0.45a$ and $t_0 = 0.5a$.

In this condition the thickness of the top base is $t_b = 0.25a$, the bottom base $t = 0.5a$ and, when the CB lays at the origin, the separation between the walls of the CB and the external waveguides, defined by a line that crosses both walls normally, is $0.25a$. In this case we see a significant displacement of the position of the trap, specifically for the EO mode. For the remaining modes the effect is too small to be seen on the chosen scale but are comparable to those observed in Figure 4.9(a) for the scale on which dz is represented. Likewise, by breaking the y-axis symmetry, we can expect that the point of equilibrium will shift along the z-axis. A very simple example is shown in Figure 4.9(b) where we chose to slightly perturb the thickness or each waveguide with the rule $t_c < t_b < t_a$. As a result we observe a shift in the position of the trap (OE(2)) toward the left most waveguide (t_a), while the effect is opposite for

pulling forces (OE(1) and EO modes). We also observe a significant change for the OE mode which now induces a force toward the right most waveguide for all separations.

4.7 Conclusion

In conclusion we have studied and explained dynamics of gradient optical forces in the 3WC. This system shows better performance and more complex functionality than the 2WC and can be used to gain optomechanical control along the whole plane transverse to the direction of propagation of the optical mode. Effects like single-mode optical trapping and single-mode optical levitation of the free nanobeam have been discussed and we propose strategies to tailor such forces by breaking the symmetry of the cross-section of the waveguides. Moreover, all the proposed geometries are amenable to fabrication with standard lithographic techniques. We believe that three waveguides configuration, not only extends the possible application of gradient optical forces, but it can be useful to the development of new reconfigurable optomechanical devices for optical MEMS applications like switching or multiplexing [5] and might lead the path to develop optomechanical system on stretchable materials [6, 7], where larger optomechanical control should facilitate the manipulation of soft suspended structures.

Bibliography

[1] P. T. Rakich, M. A. Popovi&cacute, M. Soljači&cacute, and E. P. Ippen. Trapping, corralling and spectral bonding of optical resonances through optically induced potentials. *Nature Photonics*, 1(11):658–665, 2007.

[2] J. D. Joannopoulos, R. D. Meade, and J. N. Winn. *Photonic Crystals: Molding the Flow of Light*. Princeton Univ. Press, 1995.

[3] M. Li, W.H.P. Pernice, and H.X. Tang. Tunable bipolar optical interactions between guided lightwaves. *Nature Photonics*, 3:464–469, 2009.

[4] V. Intaraprasonk and S. Fan. Nonvolatile bistable all-optical switch from mechanical buckling. *Applied Physics Letters*, 98(24):241104, 2011.

[5] Mo Li, W H P Pernice, and H X Tang. Broadband all-photonic transduction of nanocantilevers. *Nature Nanotechnology*, pages 377–382.

[6] C. L. Yu, H. Kim, N. De Leon, I. W. Frank, J. T. Robinson, M. McCutcheon, M. Liu, M. D. Lukin, M. Loncar, and H. Park. Stretchable photonic crystal cavity with wide frequency tunability. *Nano letters*, 13(1):248–52, January 2013.

[7] Y. Chen, H. Li, and M. Li. Flexible and tunable silicon photonic circuits on plastic substrates. *Scientific reports*, 2, 2012.

Chapter 5

Selective and efficient optomechanical excitation of high frequency modes of micro-mechanical beams

The working principle behind all optomechanical devices is twofold: either optical forces are used to statically monitor the separation between two objects [1], or via phonon-photon coupling, as a mean to measure the change of the mechanical resonant frequency of the device [2]. Either way, in order to increase the optomechanical interaction, most work have been focused on enhancing optical forces via slow light or high-Q systems [3–6], while little attention has been paid to the mode-matching between optical forces and mechanical vibrational modes. In this chapter we demonstrate that this can be done via a system formed by three coplanar, parallel waveguides, rather than the usual two, where only the central one is free to move. In this structure optical forces can be designed to match a specific vibrational mode of the central waveguide by, for example, changing the thickness or the refractive index of the external waveguides. We consider two different techniques to do so: by asymmetrically modulating the refractive index of the external waveguides via optical free-carrier injection or by designing their shape. With this technique gradient-forces can be accurately tailored to match the amplitude profile of any given vibrational mode, allowing its selective and efficient excitation. Furthermore, when free-carrier injection is used, once the carriers have recombined, a different configuration can be chosen.

5.1 Selective excitation

In chapter 2 we presented the most common description of optical forces based on perturbation theory. In this description the force is given by the change of the optical-mode's eigenfrequency for an infinitesimal mechanical displacement, which is a convenient description when studying periodic structures for which the coupling between mechanical and optical modes is a "property" of the system rather than a tunable parameter. Here, because of the lack of periodicity in our system, we choose a nearly identical formulation but with a purely classical derivation that gives a simple and clear intuition about the coupling between the optical pulse and a specific mechanical mode.

Classically the excitation efficiency on any mechanical mode is given by the work done by a given force on such mode, which can be written as:

$$dW = \mathbf{f}_o \cdot d\mathbf{s}. \tag{5.1}$$

Where $d\mathbf{s}$ is an infinitesimal displacement of the system and $\mathbf{f}_o$ is the force density at a given point of the object. It is obvious that, if mechanical modes are considered, $d\mathbf{s}$ is defined by the mechanical mode itself.

5.1.1 Surface formulation of the Maxwell Stress tensor

It can be easily demonstrated that, at the steady state, optical forces can be written as $F_o = \int_A \mathbf{f}_o \, dA = \frac{1}{2}\int_V \nabla\varepsilon \left|E\right|^2 dV$ [7], where ε is the dielectric function of the waveguides. Unfortunately, as it is, this integral is ill defined since the electric field is double valued at the surface of the waveguides, where $\nabla\varepsilon$ is non-zero [8]. To solve such integral we simply assume that the transition from ε_1 to ε_2 it is continuous: $\varepsilon(\mathbf{r})$, which represents the dielectric function over an infinitesimal layer between the two media, similarly to what was done in [9]. As a result the component of the electric field normal to the interface can be written as $E_\perp = D_{\perp 0}/\varepsilon(\mathbf{r})$, a straight forward consequence of the Gauss law. For convention $D_{\perp 0} = \varepsilon_0 E_{\perp 0}$ is measured at the interface but inside the high refractive index media and $\varepsilon(\mathbf{r})$ is an arbitrary, simple enough, function that describes the value of the refractive index as it changes from ε_1 to ε_2 and vice versa. All together we obtain that the force can be written as.

$$\mathbf{F} = \int_A f_o \, \mathbf{n} \, dA = \int_A \frac{\Delta\varepsilon}{2}\left(\left|E_\parallel\right|^2 + \frac{1}{\varepsilon_1\varepsilon_2}\left|D_\perp\right|^2\right)\mathbf{n} \, dA. \tag{5.2}$$

Where A is the surface of the waveguide, ε_1 and ε_2 are the permittivity inside and outside the waveguides respectively, $\Delta\varepsilon = \varepsilon_1 - \varepsilon_2$ and f_0 is the magnitude

of the force. The optical force is directed normally to A, id est along $\mathbf{n}$, and oriented from the high to the low index media; $E_{\parallel}$ and $D_{\perp}$ represent the electric and displacement fields parallel and normal to A. By substituting Equation 5.2 into Equation 5.3 and imposing that $dW = dU$, where $U = N\hbar\omega$ for non-absorbing media, we find back the usual description of gradient-forces, Equation 2.35.

5.1.2 Selective modal excitation

In this section we describe the condition for selective excitation of a specific mechanical mode, where we assume that the optical-forces can be tailored without changing the mechanical properties of the object they act on. For simplicity, we only threat the case of linear elastic beams (membranes follow an identical description) in the limit of small deformations, discussed in section 2.7. Under this assumption the deformation of a given mechanical mode can be written as $d\mathbf{s}(y,t) = \{s(y,t), 0\}$, where the axis of the beam is parallel to the y-axis. At rest $d\mathbf{s}(y,0) = \{ds(y), 0\}$, which implies that $d\mathbf{s}(y)\cdot\mathbf{n}(y) = s(y)n(y)$, where $\mathbf{n}(y)$ is the vector normal to the surface of the beams as defined in the previous section. Via Equation 5.2 and Equation 5.2 we obtain:

$$dW \propto \int_A s(y) f_o(y) n(y)\ dA. \tag{5.3}$$

For a waveguide initially at rest $n(y) = 1$ so that Equation 5.3 is proportional to the orthogonality condition of the mechanical mode if $f(y) \propto s(y)$. That is to say if the optical forces mimic the deformation of the selected mechanical mode. If the beam is not initially at rest the forces can still be selective if $f_o(y,t) = Ls(y,t) + f_o(y)$, where L is a constant to be fitted, which is a reasonable assumption in the limit of small displacements. Once more, we can obtain that $\mathbf{n}(y,t) \cdot d\mathbf{s}(y,t) = ds(y,t)$ by definition of $\mathbf{n}$ so that Equation 5.2 becomes:

$$dW \propto \int_A \mathbf{ds}(y,t)(Ls(y,t) + f(y,0))\ dA. \tag{5.4}$$

This equation is proportional to the orthogonality condition of the mechanical eigenmode if $f(y,0) \propto s(y,t)$, which is true since the time part of $d\mathbf{s}$ only adds a phase to the amplitude of the mechanical oscillation.

5.2 Geometric modulation

To demonstrate that f_o can indeed be designed to mode-match a specific mechanical mode, we first study the case where a geometrical modulation is used

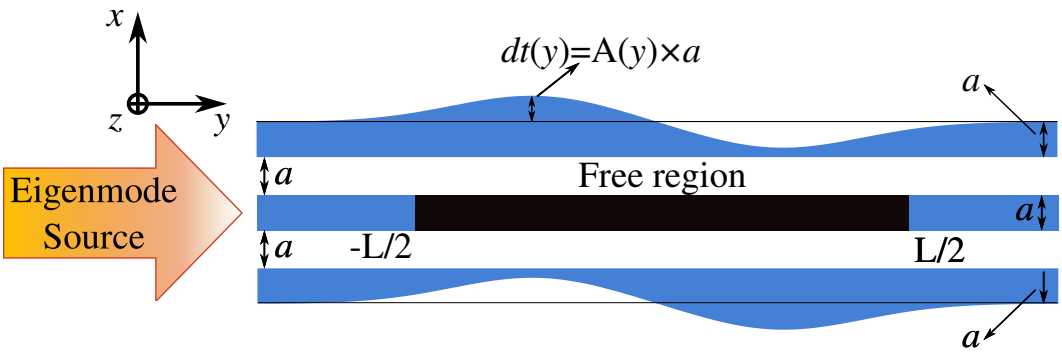

Figure 5.1: Schematic description of the system in use with geometrical modulation of the thickness of the external plates, where a is the unit length of the system.

to control the forces along the waveguides as shown in Figure 5.1. In our example the waveguides are made of Silicon ($n = 3.45$) and the central plate (CP) is assumed to be free in a region of length $L = 30a$, marked in black. To achieve spatial mode matching between a selected mechanical mode of the CP and the gradient forces on this waveguide the thickness, $dt(y) + a$, of the external waveguides (EWs) is modulated asymmetrically while the CP remains untouched. Moreover, we only modify the position of the outermost walls of the EWs so that the separation, ds, between the CP and the EWs is constant along the y-axis. Such choice allows us the use of large modulations, dt, even for short separations between the plates.

To understand the effect of different values of dt on the forces we study a cross section of the system shown in Figure 5.1 which, in a first approximation and for smooth enough perturbations along the y-axis, should be similar to the forces on the full two dimensional structure at a given point. The structure is formed by three parallel, Silicon plates where the thickness of external ones changes in an asymmetric fashion, as shown in the inset of Figure 5.2, where what is "taken" from the leftmost plate ($-dt_0$) is "added" to the rightmost one and the separation between the beams is always constant and equal to a, an arbitrary unit length. The forces between the plates can be measured via a Equation 5.2. However, for different values of dt_0, the rough localization of the fields of this system can be easily predicted and, as a result, the forces too. Obviously the discussion presented in the previous chapter is still relevant to this section. We only focus our attention to the fundamental mode at a wavevector of $k_x = 0.667$, which correspond to a frequency of $\omega = 0.269$ marked in Figure 5.3. However a different choice of mode or frequency should not affect our conclusion, except magnitude and/or phase, since the actual

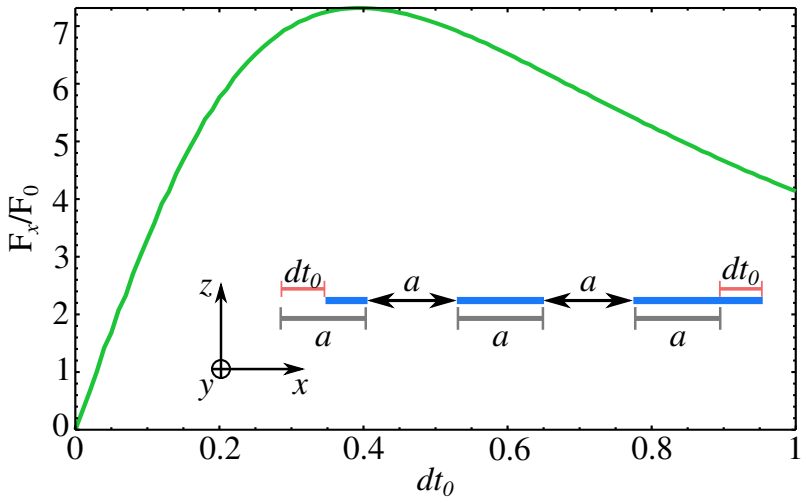

Figure 5.2: Normalized force for different variations of dt induced by the fundamental, propagative optical-mode through the one dimensional waveguide shown in inset at $\omega = 0.269$, which correspond to an in plane wave-vector $k_x = 0.667$.

profile of the force along the axis of the waveguide can be fully controlled by the geometry of the EWs. In Figure 5.2 we observe that the behavior of the force on the central beam, F_x, for a change of dt_0 is not monotonic. For small perturbations the force grows linearly, however, around $dt_0 \approx 0.3a$ it saturates and decreases for further increments of dt_0. Such behavior can be easily explained via the steps introduced in the previous sections. For small values of dt the fields, that were initially symmetrically distributed, start shifting from the shrinking waveguide (left) to the growing one (right), so that the electric field will become stronger between the CP and the rightmost waveguide, increasing the optical force between this waveguide and the CP. However, for larger values of dt_0, the fields will move away from the CP into the rightmost waveguide as well, thus reducing the force. This gives us an indication of the maximum allowed magnitude of dt_0 when a modulation is applied. In fact, for large values of dt_0, not only will we obtain reduced forces, but, as the light enters the region of variable thickness, we should experience scattering to other modes because of the large miss-match between the modal field-distribution in each region. However, if we choose a small value of dt_0, the resulting force will be small and, most importantly, small features would require simulations with very high resolution. Here we settle for a midway by choosing $dt_0 = 0.3a$.

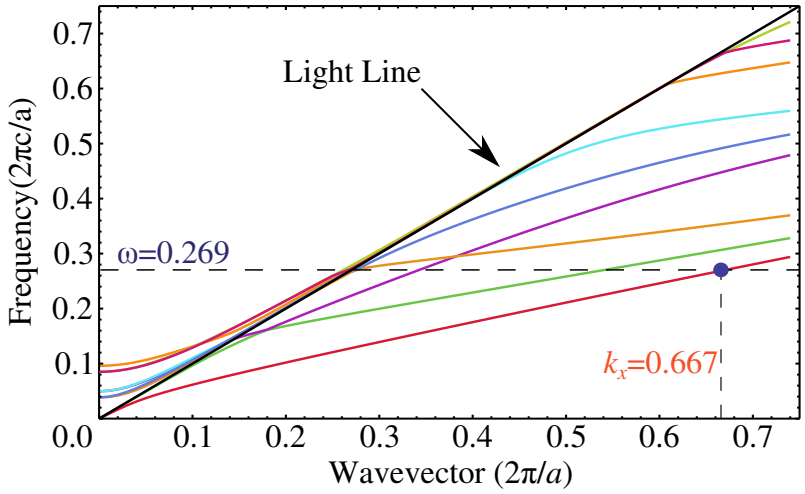

Figure 5.3: Dispersion diagram for the one dimensional system shown in the in the inset.

5.2.1 Geometrically tailored forces

In order to excite a mechanical eigenmode of the CP, $s_j(y)$ (Where j indicates the order of the mechanical mode), selectively, we tailor the distribution of the optical force $f(y)$ with a similar profile to $s_j(y)$ itself. This should be achievable by designing an appropriate modulation of the EWs; for example by choosing $dt(y)$ so that it follows the shape of $s(y)$. Here the mechanical displacement of the plate is approximated with a simple $s_j(y) \propto sin(2\pi j \times \frac{x}{L})$, according to the eigenmode solution of the Euler-Bernoulli theory presented in section 2.7. However, in order to obtain smooth width modulations of the EWs, which are useful to reduce the reflections, we approximate the sinusoidal shape as:

$$\frac{dt(y)}{a} = \sum_{i=1}^{j} A_0(-1)^i e^{-\left(\frac{j}{L}\right)^2 \sigma \left(x+\frac{L}{2j}(j-2i+1)\right)^2}. \tag{5.5}$$

In which σ is a multiplicative constant added to tune the thickness of the Gaussian shape and A_0 is the amplitude of each Gaussian.

By using the modulation Equation 5.5, we calculated optical forces along the waveguide $f(y)$ via 2D, steady-state FDTD simulations, where an eigenmode light source is used as described in Figure 5.1. However, instead of choosing a value of σ that better approximates the sinusoidal profile, we choose it by optimizing the shape of $f(y)$ for the 5^{th} order mode of $s_j(y)$. The results are shown in Figure 5.4, where the black curve represents the normalized force $f(y)$. The red curve is the mechanical displacement $s_j(y)$, while the orange

filled curve represents the geometrical modulation, Equation 5.5. As we can see, the matching between the Gaussian modulation, and $f(y)$ is good but noisy for the second and third order modes while it is very good for the fourth and fifth order ones. Altogether, considering that we only used a single free parameter to design the forces for four different cases it seems like we were able to obtain a very good agreement between the target profile and the measured force itself. A better agreement between $f(y)$ and $s(y)$ should be attainable via ad hoc optimized geometries rather than the simple approximation used here [10, 11]. In fact we believe that the noise over the force distribution, shown in Figure 5.4(a-b), is due to reflection to other optical modes with different group velocities, since, as we can also see from Figure 5.3, there are a

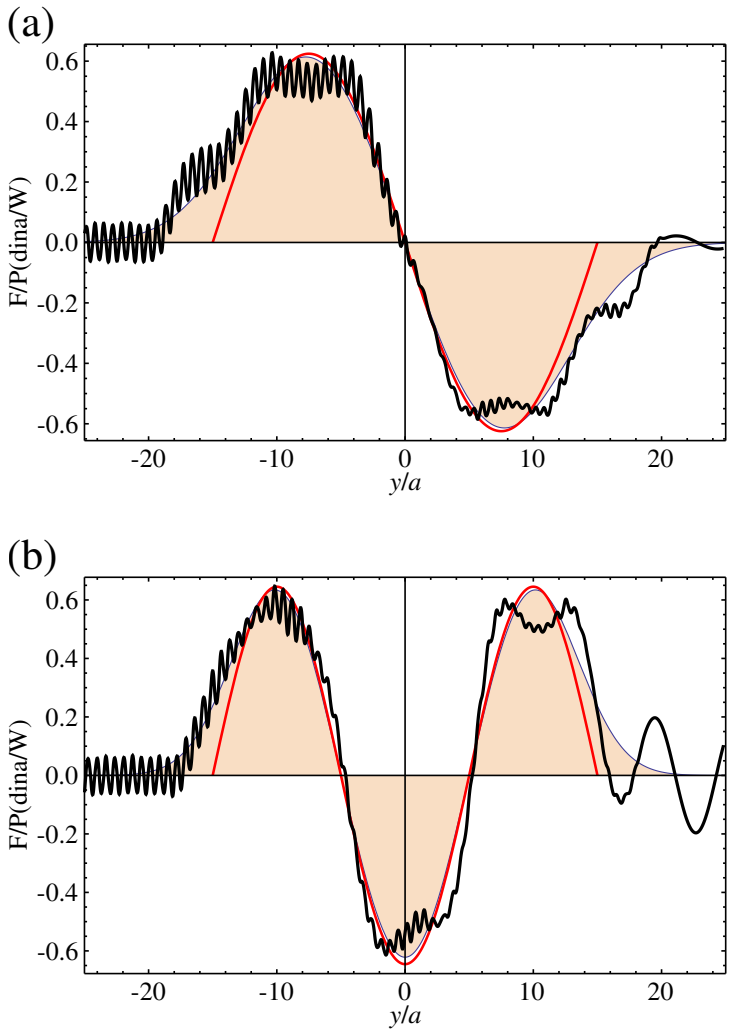

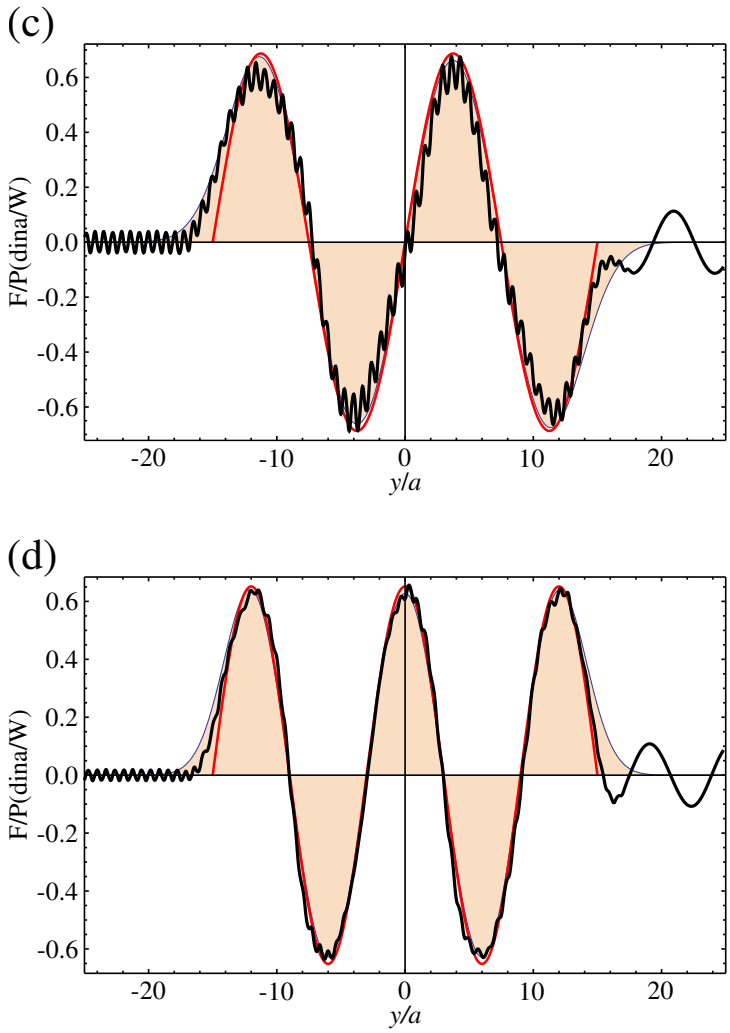

Figure 5.4: **(a-d)** Normalized optical force induced by an eigenmode signal propagating along the structure shown in Figure 5.1 only measured on its central waveguide. The red curve corresponds a sinusoidal curve that represents a simple approximation of to the nth order mechanical eigenmode of a plate made of Silicon, and free to oscillate in a section of length $L = 15a$. The orange filled curve represents the actual geometrical modulation used.

few guided modes at $\omega = 0.269$. As a result, when the incoming light comes in touch with the modulated area, part the signal will be reflected back to other modes with different group velocity, creating the interference patterns observed.

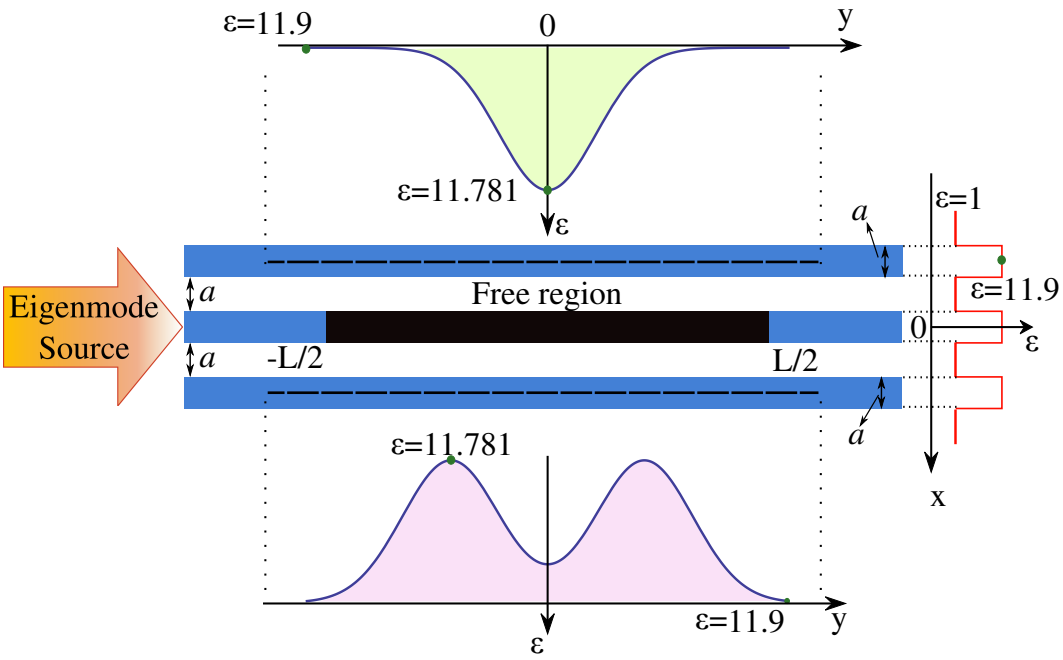

Figure 5.5: Description of the system in use where the refractive index of the external waveguides is modulated via free carrier injection. The refractive index change though is assume to be constant along the x-axis but of Gaussian shape along the y-axis. Once more the system is excited by an eigenmode source at frequency $\omega = 0.269$ and in plane wave-vector $k = 0.667$

5.3 Refractive index modulation

While the system we have studied so far can only selectively excite a prechosen mode, here we propose a method that should render our system reconfigurable. Geometrically the best candidate for such purpose is given by $dt(y) = 0$, for which, according to section 5.1.2 the forces can still be written as $f(y, x) \propto s_j(y)$. Under this condition, if the CP is already in motion optical forces can only interact with preexisting mechanical modes and no new mode should be exited. Unfortunately, this also implies that, if the CP is initially at rest, the optical forces in this system can not "start" any vibrational mode. To do so here we propose the use of a time dependent process based on optical carrier injection which temporarily breaks the optical symmetry of the system when the CP is at rest while mode-matching the forces to $s_j(y)$, the details of which are described in Figure 5.6.

Unfortunately free Carrier injection does not just change the refractive index of media but, as the free carriers recombine, it generates heat that might

create unwanted stress over our structure; not to mention the possible temperature variation of the CP due to radiative heat transfer, which it is difficult to predict [12]. These issues are not addressed here since they are out of the scope of this work, which is to determine if the force along the waveguides can be temporarily tailored via such method. Consequently we assume that the mechanical mode (at least on the time scale of the mechanical vibrations) is exited via a short impulsive optical load impulsive optical load, τ_{fc}, shorter than the life time of free carriers in Silicon, τ_{fc}. Under this condition optical forces are only be active before the recombination process takes place, after what we can wait for the transient effects of the recombination process to disappear.This process typically requires a few micro seconds, which is much shorter than the life time of the mechanical resonance $\tau_T << \tau_{me}$. At this

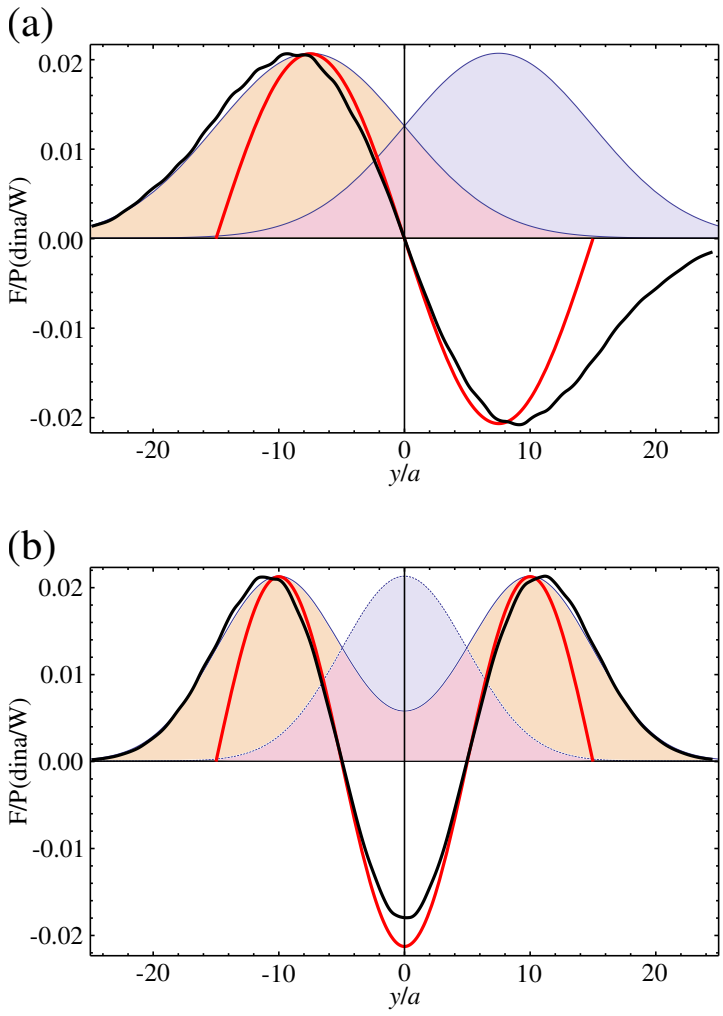

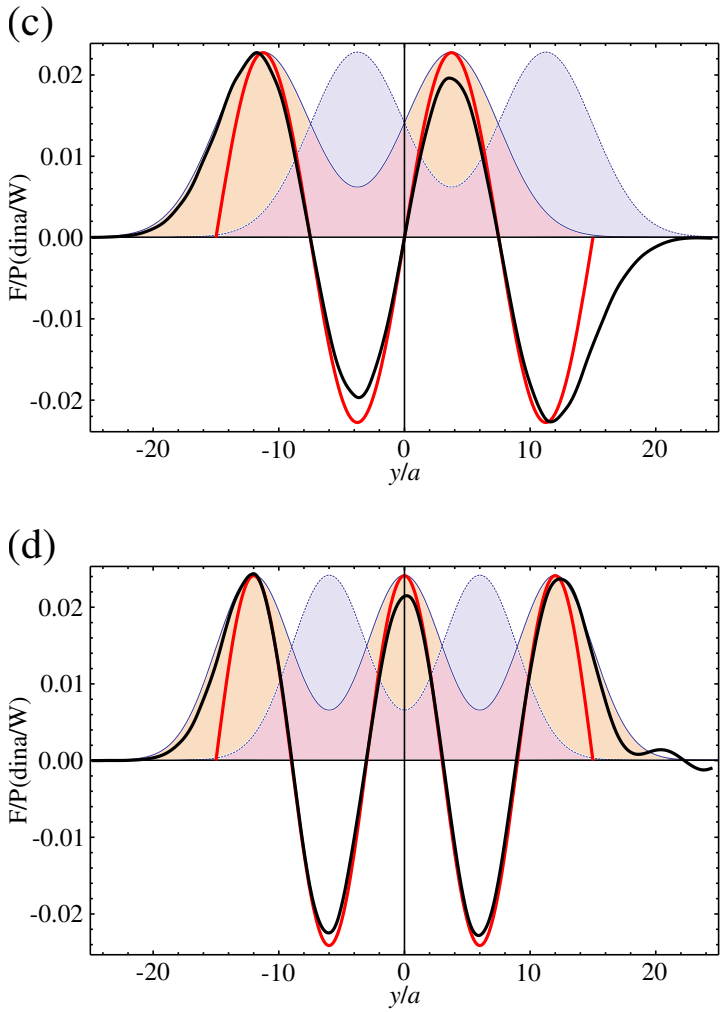

Figure 5.6: **(a-d)** Force induce by the an eigenmode signal as shown in Figure 5.5. The red curve represents a simple sinusoidal-approximation of the mechanical eigenmode. The continuous-blue, orange-filled and the dashed-blue, violet-filled curves represent, respectively the modulation of the refractive index of the bottom and top waveguide. For all cases we use $\sigma = 2$ and we assume a 1% maximum refractive index variation.

point we are free to drive our system as we desire knowing that only the initially exited mode will be affected.

Once more we use single-frequency FDTD-simulations to verify the effectiveness of our assumptions. The new system is described in Figure 5.6, where we assume that that the incident optical pulse used to induce free carriers in

the conduction band of silicon, induces a refractive index change limited to the external waveguides, constant along the y direction but Gaussian along the length of the waveguides. Such perturbation can be approximated to

$$\begin{aligned}\varepsilon_{Si}^{bot}(x,y) &= \varepsilon_{Si} - \sum_{i=2n-1}^{j} A_0 \times e^{-\left(\frac{j}{L}\right)^2 \sigma\left(x+\frac{L}{2j}(j-2i+1)\right)^2}, \\ \varepsilon_{Si}^{top}(x,y) &= \varepsilon_{Si} - \sum_{i=2n}^{j} A_0 \times e^{-\left(\frac{j}{L}\right)^2 \sigma\left(x+\frac{L}{2j}(j-2i+1)\right)^2}.\end{aligned} \tag{5.6}$$

Where ε_{Si}^{top} and ε_{Si}^{bot} correspond, respectively, to the modulated refractive index of the topmost and bottom most waveguides as shown in Figure 5.6.. In Figure 5.4 we show the instantaneous, normalized force density acting along the beam. The superimposing Gaussian profile represents the modulation of the refractive index of the bottom (in clear orange and continuous line) and top (clear purple and dashed line) waveguide. In red we show the amplitude profile of each mechanical mode, approximated to a sinusoidal shape, of the same order as the applied modulation. As it can be clearly seen the forces follow closely the amplitude and sign of the mechanical oscillations. This is largely due to the smooth and minute nature of the perturbation. We find that for either very high order mechanical modes, short values of L or large values of σ the system becomes more unstable, reducing the similarity between the force profile and the mechanical mode.

5.4 Conclusion

In conclusion we have demonstrated that selective and efficient optomechanical excitation can be achieved with the use of a three parallel waveguides configuration modulated geometrically or via optical carrier-injection; making the system fully reconfigurable. This technique also allows the coupling to anti-symmetric mechanical modes, whose coupling to the optical mode is otherwise forbidden by symmetry or very inefficient in common structures [13]. We believe that this technique shows good potential for applications to MEMS or optical devices where mechanical resonators with controllable and reconfigurable frequency are required, and in general it should facilitate the development of dynamic and reconfigurable optomechanical devices

Bibliography

[1] X. Zhao, J. M. Tsai, H. Cai, X. M. Ji, J. Zhou, M. H. Bao, Y. P. Huang, D. L. Kwong, and A. Q. Liu. A nano-opto-mechanical pressure sensor via ring resonator. *Optics express*, 20(8):8535–42, April 2012.

[2] Alexander G Krause, Martin Winger, Tim D Blasius, Qiang Lin, and Oskar Painter. A high-resolution microchip optomechanical accelerometer. *Nature Photonics*, 6, 2012.

[3] M.L. Povinelli, M. Ibanescu, S.G. Johnson, and J.D. Joannopoulos. Slow-light enhancement of radiation pressure in an omnidirectional-reflector waveguide. *Appl. Phys. Lett.*, 85(9):1466–1468, 2004.

[4] M. Notomi, H. Taniyama, S. Mitsugi, and E. Kuramochi. Optomechanical wavelength and energy conversion in high-q double-layer cavities of photonic-crystal slabs.

[5] M. Eichenfield, C.P. Michael, R. Perahia, and O. Painter. Actuation of micro-optomechanical systems via cavity-enhanced optical dipole forces. *Nature Photonics*, 1:416–422, 2007.

[6] G.S. Wiederhecker, L. Chen, A. Gondarenko, and M. Lipson. Controlling photonic structures using optical forces. *Nature*, 462:633–636, 2009.

[7] S. M. Barnett and R. Loudon. On the electromagnetic force on a dielectric medium. *Journal of Physics B: Atomic, Molecular and Optical Physics*, 39(15):S671, 2006.

[8] J. D. Jackson. *Classical Electrodynamics*. Wiley, New York, third edition, 1998.

[9] S.G. Johnson, M. Ibanescu, M.A. Skorobogatiy, O. Weisberg, and J.D. Joannopoulos. Perturbation theory for maxwell's equations with shifting material boundaries. *Phys. Rev. E*, 65(066611), 2002.

[10] J. Lu and J. Vučković. Nanophotonic computational design. *Opt. Express*, 21(11):13351–13367, Jun 2013.

[11] A. Oskooi, A. Mutapci, S. Noda, J. D. Joannopoulos, S. P. Boyd, and S. G. Johnson. Robust optimization of adiabatic tapers for coupling to slow-light photonic-crystal waveguides. *Optics Express*, 20(19):21558–21575, 2012.

[12] A. W. Rodriguezand M. T. H. Reid and S. G. Johnson. Fluctuating-surface-current formulation of radiative heat transfer for arbitrary geometries. *Physical Review B*, 86(22):220302, 2012.

[13] Y. Li, J. Zheng, J. Gao, J. Shu, and M. S. Arasand C. W. Wong. Design of dispersive optomechanical coupling and cooling in ultrahigh-q/v slot-type photonic crystal cavities. *Optics express*, 18(23):23844–23856, 2010.

Chapter 6

Conclusions

In conclusion we demonstrated that optomechanical control of dielectric waveguides can not only be done along a single line, but possibly, on the full three dimensional space if appropriate geometries are chosen. Most importantly we did so with a clear intuition on the relationship between geometry and the behavior of the force as the system is deformed. This is probably a concept that we have not stressed enough. In fact, one of the key elements for the success of every technology is not necessarily its performance or elegance, but, more often, is the *ease of use* and possible integration to existing fabrication methods. It is then essential to develop concepts that are easy to understand, use and that can be modeled via computer-aided design tools. New technologies should also be flexible and robust if integration on modern devices is required. Of course optomechanical devices which are, up to now, the most sensitive motion sensors every developed, possibly close to the ultimate quantum limit [1], are still not mature to become a future technology since most work has been focused on the magnificent possibilities that such technology exhibit scientifically [2], rather than on near future technological applications. This is the reason why we have focused on developing a semi-empirical method to tailor optical forces rather than concentrate on a particular structure and analyzing them analytically through some approximation [3].

6.1 Summary

In chapter 3 we presented five principles that can be applied in three recursive steps. All together this methodology allows a simple and intuitive understanding of the field dynamics as the separation between waveguides is changed. Of course there are limits to its applications: in general structures that are well

suited for this method are axis symmetric. However this is not a significant limitation since most systems ever considered in literature are, indeed, axis symmetric. Following this principles we demonstrate the existence of two and three dimensional structures that exhibit repulsive optical forces for all separation. Moreover the three dimensional structures proposed are amenable to fabrication with common lithographic techniques. The utility of this method is not necessarily limited to the self-action of the optical mode on the waveguides that support it but it can be useful in any process that requires the knowledge of the field distribution and its intensity along the waveguides. We have chosen not to explore alternative applications due to the lack of time and, most importantly, because it deviates from our main interests, An example is opto-fluidics, where nano-particles are actively controlled and trapped between parallel, coupled waveguides, this time fixed to a substrate [4] or, recently, researchers have considered the possibility of trapping single atoms in periodic photonics waveguides [5]. However, for what optomechanical systems are concerned, the simple action of attraction and repulsion per se is limiting. In principle there is no reason why optical forces should be limited to attractive or repulsive interaction. In chapter 4 we demonstrate that it is also possible to induce forces on the whole two dimensional-plane normal to the axis of the waveguides. This is done quite simply by using a system formed by three parallel waveguides instead of just the two of them. According to the guided optical mode chosen the forces can induce trapping of the middle waveguide along each axis or what we called two dimensional trapping along both axis. Moreover, via simple geometric modifications of the waveguides the position of the trap (that is to say the point where the forces are zero) can be actively controlled. This might be a significant advantage if we ever consider the possibility of optomechanical systems formed by soft materials, in which smaller forces can create larger mechanical displacements and the effect of static deformation should be more marked than in silicon photonics. However, in general, our goal in that chapter was not only to study such system but, most importantly to evaluate the possibility of applying the methodology developed in chapter 3 to systems with "less symmetry". We demonstrated that it is not always necessary to have a fully symmetric system but, in general, the behavior of the fields, and as a consequence the optical forces, can be predicted by knowing the field distribution in a given initial position. In fact we observed that, once the symmetry is broken, the change in field-distribution for different positions of the central waveguide is mainly mode related and the effect induced by geometry are more or less similar between different configurations. However this is not the only application of such system. In chapter 5 we demonstrate a system formed by three parallel waveguides can be used to obtain efficient and

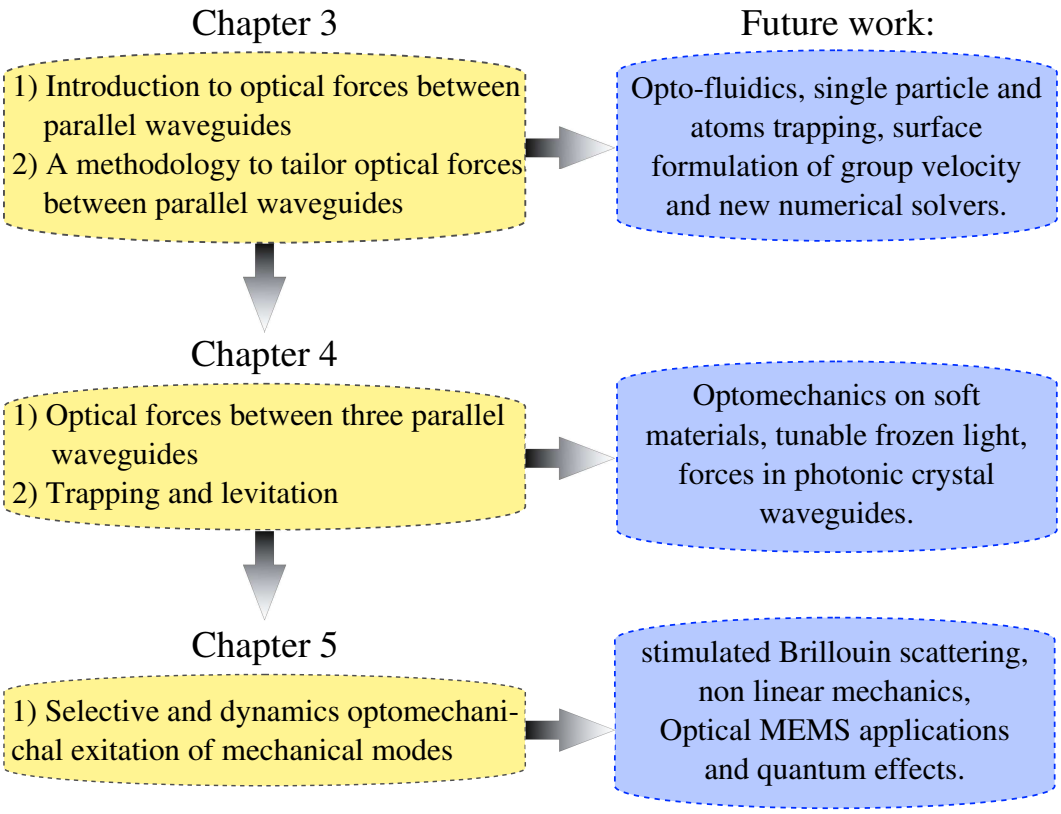

Figure 6.1: Summary of future work.

selective excitation of a given mechanical mode without the use of resonant techniques, as well as tuning its vibrational eigenfrequency dynamically. This offers an unprecedented new level of control of the mechanical vibrations and might be the first step toward deeper integration between optomechanics and MEMS devices. Selective excitation of a given optomechanical mode is indeed unprecedented. In fact, every system known to us, which are usually optimized to excite one or more mechanical modes are never selective and excitation of higher frequency mechanical modes is indeed expected [6].

6.2 Future work

There are several applications and paths that we have envisioned during the last years. First of all there are still several system that can be explored via our semi-empirical method like photonic crystal waveguides where the mode is guided not because localized on the high refractive index regions but because

the light is contained between two regions where its propagation is forbidden due to the presence of an optical band-gap [7]. In this case, however, if the waveguide is formed by a suspended waveguide rather than a continuous dielectric layer, we might be able to observe trapping at a position other that the origin even if the initial geometry is axis symmetric. Another interesting possibility is the relation between frozen light [8] and optical forces. Frozen light is basically slow light at wave-vectors different from the band edge. As such a system formed by movable parts should be able to jump on and off slow light states by simply changing the position of its movable part. This should offer a new way of tailoring optical forces via group velocity. Part of our work, although not yet successful has been oriented toward the development of a surface based formulation of frequency and group velocity, much like our formulation of optical force. Indeed this is a challenging theoretical problem but, if solved, it should allow the realization of faster and better eigensolvers and might be useful to find new geometries and properties of cavity and slow light devices which are of fundamental importance for any modern application of optics [9]. Slow-light band-edge modes can also be used in opto-fluidic devices. In fact, unlike propagative modes, modes just a little over the slow-light frequency are evanescent in nature. In such condition, particles that destroy the periodicity of the system should create new localized states that will allow transmission of light to the opposite side of the waveguide. In such case the forces acting on the particle should be oriented in opposition to the direction of propagation of light. If this were true it would be a major step toward the development of all optically control of opto-fluidic devices like cell sorters or sensors for medical and biological applications. Moreover, as we have previously mentioned, it should be straight forward to adapt the method developed in chapter 3 to improve the performance of opto-fluidic systems. Finally much work still remains to be done to fully develop the potentiality of the three parallel waveguides configuration. In principle this system can be used to study effects like: stimulated Brillouin scattering [10], non-linear mechanics [11] and quantum cooling. Also the mechanical effects due to the small fluctuation of the external waveguides should be assessed. In fact, we have so far assumed that these waveguides, being fixed to a substrate, have no significant optomechanical interactions with the optical modes. In reality this might not be true, specially when quantum optomechanical coupling is considered. In general our method and the structures we proposed should allow the improvement of existent devices, and hopefully the realization of new ones since the optomechanical interaction can be used for a variety of applications.

Bibliography

[1] A. H. Safavi-Naeini, Simon J. T. Gröblacher, Hill, J. Chan, M. Aspelmeyer, and O. Painter. Squeezed light from a silicon micromechanical resonator. *Nature*, 500(7461):185–189, 2013.

[2] Markus Aspelmeyer, Tobias J Kippenberg, and Florian Marquardt. Cavity optomechanics.

[3] W. H. P. Pernice, M. Li, and H. X. Tang. Theoretical investigation of the transverse optical force between a silicon nanowire waveguide and a substrate. *Optics express*, 17(3):1806–1816, 2009.

[4] D. Ericksonand X. Serey, Y. Chen, and S. Mandal. Nanomanipulation using near field photonics. *Lab on a Chip*, 11(6):995–1009, 2011.

[5] H Jeff Kimble. Trapped atoms in one-dimensional photonic crystals. In *Conference on Coherence and Quantum Optics*. Optical Society of America, 2013.

[6] M. Eichenfield, R. Camacho, J. Chan, K. J. Vahala, and O. Painter. A picogram-and nanometre-scale photonic-crystal optomechanical cavity. *Nature*, 459(7246):550–555, 2009.

[7] A. Mekis, J. Chen, I. Kurland, S. Fan, P. R. Villeneuve, and J. D. Joannopoulos. High transmission through sharp bends in photonic crystal waveguides. *Physical Review Letters*, 77(18):3787, 1996.

[8] N. Gutman, W. H. Dupree, Y. Sun, A. Sukhorukov, and C. M. De Sterke. Frozen and broadband slow light in coupled periodic nanowire waveguides. *Optics Express*, 20(4):3519–3528, 2012.

[9] T. Baba. Slow light in photonic crystals. *Nature Photonics*, 2(8):465–473, 2008.

[10] P. T. Rakich, C. Reinke, R. Camacho, P. Davids, and Z. Wang. Giant enhancement of stimulated brillouin scattering in the subwavelength limit. *Physical Review X*, 2(1):011008, 2012.

[11] R. Lifshitz and M. C. Cross. Nonlinear dynamics of nanomechanical and micromechanical resonators. *Reviews of nonlinear dynamics and complexity*, 1:1–48, 2008.

Acknowledgments

I would like to thank everyone I have meet during my Ph.D. for the support and help that, little by little, has allowed me to complete this wonderful trip. Not everything was easy, not everything was happy, but it was worth it. This experience has deeply changed me, not only intellectually, but as a human being.

One by one I would like to thank, Prof. Yoichi Kawakami, Prof. Shizuo Fujita, Prof. Takashi Asano, Prof. Susumu Noda, Dr. Richar Bardoux, Dr. Ardavan Oskooi, Dr Thirimadura De Zoysa Menaka Chaminda, Dr. Jeremy Upham, Mrs. Miki Watanabe and Miss Wang Mian.

Prof. K. Kawakami for his patience and countless hours of listening to me rambling about half-baked thoughts and ideas that barely made sense to me. He was understanding of our differences and always facilitated our relationship. Most importantly he gave me the chance to come to Kyoto University, where I have meet the most important person of my life and getting to know this country and its mesmerizing culture. Although we have our disagreements, I admire the deep human connection and friendly attitude towards his students and his laboratory which is one of the several good memories I will carry for life.

A big thanks goes to professor Shizuo Fujita, for his help during the realization of this thesis, his useful comments and support.

Another professor I would like to thank is T. Asano: He is without double one of the kindest and warmest professor I have every meet: an inspiration as a scientist and human being. I would like to deeply thank him for checking my papers over and over, polishing every line for style and content. This might not seem much unless you know you messy and forgetful I am. Scientifically, I owe part of my achievements to him and I would not be writing this thesis without his help. Thanks

A deep thank also goes to Prof. S. Noda. He allowed me to collaborate with his group and welcomed me to useful and inspired discussions, always with a friendly smile, and made me feel welcome at any time. Even after giv-

ing a bad presentation, due to an unfortunate incident with my slides at the JSAP meeting 2012, he had nothing but kind words for me. Even if I myself felt ashamed, even if Prof Asano had introduced me as one of his students, and he could have been, with reason, angry and disappointed, he was most understanding and his words gave me comfort when I needed.

I can not forget to mention Dr. R. Bardoux, Richard. He has been my friend since the moment I have joined Kawakami laboratory. As a hard working person and inspired human being he has taught me a lot and, just like Prof. Asano, his contribution to my papers was invaluable. He is a friend.

I would like to thanks A. Oskooi for introducing me to my research field and, in general, to computational physics which I love. He, most than anybody else, is the one I should thank for the success of my Ph.D. After seeing how desperate I was after an year and a half of hard work and not significant successes with my previous research, out of trust and good will, he gave me a direction and the small push that I needed. Thanks.

Thank Mrs. M. Watanabe for the continuous help and patience with documentation, information and guidance in all matters Japanese.

Thanks to Menaka and Jeremy for the hospitality and the fruitful discussions.

Finally, and most of all I would like to thank my fiancé, Wang Mian. She made everything worth it by pushing me down the hard road when I deeded or giving me a hug when I needed it more. She was also instrumental in understanding Japanese culture and always always pushed me to do more and better work in balance with my life. She is my strength and will for the future. Thanks.

Publications & Conferences

List of publications

[1] Ardavan Oskooi*, **Pedro Antonio Favuzzi***, Yoichi Kawakami and Susumu Noda, *Tailoring repulsive optical forces in nanophotonic waveguides.* Optics Letters, Vol. **36**, pages 4638-4640, 2011.

[2] Ardavan Oskooi*, **Pedro Antonio Favuzzi***, Yoshinori Tanaka, Hiroaki Shigeta, Yoichi Kawakami and Susumu Noda, *Partially disordered photonic-crystal thin films for enhanced and robust photovoltaics.* Applied Physics Letters, Vol. **100**, page 181110, 2012.

[3] **Pedro Antonio Favuzzi**, Richard Bardoux, Takashi Asano, Yoichi Kawakami and Susumu Noda, *Ab-initio design of nanophotonic waveguides for tunable, bidirectional optical forces.* Optics Express, Vol. **20**, pages 24488–24495, 2013.

[4] **Pedro Antonio Favuzzi**, Richard Bardoux, Takashi Asano, Yoichi Kawakami and Susumu Noda, *In plane manipulation of a dielectric nanobeam with gradient optical forces.* Optics Express, Vol. **21**, pages 29129–29139, 2013.

[5] **Pedro Antonio Favuzzi**, Richard Bardoux, Takashi Asano, Yoichi Kawakami and Susumu Noda, *Selective and efficient optomechanical excitation of high frequency modes of micro-mechanical beams.* In preparation, 2013.

* My equal contribution has been recognized in the manuscript: in which case both Dr. A. Oskooi and I are nominated as *first coauthors.*

International & national conferences

[1] **Pedro Antonio Favuzzi**, Ardavan Oskooi, Yoichi Kawakami and Susumu Noda, *Tailoring optical forces in nanophotonic waveguides.* PECS, Santa-Fe (USA), June 2012. Poster Session.

[2] **Pedro Antonio Favuzzi**, Ardavan Oskooi, Yoichi Kawakami and Susumu Noda, *Tailoring optical forces..* Spring meeting of the Japanese Society of Applied Physics, Tokyo (Japan), April 2012.

[3] **Pedro Antonio Favuzzi**, Ardavan Oskooi, Richard Bardoux, Takashi Asano, Yoichi Kawakami and Susumu Noda, *Ab-initio design of nanophotonic waveguides for tunable, bidirectional optical forces.* Autumn meeting of the Japanese Society of Applied Physics, Tokyo (Japan), September 2012.